

Miniaturized Laser Doppler Vibrometer
Integrated on a Silicon Photonics Platform

Miniaturisatie van een laser-dopplervibrometer
door middel van een fotonisch circuit op basis van silicium

Yanlu Li

Promotor: prof. dr. ir. R. Baets
Proefschrift ingediend tot het behalen van de graad van
Doctor in de Ingenieurswetenschappen: Fotonica

Vakgroep Informatietechnologie
Voorzitter: prof. dr. ir. D. De Zutter
Faculteit Ingenieurswetenschappen en Architectuur
Academiejaar 2012 - 2013



ISBN 978-90-8578-623-8
NUR 959
Wettelijk depot: D/2013/10.500/56



Universiteit Gent
Faculteit Ingenieurswetenschappen en
Architectuur
Vakgroep Informatietechnologie

Promotor:

Prof. dr. ir. Roel Baets

Examencommissie:

Prof. dr. ir. Rik Van de Walle (voorzitter)
Prof. dr. ir. Roel Baets (Promotor)
Prof. dr. ir. Patrick Segers
Prof. dr. ir. Wim Bogaerts
Dr. ir. Pieter Dumon
Dr. Christian Rembe
Prof. dr. ir. Joris J.J. Dirckx

Universiteit Gent
Universiteit Gent
Universiteit Gent
Universiteit Gent
Universiteit Gent
Polytec GmbH
Universiteit Antwerpen

Universiteit Gent
Faculteit Ingenieurswetenschappen en Architectuur

Vakgroep Informatietechnologie
Sint-Pietersnieuwstraat 41, B-9000 Gent, België

Tel.: +32-9-264.33.18
Fax.: +32-9-264.35.93



Proefschrift tot het behalen van de graad van
Doctor in de Ingenieurswetenschappen:
Fotonica
Academiejaar 2012-2013

Dankwoord

When I started my PhD, I felt like landing in a totally strange country, without knowing where to go and what to do. Gradually, I came to realize that the road to PhD is full of various challenges, obstacles, and failures. It really needs great courage to conquer all these difficulties. This would have been impossible without the support from professors, colleagues, friends, and family. I would like to thank you all, for sharing your knowledge and joys with me.

First and foremost, I would like to express my sincerest gratitude to my promoter, prof. Roel Baets, for his continuous support of my study and research. Seven years ago, he gave me the opportunity to join the Erasmus Mundus master program. Two years later, he offered me a PhD position to work in this excellent group. The five years' PhD life has been a wonderful experience to me. I am extremely impressed by Roel's enthusiasm for research. His passion always encourages me whenever I face difficulties.

I would also like to thank the other senior staffs in this group: prof. Günther Roelkens, prof. Dries Van Thourhout, prof. Peter Bienstman, prof. Geert Morthier, prof. Nicolas Le Thomas, dr. Danae Delbeke and dr. Pieter Dumon, for their supports and encouragements. I have also received a lot of help from outside of this group: prof. Joris J.J. Dirckx from Universiteit Antwerpen, prof. Patrick Segers from Universiteit Gent, dr. Christian Rembe from Polytec GmbH, dr. Paulo Santos from Paul-Drude-Institut, and dr. Lars Zimmermann from Technical University of Berlin, their help is really helpful and important for me.

Special thanks to the examination committee of my PhD defence, prof. Rik Van de Walle, prof. Patrick Segers, prof. Wim Bogaerts, prof. Joris J.J. Dirckx, dr. Pieter Dumon, and Dr. Christian Rembe, for their insightful comments and difficult questions.

I wouldn't have made those publications without the help of Diedrik Vermeulen, Yannick De Koninck, Gunay Yurtsever, Shahram Keyvaninia, Hui Yu, Lianyan Li, Bin Tian, Linghua Wang, Stijn Meersman, and Steven Verstuyft. I would also thank Eva, Peter De Heyn, Ashim, Martin, Samir, Nannicha, Bart, Cristina, Pauline, Alfonso, Thijs, Martijn, Ruijun, Sam, Weiqiang, Yunpeng, Joris, Sukumar, Nebiyu, Yingtao, Chen Hu, Ronny, Andrea, Zhechao, Honghui, William Chen, Tom, Wout, Shih-Che Hung, Liu Liu, Jonathan, Zhen Sheng, Dirk, Jie Teng, Karel, Kristof, Marie, Yu Ban, Zhisheng, Xiao Li, Xin Yin, Dries Willems et. al. for

so many discussions. I have been aided by so many skilful and helpful colleagues in the cleanroom, in the measurement laboratory, and in mask design. Thank you Steven, Liesbet, Kasia, Peter Geerinck, Parastesh, Jeroen, Michael, Manuel, Peter Guns, Jin Guo, and Amit. I have also received a lot of help from Dave, Bert, Mike, Kristien, Ilse and Ilse. Thank you for your time and efforts on my troubles.

For most of my PhD I have been working in the office 1.40 in Technicum. I was once forced out of this office when it was decorated, but I finally managed to come back. I love this office, not only because it is really close to the coffee room, but also because there have been a lot of nice and lovely office colleagues: Zhen Sheng, Hui Yu, Martin, Elewout, Karel, Parvathi, Pauline, Nannicha, Cristina, Linghua, Oscar, Andrea, and Yingtao. It is very pleasant to work with all of you.

Finally, I would like to give my heartfelt thanks to my parents and my wife, Ying. Special thanks to Ying, who gave up her job in China and came to support me. My life would not be so wonderful without her companionship.

Ghent, Aug 2013
Yanlu Li

Table of Contents

Dankwoord	i
Nederlandse samenvatting	xxi
English summary	xxv
1 Introduction	1
1.1 Different arrangements of LDVs	2
1.1.1 Single-beam LDVs	3
1.1.2 Dual-beam LDVs	5
1.1.3 Self-mixing LDVs	6
1.1.4 LDVs for multi-point measurements	7
1.2 Key parameters of an LDV	8
1.3 Silicon-on-insulator (SOI) platform	10
1.4 Contents and outline	12
1.5 Publications	12
1.5.1 Publications in international journals	12
1.5.2 Patents	13
1.5.3 Publications in international conferences	13
1.5.4 Publications in national conferences	15
References	16
2 Working principle of on-chip LDVs	23
2.1 Basic building blocks	24
2.1.1 Laser source	25
2.1.2 Interferometer	26
2.1.3 Imaging optical system	27
2.1.4 Photo-detectors	28
2.1.5 90° optical hybrid	29
2.1.6 Optical frequency shifter	30
2.1.7 Demodulators	30
2.2 Demodulation method for typical homodyne LDVs	31
2.2.1 Different demodulation methods for homodyne LDVs	31
2.2.2 IQ demodulation for ideal optical components	32
2.2.3 IQ demodulation for real devices	33

2.2.4	Compensation method	35
2.2.5	Noise issues	36
2.3	Demodulation method for heterodyne LDVs	37
2.3.1	Conventional demodulation method for heterodyne LDV	38
2.3.2	Ideal digital quadrature demodulation	39
2.3.3	Influence of spurious reflections and compensation methods	40
2.3.4	Influence of residue harmonics in the frequency shift	42
2.3.5	Influence of coupling variations in the reflected measurement light	45
2.3.6	Influence of noise	46
2.4	Conclusions	46
	References	48
3	Low-reflection optical components on SOI	51
3.1	Introduction	51
3.2	Low-reflection grating couplers	52
3.2.1	Tilted 1D grating couplers	53
3.2.2	Enhancement transmission in tilted 1D GCs	54
3.2.3	Angle deviation in the out coupled light	56
3.2.4	Tilted Focusing grating couplers	58
3.2.5	Tilted Focusing grating couplers with silicon overlay	63
3.3	Low-reflection multimode interference couplers	66
3.3.1	Simulation	67
3.3.2	Measurement	68
3.4	Other spurious reflections	69
3.5	Conclusions	71
	References	72
4	Optical frequency shifters	75
4.1	Optical modulation mechanisms in PICs	76
4.1.1	Electro-optic effect	77
4.1.2	Acousto-optic effect	78
4.1.3	Thermo-optic effect	80
4.1.4	Plasma-dispersion effect	80
4.1.5	Conclusions	82
4.2	OFS based on serrodyne technique	83
4.2.1	Serrodyne OFS based on the thermo-optic effect	87
4.2.2	Serrodyne OFS based on reverse biased PN junction	93
4.3	Four-branch interferometry frequency shifter	97
4.3.1	Four-branch method with pure phase modulation	97
4.3.2	Four-branch method with pure amplitude modulation	98
4.3.3	Four-branch method for reversed PN modulators	99
4.4	Conclusions	100
	References	102

5	Heterodyne and homodyne LDVs on SOI: measurement results	105
5.1	Measurement setups	106
5.2	Heterodyne LDV	109
5.2.1	Proof-of-principle fiber-based setup for heterodyne based LDVs	109
5.2.2	On-chip heterodyne LDV with TO-based heterodyne OFS	112
5.3	On-chip homodyne LDV	119
5.4	Conclusions	122
	References	124
6	Multi-point LDVs for arterial pulse wave velocity (PWV) measurements	125
6.1	Pulse wave velocity (PWV)	126
6.2	On-chip Dual-LDV device	128
6.3	Algorithms for retrieving PWV	130
6.4	Calibration and <i>in vivo</i> measurement	132
6.5	Scanning-beam configuration	133
6.6	Concept product design	135
6.7	Conclusions	136
	References	137
7	Conclusion	141
7.1	Conclusions	141
7.2	Prospectives	143
A	Optical frequency domain reflectometry	145
	References	147
B	Tilted grating coupler design	149
B.1	Introduction	149
B.2	Deviation of the direction in the out coupled light	149
B.3	Tilted focusing grating coupler	150
B.4	Tilted focusing grating coupler with amendment	151

List of Figures

1.1	The schematic of a typical single-beam heterodyne-detection LDV. f_0 is the original frequency of the laser light, $f_D(t)$ is the instantaneous Doppler shift of the reflected light due to the target movement, and f_{ofs} is the frequency shift of the reference signal introduced by the optical frequency shifter (OFS).	3
1.2	The schematic of a typical single-beam homodyne-detection LDV. f_0 is the original frequency of the laser light, and $f_D(t)$ is the instantaneous Doppler shift of the reflected light due to the target movement. A 90° optical hybrid with four photo-detectors are used in this system.	4
1.3	The schematic of a typical single-point heterodyne laser Doppler velocimeter used for measure fluid flow. f_0 is the original frequency of the laser light, and $f_D(t)$ is the instantaneous Doppler shift of the reflected light due to the target movement.	5
1.4	The schematic of a typical dual-beam LDV used for measuring fluid flow. f_0 is the original frequency of the laser light, and $f_D(t)$ is the instantaneous Doppler shift of the reflected light due to the target movement.	6
1.5	(a) The schematic of a typical self mixing LDV. (b) The output signals of a self-mixing LDV with different C parameter, reprinted from [32].	7
1.6	The SEM image of a waveguide bend on the silicon-on-insulator platform. Adapted from [67].	11
1.7	The 3d schematic of a heterodyne LDV integrated on SOI.	11
2.1	The schematic of a typical heterodyne on-chip LDV, in which PD stands for photodetector, OFS for optical frequency shifter, gc for grating coupler.	24
2.2	Three important parts of the imaging optical system: 1. on-chip optical coupler, 2. free-space imaging system, 3. a vibrating surface.	28
2.3	A typical IQ Lissajous curve for the homodyne outputs.	33
2.4	IQ curve for homodyne output signals with noise.	37

2.5	The typical noise spectrum for photo-detectors (Thorlabs PDB 440A). The red curve is measured when the inputs of the PD are blocked, while the black curved is for the case that the PD is switched off, which represents the system's noise floor. Reproduced from [20].	38
2.6	The influence of the spurious reflection on the demodulated results. In this case the power ratio between the spurious reflection and the useful reflection is around 30%. The vibrating frequency is 22.6 Hz. (a) the IQ Lissajous curve for signals with spurious reflection; (b) the solid curve represents for the original displacement signal and the dashed line is for the demodulated displacement.	42
2.7	Simulated root-mean-square (RMS) deviations of the demodulated displacements versus spurious reflections with different power and phase values, for power ratios (spurious reflection/useful reflection) between 0% and 60%. The 36 solid curves represent for 36 evenly spaced phases of the spurious reflection from 0 to 2π . The dashed line is the RMS deviation when the spurious reflection compensation is applied.	43
2.8	Photocurrent signals with strong -1st order harmonics generated by using an imperfect sawtooth driving signal. The solid curves show the original displacement value and break curves are the demodulated results. In 2.8(a), no phase compensation was done. In 2.8(b), the phase is compensated using equation 2.57.	45
2.9	The IQ Lissajous curve with a coupling modulation $\alpha_m(t) = [1 + 0.1 \cos(2\pi f_v t) + 0.1 \cos(4\pi f_v t)]$.	46
3.1	Schematic of Fresnel reflections and 2nd order reflections of a grating coupler.	52
3.2	(a) 3D wave vector relations in a tilted 1D grating coupler; (b) Relations of the projections of the wave vectors on the chip surface.	53
3.3	(a) The cross-section of a grating coupler with a silicon overlay; (b) Fractions of light coupled into the upward direction of different tilted GCs as a function of the azimuth α_0 ($\lambda_0 = 1550$ nm). The curves called "1D" are for the tilted 1D GCs with a 160 nm thick Si overlay, the curves called "1D (n)" are for the tilted 1D GCs without Si overlay, and the curve called "FGC" is for a tilted FGC designed for $\alpha_0 = 15^\circ, 45^\circ, 75^\circ$.	55
3.4	The effective indices of 1D grating couplers with silicon overlay as a function of wavelength and grating period. In this case $\beta = 0^\circ$.	56
3.5	Spectra of the upward coupled power of tilted 1D GCs with silicon overlay ($\alpha_0 = 45^\circ$), for different n_g values.	57

3.6	Schematic of tilted FGCs (exaggerated) on SOI with different azimuths: (a) $\alpha = 0$, (b) $\alpha \neq 0$. The black region is etched 70 nm into a 220 nm silicon layer while the rest is unetched. The light lines diffracting from the waveguide and the Fresnel reflections are indicated with the blue and red lines, respectively.	59
3.7	A scanning electron microscope image of a tilted FGC designed for $\alpha = 45^\circ$	60
3.8	3D Schematic of a tilted FGC (exaggerated) on SOI and its corresponding output fiber.	60
3.9	Maximal coupling efficiency between a single mode fiber and FGCs with different q_0 values and corresponding central wavelengths. The width of the waveguide aperture is $0.9 \mu\text{m}$	60
3.10	The transmission spectra of the tilted FGCs with different azimuths.	62
3.11	The maximal transmission efficiencies of the tilted FGCs and the corresponding central wavelengths. The horizontal line stands for the η of a standard FGC.	62
3.12	The peaks in the autocorrelation $R(z)$ caused by the reflection from the output tilted GCs with different azimuths. The autocorrelations are plotted in a logarithmic scale ($20 \times \log(R(z))$).	62
3.13	The maximal frequency averaged reflections of the tilted FGCs for different azimuths.	63
3.14	Measured transmission spectra of four tilted FGCs with Si overlays with different n_g values, $\alpha_0 = 45^\circ$. The “ref” curve stands for the transmission spectrum of a standard GC without any Si overlay.	64
3.15	The deviation of α_0 and ϕ_0 as a function of Δn_g . The solid and curved lines are calculated values. The \diamond and \circ symbols are the measured values.	64
3.16	The reflection values for FGCs with $\alpha_0 = 0^\circ$ (solid line) and tilted FGCs with $\alpha_0 = 45^\circ$ (dashed line). Both are with 160 nm thick Si overlay.	65
3.17	The top view of a 2x1 MMI.	66
3.18	(a) Reference simulation (b) Simulation structure of the MMI.	67
3.19	Simulation results for low-reflection MMIs: (a) isolation, (b) reflection.	68
3.20	The energy flux in 2x1 MMI (a) conventional 2x1 MMI; (b) the improved 2x1 MMI with the deeply etched boundaries on the right side of the device tilted by 60°	69
3.21	Reflections for two different 2x1 MMI couplers: the standard one with no boundary tilting and an improved one with a 60° tilt angle.	70
3.22	The roughness of the backside of the chip, with a root-mean-square deviation in height of $0.33 \mu\text{m}$	70

4.1	The relation between the refractive index change and the loss change (dB/cm) when the electron or hole concentration is changed from 0 to $2 \times 10^{18}/\text{cm}^3$	82
4.2	Time domain phase profile of an optical signal modulated with a serrodyne frequency shifter. In this case $\theta_{pp} = 2\pi$	83
4.3	Different harmonic orders (simulated) as functions of the peak-to-peak phase change: (a) power (b) phase.	85
4.4	Different harmonic orders (simulated) as functions of the fly-back time: (a) power, (b) phase.	85
4.5	Several nonlinear ramp signal, with $\chi = 0.5, \dots, 2$	86
4.6	Different harmonic orders (simulated) as functions of nonlinearity factor χ : (a) power, (b) phase.	86
4.7	Different harmonic orders as functions of spurious amplitude modulation: (a) power, (b) phase. In these figures, the spurious amplitude modulation is denoted as $20 \log(1 + \alpha_{2\pi})$	88
4.8	The cross section of the thermo-optic frequency modulator.	88
4.9	Optical loss due to the metal heater for different BCB thicknesses.	89
4.10	The SEM image of a thermo-optic modulator.	89
4.11	4.11(a): The temperature response ($\frac{\Delta T_{pp}(f)}{\Delta T_{pp}(0)}$) for three TO modulators with different BCB thickness, where $\Delta T_{pp}(f)$ is the peak-to-peak temperature variation at frequency f . 4.11(b): The phase delay for three TO modulators with different BCB thickness	90
4.12	An example of the square-root-of-time (SQOT) and sawtooth signals with a frequency at 1 Hz. When the voltage signal applied across the heater has a SQOT profile, the phase profile of the optical signal should be a sawtooth.	91
4.13	Optical power measured from the analog output of the powermeter as a function of time. An optimized thermo-optic serrodyne modulation (at 1 kHz) is applied to the reference arm. The measurement arm is connected with a fiber, but without any intended frequency shifted.	92
4.14	Power spectral density of the signal from the analog output. An optimized thermo-optic serrodyne modulation (at 1 kHz) is applied to the reference arm. The measurement arm is connected with a fiber, but without any intended frequency shifted.	92
4.15	The amplitude of the fundamental harmonic and 2nd order harmonic as functions of the sawtooth repetition frequency.	93
4.16	(a) Schematic cross section of an ideal abrupt p-n junction-based optical phase shifter. (b) A practical dopant distribution achieved by the implantation condition. Reproduced from [16]	94
4.17	The test structure of a PN diode based phase modulator. The actual modulator is split into three parts with each has a length of 1.5 mm.	94
4.18	The current-voltage curve of the reverse biased PN junction.	95

4.19	(a) The optical power of two outputs ports of the optical hybrid for a reverse biased PN junction, when a 2π peak-to-peak phase shift is generated in the PN phase modulator by a sawtooth voltage driving signal. (b) The Lissajous curve of the two outputs.	95
4.20	The power spectral densities of the two quadratic signals for a reverse biased PN junction.	96
4.21	The schematic of a four-branch interferometry used for frequency shifting.	96
4.22	The power spectral densities of different harmonics using the four-branch interference OFS with different phase amplitude δ	98
4.23	Power spectral densities of different harmonics as functions of modulator length when the carrier concentration of holes is modulated by a sinusoidal signal with an amplitude of $2 \times 10^{17}/\text{cm}^3$	99
4.24	The power spectral densities of different harmonics using the four-branch interference OFS (a) as functions of the amplitude deviation ζ in one arm, indicating that the light amplitude in one arm is increased by $1 + \zeta$ times, when the half phase amplitude $\delta = 1.53$. (b) as functions of the phase deviations ξ in arm arm, indicating that in one arm the phase is increased by ξ degree.	100
5.1	The picture of a fiber array from OZ-optics. Reproduced from [4].	106
5.2	(a) The schematic of a fiber array setup. (b) The photo of the fiber array setup.	107
5.3	A PIC design with grating coupler array, which is customized to a fiber array with a pitch of $250 \mu\text{m}$. A reference waveguide is also put in the design for the sake of alignment.	108
5.4	The measurement setup of the LDV.	108
5.5	Schematic configuration of the experimental setup. In the figure, L stands for the laser, C stands for the circulator, F stands for the focuser, VS stands for the vibrating surface, PM stands for the phase modulator, PC stands for the polarization controller, PD stands for photo-detector, TIA stands for transimpedance amplifier, ADC stands for analog-to-digital converter. Reproduced from [6].	110
5.6	Comparison of the demodulated results between Polytec LDV and fiber-based serrodyne LDV.	111
5.7	Figure of resemblance for different vibration frequencies and speeds with difference bandwidths of bandpass filters. (a): bandwidth of 12 kHz. (b): bandwidth of 24 kHz.	112
5.8	The PIC design of a Michelson type heterodyne LDV PIC.	113
5.9	Microscope images of the PIC. Images of the titled grating coupler [8], 2×2 multimode interference coupler, and reflector are also shown.	114

5.10	Demodulated displacements for on-chip LDV: the solid red curve stands for results measured with on-chip LDV, and the blue dashed lines are for results from Polytec LDV. Results in 5.10(a) are for the piezo vibration driven by a 50 Vpp signal, while those in 5.10(b) are for the vibration driven by 100 Vpp.	115
5.11	Response of the piezo-electric stack measured both by on-chip LDV (solid lines) and Polytec LDV (dashed lines). The peak-to-peak voltages of the piezo driver are chosen as: 1 V, 3 V, 5 V, 10 V, 30 V, 50 V, and 100 V.	115
5.12	The power spectral density of the demodulated signal, when the piezo stack is driven by a 50 Vpp signal at 22.6 Hz.	116
5.13	The power spectral density of environmental vibrations measured using LDV PIC with TO serrodyne frequency shift.	116
5.14	The PIC design and microscope images of the 90° optical hybrid and of the 2gc light receiving components.	118
5.15	Schematic show of a 90° optical hybrid. Reproduced from [10].	118
5.16	The configuration of the 1gc type and the 2gc type light receiver.	118
5.17	(a) The average light power values at each output port (DC_j) for the homodyne 1gc LDV. (b) DC_j for the homodyne 2gc LDV.	120
5.18	(a) The average light power values at each output port (DC_j) as a function of device temperature (2gc LDV). (b) DC_j as a function of the input power (2gc LDV).	120
5.19	(a) Demodulated signals for two vibrations in time domain. (b) IQ Lissajous curve.	121
5.20	Power spectral densities of the LDV outputs for the two vibration signals.	122
6.1	The artery system. Adapted from [11]	127
6.2	(a) The schematic of the PWV measurement device using a dual-LDV PIC chip. In the figure <i>os</i> stands for optical splitter, <i>hybrid</i> for 90° optical hybrid, <i>PC</i> for polarization controller, <i>BPD</i> for balanced photo-detectors, <i>Mon</i> for monitor, <i>TA</i> for transmitting antenna, <i>RA</i> for receiving antenna, <i>GC</i> for grating coupler. (b) The photo of a real dual-LDV chip with a bonded fiber array, compared with a two euro coin.	128
6.3	Calibration measurement results on two pulses generated on two separate loud speakers. The two pulses have the same shape but are generated at different times. (a) The measured two pulses with a delay of 0.8 ms. (b) The cross correlation of the two velocity curves, which shows a time delay of 0.85 ms. (c) The recovered delay time for different method, where x-corr means cross-correlation method.	131
6.4	(a) The velocity curves of the two pulses. (b) The cross-correlation of the two measured pulses. A time delay $\Delta t = 3.3$ ms is obtained using the correlation method.	132

6.5	(a) The displacements of the two pulses. (b) The accelerations of the two pulses.	133
6.6	Designs for different light paths using on-chip grating couplers and free space optical systems (mockup). Reproduced from [21]. . . .	134
6.7	The spacers of OVC, which are used to keep a distance between the optical components and the skin. Reproduced from [21]. . . .	135
6.8	The view of the PWV measurement device. Reproduced from [21].	135
A.1	The optical frequency domain reflectometry (OFDR) setup used for measuring reflections from a chip.	146
B.1	The vector relation of a 1D tilted grating coupler with an effective index error Δn	150
B.2	Schematic of tilted FGCs.	151

List of Tables

1.1	Summary of different commercial LDVs.	10
5.1	Performance of 1gc and 2gc LDVs, all values are compared with the power power of the reference light.	121
5.2	The performance summary.	123

List of Acronyms

A

ADC Analog-to-digital converter
AO Acousto-optic

C

CCA Common carotid artery
CMOS Complementary metal-oxide-semiconductor
CNR Carrier-to-noise ratio

D

DFB Distributed feedback
DSP Digital signal processing

E

EO Electro-optic

F

FGC Focusing grating coupler
FOR Figure of resemblance

G

GC Grating coupler

I

IQ In phase & quadrature

LLDI Laser Doppler imaging
LDV Laser Doppler vibrometer
LO Local Oscillator**M**MI Michelson interferometer
MMI Multi-mode interference
MZI Mach-Zehnder interferometer**N**

NA Numerical aperture

O

OFS Optical frequency shifter

P

PIC Photonic integrated circuit
PSD Power spectral density
PWV Pulse wave velocity

R

RA Receiving antenna
Radar Radio detection and ranging
RCS Radar cross section
RIN Relative intensity noise

S

SEM Scanning electron microscope
SLDV Scanning laser Doppler vibrometry
SOI Silicon on insulator

T

TA Transmitting antenna
TO Thermo-optic

Nederlandse samenvatting

–Summary in Dutch–

Trillingsmetingen zijn van groot belang in diverse industriële toepassingen en onderzoeksgebieden, zoals akoestiek, automobieltechniek, lucht- en ruimtevaart en medische biologie. Conventioneel wordt veelal gebruik gemaakt van accelerometers voor deze metingen. Toch heeft deze oplossing zijn beperkingen in een aantal situaties. Als belangrijkste probleem kan vermeld worden dat de accelerometers aangebracht worden op het oppervlak van het trillende doelobject, waardoor de trilling zelf kan verstoord worden. Voor trillingen die gevoelig zijn voor een belasting door extra massa, bijvoorbeeld bij de trilling van de trommelvlies, is het dan ook geen optie om een accelerometer te gebruiken. Verder hebben versnellingsmeters ook beperkingen bij trillingen met zeer lage frequentie. In vergelijking met accelerometers heeft de laser-dopplervibrometer (LDV) het voordeel contactloos te zijn en daardoor de trillingen niet te beïnvloeden. Tegenwoordig wordt de LDV-techniek dan ook veelvuldig gebruikt in tal van toepassingen en wordt hij algemeen aanvaard als een standaard meettechniek. In sommige moeilijke meetsituaties, zoals bijvoorbeeld trillingsmetingen in het oor, worden moeilijke eisen gesteld aan een LDV-apparaat. In het bijzonder dringt zich steeds vaker de eis op om een LDV-toestel te miniaturiseren. Op dit vlak is al enig onderzoek verricht, bijvoorbeeld met behulp van glasvezels of van de zelfmengingstechniek. Maar verregaande miniaturisatie en hoge prestaties werden nooit tegelijk verkregen met deze technieken.

In dit proefschrift stellen we voor de LDV-miniaturisatie te realiseren met behulp van fotonische geïntegreerde schakelingen (PICs) op een siliciumsubstraat, daarbij voortbouwend op de snelle vooruitgang in het domein van siliciumfotonica (“silicon photonics”) in het laatste decennium. In dit domein wordt gebruik gemaakt van CMOS-technologie om optische chips te fabriceren. Het doel van het voorliggende onderzoek is dan ook om een compact LDV-circuit met goede prestaties te realiseren op basis van siliciumfotonica. Dit opent het perspectief voor compacte en performante LDV-systemen met lage kostprijs.

De LDV-techniek is een coherente detectietechniek op basis van optische interferometrie. Er bestaan twee varianten, met name homodyne en heterodyne detectie. Het grote verschil tussen beide bestaat erin dat er voor de heterodyne techniek een optische frequentieverschuiving (OFS) nodig is in n arm van de interferometer. Hiermee kan men de invloed van ruis bij lage frequenties (1/f-ruis) veroorzaakt door elektronische componenten omzeilen. Bij de homodyne techniek gebruikt

men geen frequentieverschuiving maar wordt een zogenaamde 90-graden optische hybride ingezet om de demodulatiekwaliteit te verbeteren. In dit proefschrift worden beide technieken uitgelegd en toegepast, inclusief de bijhorende demodulatiemethodes.

Bij de implementatie van on-chip LDV wordt men geconfronteerd met een aantal uitdagingen die het specifieke gevolg zijn van de op geventreerde golfgeleiders gebaseerde aanpak. Volgens onze analyse kunnen deze uitdagingen in een drietal factoren onderverdeeld worden, met name de onbedoelde optische reflecties op de chip, de onvolmaaktheden van de optische hybride (voor homodyne) en deze van de optische frequentieverschuiving (voor heterodyne). Al deze effecten zorgen voor vervormingen op het meetsignaal. In sommige gevallen kan de vervorming te niet gedaan worden door middel van compensatie-algoritmes op basis van digitale signaalverwerking (DSP). Dit is volgens onze analyse vooral het geval als het ruisniveau laag is. Verder benodigen deze algoritmes lange rekentijden, waardoor ze moeilijk toepasbaar zijn voor trillingen met hoge frequenties. Om deze redenen is het belangrijk om de afwijkingen te verbeteren bij de bron. In dit proefschrift besteden we dan ook veel aandacht aan het verminderen van onbedoelde reflecties en het optimaliseren van de optische frequentieverschuiving.

De reflecties van roosterkoppelaars en van 1-naar-2 multimode-interferentie-koppelaars (MMI) vormen de belangrijkste bron van onbedoelde reflectie in een LDV-interferometer en ze worden vooral veroorzaakt door abrupte interfaces. Voor een roosterkoppelaar is dat vooral de overgang tussen het gebied met resp. zonder het rooster. Bij de MMI-koppelaar is het vooral de interface met diep geëtste gebieden die de boosdoener zijn. In het verleden werd meestal weinig aandacht besteed aan de optimalisatie van deze componenten op gebied van reflecties. Dat hebben we in dit werk wel gedaan. De strategie hierbij is niet zodanig om de reflecties uit te schakelen dan wel om het gereflecteerde licht weg te buigen van het inkomende golfgeleiderkanaal zodat het geen kwaad kan doen. Uit onze meetresultaten blijkt dat ons verbeterd roosterkoppelaarontwerp een reflectie van slechts -40 dB vertoont terwijl dat bij de verbeterde MMI-koppelaar -35 dB is.

De prestatie van een optische frequentieverschuiver wordt bepaald door de onderdrukingsverhouding van ongewenste harmonischen. In de praktijk moeten enkel de -1ste orde en de 0de orde harmonischen beschouwd worden, gezien de andere harmonischen onderdrukt kunnen worden door middel van filters in de demodulator. In dit proefschrift bestuderen we twee types van on-chip OFS-circuits, namelijk de serrodyne techniek en de vier-armige interferometer. In de serrodyne techniek wordt de fase van het optische signaal gemoduleerd met een zaagtandfunctie met een piek-tot-piek waarde van 2π . Om harmonischen te vermijden vereist de serrodyne techniek een zuivere fazemodulator met een perfecte zaagtandfunctie met de juiste amplitude. We hebben de invloed van allerlei fouten hierop geanalyseerd. Er blijkt bijvoorbeeld dat de bandbreedte van de fazemodulator ten minste 35 keer groter moet zijn dan de gewenste frequentieverschuiving. Verder moet de onbedoelde amplitudemodulatie kleiner zijn dan 4 dB. Een fazemodulator gebaseerd op de modulatie van ladingsdragers in een p-n junctie heeft een voldoende bandbreedte, maar vertoont altijd een te hoge amplitudemodulatie.

Bovendien is deze component vrij groot. De thermo-optische (TO) fazemodulator daarentegen heeft een perfect zuivere fazemodulatie maar heeft een erg lage bandbreedte (<10 kHz). Gelukkig kan een vier-armige interferometer toegepast worden waarbij in elk van de armen een fazemodulator gebaseerd op ladingsdragermodulatie ingezet wordt en elk hiervan sinusoidaal aangestuurd wordt met een geoptimaliseerde amplitude en fase. Met deze methode kunnen ongewenste harmonischen goed onderdrukt worden, zelfs in de aanwezigheid van een relatief sterke amplitudemodulatie. Bovendien is deze component compacter dan de serrodyne modulator. De prestatie van de vier-armige interferometer hangt wel af van afwijkingen in de fazemodulatie en onbalansen tussen de vier optische signalen. Deze afwijkingen kunnen door middel van extra fase- en amplitude modulatoren gecompenseerd worden.

Experimenteel hebben we een thermo-optische serrodyne OFS met een verschuiving van 2 kHz gerealiseerd. Hiermee hebben we een geminiaturiseerd LDV op silicium aangetoond. De TO-modulator bestaat uit een silicium optische golfgeleider bedekt met een Titanium metaalstrip voor de Joule-verwarming. Een BCB-polymeerlaag (Benzocyclobuteen) scheidt de golfgeleider van de metaalstrip teneinde optische verliezen te vermijden. We hebben dit LDV-circuit getest door licht vanuit de chip te richten op een trillende spiegel bevestigd mechanisch aangestuurd door een piezoelektrisch blok en het gereflecteerde licht terug in te koppelen in de chip. We hebben aangetoond trillingen met een amplitude van slechts 1 nm te kunnen detecteren. Een goede overeenkomst werd bekomen met metingen uitgevoerd met een state-of-the-art commercieel toestel van Polytec.

Daarnaast hebben we een on-chip homodyne LDV gerealiseerd, gebaseerd op een 90-graden optische hybride. Deze laatste werd gerealiseerd met een compacte 2-naar-4 MMI-koppelaar. De fazerelatie tussen de vier uitgangen van dit circuit laat een in-faze en kwadratuur (IQ) demodulatie toe van het optische signaal. Alhoewel de hybride niet perfect was ten gevolge van onnauwkeurigheden in de fabricage, konden de fouten toch met digitale signaalverwerking gecompenseerd worden. We hebben een minimaal meetbare verplaatsing van 6 nm kunnen aantonen.

Bij ons experimenteel werk hebben we nog geen lichtbronnen en detectoren gegtegreerd op de LDV-chip, aangezien we vooral de focus wilden leggen op de invloed van onbedoelde imperfecties en ook om de complexiteit en de kostprijs van het onderzoek te beperken. We hebben dan ook externe DFB-lasers en detectoren gebruikt, die we met de chip gekoppeld hebben via glasvezel-arrays.

Als toepassingsgerichte demonstrator hebben we een dubbel homodyne LDV-circuit op een chip gerealiseerd voor het meten van de arteriële bloedpulssnelheid (PWV) in de halsslagader. Deze bloedpulssnelheid is een belangrijke marker voor cardiovasculaire risicos. Vanuit deze chip werden twee lichtsignalen respectievelijk uit elk van beide LDV-circuits via een lensstelsel afgebeeld op twee plaatsen van de halsslagader. De huidbeweging ten gevolge van de onderliggende bloedpuls werd aldus op twee plaatsen gemeten. Uit de kruiscorrelatie van beide signalen kon de tijdsvertraging bepaald worden en dus de PWV. We hebben een tijdsnauwkeurigheid van 0.1 ms aangetoond. Aangezien de afstand tussen de twee

gemeten posities op de slagader ongeveer 1.5 cm was in de praktijk, betekent het dat de maximale meetbare snelheid van onze opstelling ongeveer 150 m/s is. Dit is voldoende voor praktische PWV-metingen.

Als conclusie kan gesteld worden dat LDV-systemen gebaseerd op silicium optische chips beloftevol zijn. Deze chips zijn compact, hun performantie kan hoog zijn en bovendien is hun kostprijs zeer laag indien gefabriceerd in volume. De integratietechniek is vooral heel waardevol wanneer meerdere potentieel zeer veel LDV-circuits gecombineerd worden op n chip voor toepassingen waar veel LDV-metingen in parallel dienen te gebeuren.

English summary

Vibration measurements are required in various industrial applications and research fields, e.g. acoustics, automotive, aerospace, and biomedicine. Conventionally, accelerometers are usually used for this type of measurement. However, some weaknesses of accelerometers keep them away from many applications. The largest problem with accelerometers is the disturbance of the target vibration caused by attaching the accelerometers on the vibrating target. For vibrations that are sensitive to mass loading, e.g. vibration of eardrums, the use of accelerometers for measurement is ruled out. Besides, accelerometers also suffer from their low measuring range of frequency. Compared to accelerometers, the laser Doppler vibrometry (LDV) technique has a very weak disturbance effect to the target vibration, due to its non-contact nature. Nowadays, the LDV technique is used in numerous applications and is widely accepted as a standard tool for vibration measurements. However, some difficult measurement situations, e.g. vibration measurement in the ear, impose more stringent requirements on the LDV devices. To meet these requirements, a device miniaturization is needed. A lot of research has been done to realize this miniaturization, for example, with the help of fiber-optics or the self-mixing technique. However, high compactness and high performance have never been obtained at the same time with these techniques. In this thesis, we propose to realize the LDV miniaturization using photonic integrated circuits (PICs) on the silicon-on-insulator (SOI) substrate. Based on complementary metal-oxide-semiconductor (CMOS) compatible technologies, a high performance, low-cost miniaturization technology in LDV can be realized on this platform.

The LDV technique is a coherent detection technique based on optical interferometry, and it exists in two basic detection schemes, namely homodyne and heterodyne. The major difference between these two schemes is whether an optical frequency shifter (OFS) is used in the reference arm of the interferometer. In heterodyne, an OFS is used to circumvent the influence of low frequency noise in electronics, while in homodyne such an OFS is not required. To improve the demodulation quality in homodyne, a 90° optical hybrid is usually used. In this thesis, the working principles of these two schemes and their corresponding demodulation methods are explained.

In on-chip devices, there also exist some deviation factors that can strongly influence the LDV outputs. According to analysis, three crucial influential factors exist in on-chip LDV. They are the unwanted optical reflections in on-chip devices, imperfect 90° optical hybrid designs (for homodyne), and imperfect optical

frequency shifts (for heterodyne). If any of these deviations cannot be neglected, the LDV outputs can be deformed. Therefore, to ensure a negligible phase deformation, the on-chip spurious reflections should be strongly suppressed. For the case of heterodyne, it is also important to suppress the -1 order and 0th order harmonics of the frequency shifted signal. Useful information may be recovered from the corrupted LDV outputs with the help of some compensation algorithms based on digital signal processing (DSP). According analysis, this recovery can be very accurate if noise is weak, but this situation is not always fulfilled. Besides, these algorithms take a long calculation time, which makes it difficult to use these algorithms for the compensation of high frequency vibrations. Therefore, it is important to improve the on-chip device designs regarding these deviations. In this thesis, we focus our efforts on the realization of spurious-reflection suppression and of a high quality optical frequency shift.

The reflections of grating couplers and 2×1 multi-mode interference (MMI) couplers are the major spurious reflection sources in an on-chip LDV interferometer, and they are mainly caused by the existence of mode-mismatching boundaries in these designs. For a grating coupler, the reflection boundary is the one between the input waveguide and grating region. For the MMI, reflections mainly come from the boundaries of the deeply etched trenches, which are used to form an optical waveguide. In many previously proposed on-chip optical devices, these boundaries are not carefully designed and can thus introduce considerable reflections. To solve this problem, we have made several new designs in which the reflection boundaries are deliberately tilted so that the reflections can be sent to somewhere else rather than the input waveguide. The back-reflection back to the input waveguide is strongly reduced with this method. From measurement results, it turns out that the reflection of an improved grating coupler design is reduced to -40 dB compared to the power of the input light. For improved 2×1 MMI couplers, the spurious reflection is believed to be about 35 dB lower than the input optical power according to simulations.

The performance of an OFS is characterized by the suppression ratios of high-order harmonics to the fundamental harmonic. In practice, only the suppression ratios for -1 st order and 0th order harmonics need to be considered, since the other sidebands can be removed by filtering in a demodulation stage. To realize and improve the performance of an on-chip OFS, two different techniques for generating the frequency shift, namely the serrodyne technique and the four-branch interferometry technique, are analyzed in this thesis. In the serrodyne technique, the phase of the optical signal is modulated to a sawtooth profile with a peak-to-peak phase variation of 2π , so as to create a desired frequency shift. In order to strongly suppress sidebands, the serrodyne modulation requires a pure phase modulator. The influences of the accuracy in phase modulation depth, of the modulator bandwidth, of the phase linearity, and of spurious amplitude modulations are analyzed with spectrum analysis. It turns out that the modulator bandwidth should be at least 35 times larger than the actual desired frequency shift and the spurious amplitude modulation should be smaller than 4 dB. The carrier-depletion type modulator has a sufficient bandwidth but suffers from its long length and intrinsic

spurious amplitude modulation, while the thermo-optic (TO) phase modulator has very weak spurious amplitude modulation but is also low in speed (<10 kHz). Luckily, a four-branch interferometry frequency shift technique can be used to avoid the problems occurring in carrier-depletion type modulators. In this four-branch interferometry technique, light signals in the four arms are modulated with four different sinusoidal signals. With carefully controlled phase delays, sidebands in the combined signal are strongly suppressed. Several simulations are made with respect to this design. According to the simulation results, the undesired sidebands can still be strongly suppressed even with a relatively strong spurious amplitude modulation. Another benefit with this method is a reduction in the total modulator length compared to serrodyne technique, since its peak-to-peak phase change does not need to be as large as 2π . The required bandwidth for the signal driver is also significantly smaller than serrodyne since the high-bandwidth sawtooth driving signal is not needed anymore. The performance of this four-branch interferometry is sensitive to the deviation of the phase shift in each optical signal and to the power imbalance among the four optical signals. However, these phase deviations and imbalances can be corrected with extra phase and amplitude modulators.

For demonstration, we have realized a TO modulator-based serrodyne OFS at a frequency of 2 kHz. With this TO OFS, a miniaturized LDV on SOI has been demonstrated. The TO modulator consists of a silicon optical waveguide, a titanium heater and an intermediate Benzocyclobutene-based polymer layer. The characterization of this device is realized by measuring a voltage-driven piezostack. Results show that a vibration with the amplitude as small as 1 nm can be detectable using this heterodyne LDV. These results are also compared with those obtained with a vibrometer from Polytec, and a good agreement is seen.

We have also reported an on-chip homodyne LDV, based on a 90° optical hybrid. The 90° optical hybrid is realized with a compact 2×4 MMI coupler. The special phase relation among the four outputs of the optical hybrid allows an in-phase & quadrature (IQ) demodulation to these signals. Though the hybrid may not work perfectly due to fabrication inaccuracies, the demodulation outputs can still be correctly recovered with certain compensation methods based on DSP. Measurement results show that the minimal measurable displacement of this on-chip homodyne device is around 6 nm. Note that in both of our heterodyne and homodyne designs, laser sources and photo-detectors are not integrated on the chip, to avoid the influence on on-chip interferometers and to reduce fabrication complexity. External distributed-feedback (DFB) lasers and photo-detectors, connected with the chip via a fiber-array, are used instead.

To show the advantage of the miniaturization, we have also demonstrated an on-chip double-LDV device with homodyne technology for measuring the arterial pulse wave velocity (PWV), an important marker for cardiovascular risks. In this device two stand-alone homodyne LDVs are fabricated on the same SOI chip. Two light beams from these two LDVs are sent to a common-carotid artery (CCA) with the help of an imaging system. Each LDV is responsible for recording the time when a pulse wave is moved to the measured position on the CCA. By calculating the transit time of a pulse between the two measurement positions with a cross-

correlation method, the PWV can be estimated. The time accuracy of this device is estimated by measuring two pulses with a controlled relative time shift. The time accuracy turned out to be around 0.1 ms. Since the distance between the two measured positions on the CCA is around 1.5 cm in practice, it indicates that the maximal measurable velocity of this device is around 150 m/s. This range is large enough to cover all possible values of the PWV. In conclusion, the SOI-based LDV system is a very promising technique. The size of this device can be very compact thanks to the small geometric dimension of SOI-based PIC designs. Since CMOS-compatible technologies are used for this platform, the production cost can be extremely reduced in case of high volume production. This platform is especially powerful for integrating multiple LDVs on the same chip, which can be used in many applications such as PWV measurements.

1

Laser Doppler vibrometer(LDV) and LDV-on-SOI

The Doppler effect of light was first introduced by the Austrian physicist Christian Doppler in 1842 in a paper explaining the observed periodic color changes of binary stars (a star system consisting of two stars orbiting around their common center of mass) [1]. In this hypothesis, the observed light from the star increases in frequency (blueshift) as the star is moving towards the earth and decreases in frequency (redshift) as the star is moving away from the earth. Therefore, the periodic frequency shift in the light emitted from a binary star is caused by periodic movement of a binary star. The value of the frequency shift f_D can be approximately calculated according to

$$f_D = \frac{v}{\lambda_0}, \quad (1.1)$$

where λ_0 is the light wavelength in a vacuum, and v is the relative velocity of the source towards the observer. This hypothesis was later confirmed by Ballot [2] with sound waves.

The Doppler shift can also be observed in a light wave that is reflected by a moving object. The corresponding frequency shift $f_D(t)$ is also linearly related to the instantaneous velocity $v(t)$ of the moving object relative to the observer, being described as

$$f_D(t) = 2 \frac{v(t)}{\lambda_0}. \quad (1.2)$$

This mechanism has been utilized in Doppler radar (RADIO Detection And Rang-

ing) systems to estimate the speed of aircraft or missiles, in which radio waves are used as the detection signal. The wavelength of the detection signal determines the minimum size of a detectable object. Therefore, radar cannot be used to detect an object with a very small geometric dimension, which limits the potential applications of Doppler radars. In order to acquire the movement information of tiny objects, such as particles in a fluid, a short wavelength is required. But this was not feasible until the invention of laser [3].

The first laser Doppler velocimeter in the optical range was proposed by Yeh *et al.* [4]. In their setup, coherent light at a wavelength $\lambda_0 = 632.8$ nm was used for detection, and this small wavelength allows the detection of monodispersed polystyrene spheres of diameter $0.556 \mu\text{m}$. A fluid flow can thus be estimated from the velocities of the spheres inside the fluid. This LDV employed a typical heterodyne-type optical coherent detection technique with the help of an optical interferometer. This heterodyne detection method is still widely used these days. Since this first demonstration, the LDV technique has drawn much attention and has been implemented with different optical arrangements: vom Stein *et al.* introduced a dual-beam mode LDV in 1969 [5]; Penny demonstrated a dual-scatter beam configuration [6]; the first fiber-based LDV was patented by Crosswy *et al.*; a self-mixing LDV was proposed by Rudd in 1968 [7]. These techniques are capable of measuring tiny vibrations or movements with particularly high spatial resolution, and thus have brought much attention in multiple industrial applications and research fields [8–14].

There are also many alternative techniques that can be used for vibration measurements, e.g. accelerometers. In an accelerometer, the acceleration is measured by converting the physical force $f(t) = ma(t)$ exerted on the sensing material to an electrical signal with the help of piezoelectricity, piezoresistivity or capacitive sensing, where m is the mass of the sensing material and $a(t)$ is its instantaneous acceleration [15]. However, these accelerometers have multiple drawbacks, including mass-loading effect [16] and narrow frequency range [15]. These problems have been successfully avoided by using the LDV technology thanks to its non-contact feature and flat frequency response. Nowadays, the calibration of accelerometers is based on the LDV technology [17].

1.1 Different arrangements of LDVs

Optical arrangements for LDVs are closely related to applications. For instance, single-point LDVs and scanning LDVs are usually used for surface-vibration measurement while dual-beam LDV configurations are commonly used for characterizing of fluid flow [18]. Therefore, we usually differentiate LDV technologies by using different names: “laser Doppler vibrometry” is used for surface-vibration measurement, while “laser Doppler velocimetry” and “laser Doppler anemome-

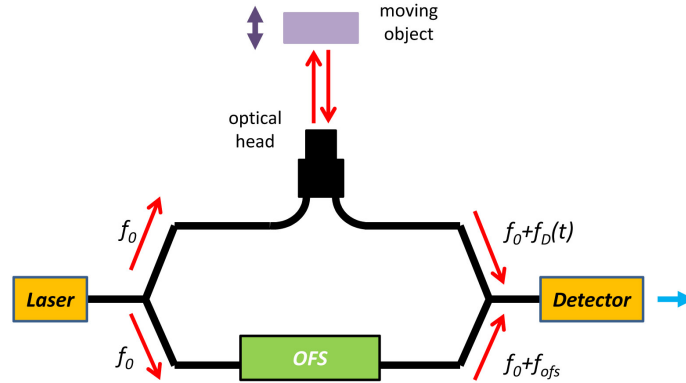


Figure 1.1: The schematic of a typical single-beam heterodyne-detection LDV. f_0 is the original frequency of the laser light, $f_D(t)$ is the instantaneous Doppler shift of the reflected light due to the target movement, and f_{ofs} is the frequency shift of the reference signal introduced by the optical frequency shifter (OFS).

try” are used for measurements of fluid flows. Most part of this thesis is devoted to the measurement of surface vibrations, which lies in the category of “vibrometry”. However, it is essential to realize the existence of different LDV arrangements. Therefore, a brief introduction to some popular optical arrangements for LDVs, e.g. single-beam and dual-beam LDVs, is given in this section.

1.1.1 Single-beam LDVs

A single-beam LDV realizes the velocity measurement with only one light beam. It is usually implemented in such a way that the light transmitting antenna (TA) and the light receiving antenna (RA) are integrated in one block, so as to keep the size of the optical head small. This optical arrangement is usually used to measure the out-of-plane velocity of a vibration. The interferometer of a single-beam LDV can be arranged to realize two typical detection schemes, namely heterodyne or homodyne, which are differentiated by whether an optical frequency shifter (OFS) is used in the interferometer.

Being used in the first demonstrated LDV system, the single-beam heterodyne-detection technique is still widely used nowadays. A typical single-beam heterodyne-detection LDV is schematically shown in figure 1.1. The signal is processed as follows. Light is first sent to the interferometer, where it is split into two arms, called the measurement arm (upper arm in figure 1.1) and reference arm (lower arm in figure 1.1), respectively. Light in the measurement arm is sent to a vibrating surface with the help of a TA in the optical head and an off-chip optical system (not depicted in figure 1.1). A portion of the light signal is reflected by the moving tar-

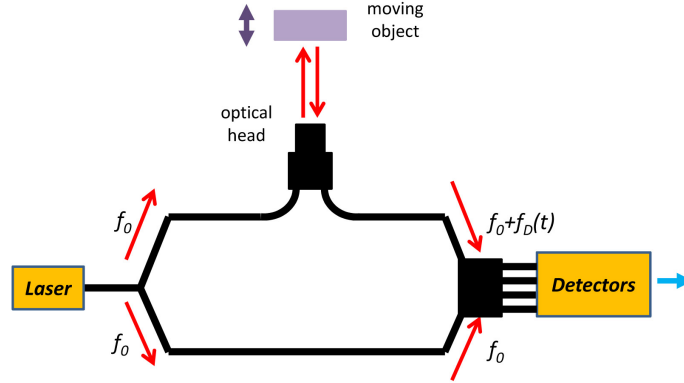


Figure 1.2: The schematic of a typical single-beam homodyne-detection LDV. f_0 is the original frequency of the laser light, and $f_D(t)$ is the instantaneous Doppler shift of the reflected light due to the target movement. A 90° optical hybrid with four photo-detectors are used in this system.

get and sent back to the optical head. According to the Doppler effect, this signal carries the information of the target's vibration in its modulated optical frequency. The reflected light is picked up by the RA in the optical head and coupled to the device again. Meanwhile, light in the reference arm undergoes a frequency shift of f_{ofs} with the help of the OFS. The recaptured reflection signal and the frequency shifted reference signal are combined in an optical combiner before being sent to a photo-detector. In the photo-detector, the optical signal is converted to an electrical signal, which is used for recovering the Doppler shift and hence the instantaneous out-of plane velocity of the vibration. The demodulation can be done directly with an FM demodulation or an in-phase & quadrature (IQ) demodulation based on a digital signal processing (DSP) approach.

In this configuration, the OFS in the reference arm is used to ensure that the carrier frequency of the photo-current signal does not lie in the low frequency region, where noise (e.g, $1/f$ noise) is significantly strong. This frequency shift is also helpful for the direction discrimination of the target's movement. The most usually used OFS is a Bragg cell, which creates the desired optical frequency shift using an acousto-optic effect [19, 20]. However, to realize an acousto-optical modulation may be difficult in some material systems. Hence other pseudo-heterodyne techniques have been proposed, either by using a ramp phase modulation (serrodyne) [21, 22], or with synthetic heterodyne techniques [23–25].

In a single-beam homodyne-detection LDV, the use of OFS is not required, which means that a homodyne LDV may be strongly influenced by low frequency noise. Hence, its measurement sensitivity may be lower than that of heterodyne. However, homodyne LDVs still have several strengths, including easy implemen-

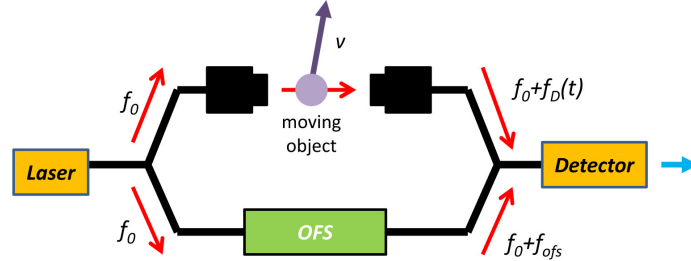


Figure 1.3: The schematic of a typical single-point heterodyne laser Doppler velocimeter used for measure fluid flow. f_0 is the original frequency of the laser light, and $f_D(t)$ is the instantaneous Doppler shift of the reflected light due to the target movement.

tation, low fabrication cost, and large measuring range of velocity. In addition, by implementing some special designs in the interferometer, e.g. a 90° optical hybrid [26], the homodyne demodulation quality can be improved. A typical arrangement of the single-beam homodyne-detection LDV is shown in figure 1.2. In this arrangement, the 90° optical hybrid is used to assist the demodulation.

A lot of applications are associated with single-beam LDVs, ranging from mechanics to biomedical researches. The applications include the evaluation of internal dynamic stress in a solid vibrating body [12], vibration of a burner [10], ground vibration [14], respiration vibration and cardiac period [27], tactile stiffness estimation [28], stapes velocity in live human ears [29] *et al.*

A single-beam LDV can also be implemented with separated TA and RA. This arrangement is desired when the velocity of a fluid is measured. Since the main application is not the vibration measurement, we'd rather call this a single-beam laser Doppler velocimeter. A schematic of such an LDV system based on heterodyne detection is shown in figure 1.3. An example is the reference beam LDV proposed by Yeh *et al.* [30]. This arrangement can also be implemented in homodyne.

There are several companies providing commercialized single-point LDV systems. The sensor head OFV-534 from Polytec[®] is a typical commercialized single-beam heterodyne-detection sensor head, while the RLE system from RENISHAW[®] is based on the homodyne detection.

1.1.2 Dual-beam LDVs

Another important LDV is the dual-beam arrangement, which is also named as the Doppler difference technique [18]. In this arrangement, both the reference and the measurement signals are sent to the moving target during the operation. A typical Doppler difference arrangement is shown in figure 1.4. In this figure, three possible positions of RAs are illustrated: *Detector 2* and *Detector 3* stand for the detectors set in the propagation directions of the reference and measurement sig-

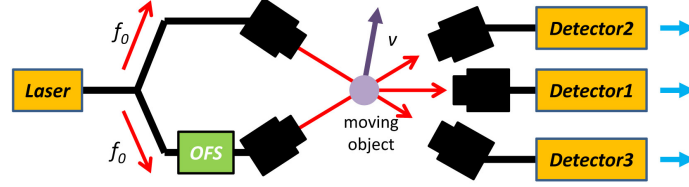


Figure 1.4: The schematic of a typical dual-beam LDV used for measuring fluid flow. f_0 is the original frequency of the laser light, and $f_D(t)$ is the instantaneous Doppler shift of the reflected light due to the target movement.

nals, respectively, while *Detector 1* is for detectors at any other locations. One can choose any of these three positions to receive scattered signal, but the demodulation techniques may be different from each other. An OFS can also be placed in one arm of the interferometer, so as to realize the optical heterodyne detection.

These dual-beam LDVs can be used to measure a fluid flow [31] or a surface vibration [5, 6]. They are more flexible in the optical arrangement, but the flexibility also makes this LDV bulky and difficult to build.

1.1.3 Self-mixing LDVs

A self-mixing LDV is a highly compact LDV system since it uses the laser cavity itself as the optical mixer. A typical self-mixing LDV arrangement is shown in figure 1.5(a). During the operation, light from a laser cavity is reflected by the moving target and coupled back to the laser cavity. It is found that the optical power in the laser cavity varies at a frequency equal to the Doppler frequency shift due to the vibration. By acquiring this optical power variation with a closely placed photodetector, one can recover the Doppler shift of the back-reflected signal. However, the shapes of these signals are complex and may vary strongly depending on the reflection power. A series of self-mixing photocurrent signals for different reflection power levels (represented by the factor C) is shown in figure 1.5(b), which is reproduced from [32]. According to the theory based on a three-mirror Fabry-Perot cavity [33, 34], the reflection power factor C can be calculated as [35]

$$C = \frac{\kappa s \sqrt{1 + \alpha^2}}{L_{las} n_{las}}, \quad (1.3)$$

$$\kappa = \frac{\epsilon(1 - R_2)}{\sqrt{AR_2}} \quad (1.4)$$

where s is the average distance of the target, α is the laser diode linewidth enhancement factor, L_{las} and n_{las} are the length and refractive index of the laser cavity, respectively, ϵ is a mismatch factor between the reflection and the lasing modes, A is the power loss in the external cavity, and R_2 is the reflectivity of

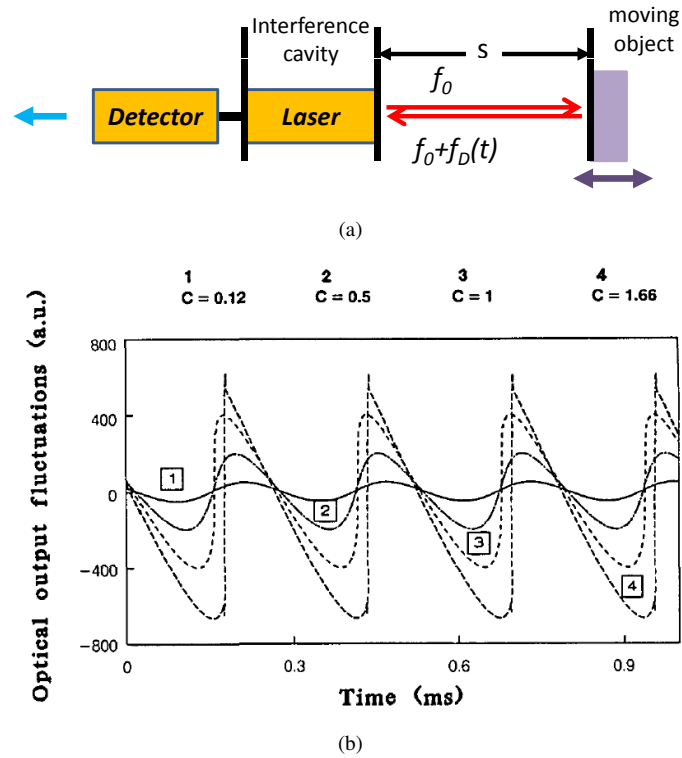


Figure 1.5: (a) The schematic of a typical self mixing LDV. (b) The output signals of a self-mixing LDV with different C parameter, reprinted from [32].

the laser output facet. It can be found from figure 1.5(b) that the influence of the C factor is significant, which may lead to complex demodulation algorithms. A simple fringe-counting method is the commonly used demodulation algorithm of self-mixing LDVs, but it has a bad displacement resolution of $\lambda_0/2$.

In spite of these modulation difficulties, self-mixing LDVs have been reported in a lot of publications thanks to their compact size and easy configurations. This technique can be used in liquid flow measurements [36], cardiovascular diagnostics [37], cantilever sensing [38] *et al.* However, it has not led to a well-sold product with a competitive price [39].

1.1.4 LDVs for multi-point measurements

In some applications, e.g. fluid turbulence measurement [40, 41], the velocity information of multiple positions is needed. For applications like the vibration measurement of a spinning blade (blade tip timing), the capability of changing the

measurement location is necessary [42, 43]. To fulfill these requirements, scanning LDV (SLDV) techniques have been introduced. With the help of a beam scanning system, SLDV can automatically relocate the position of the measurement light during the measurement. These scanning arrangements can be different for different applications [44, 45].

Multi-point vibration measurement may also be realized with a multi-beam measurement setup that can simultaneously retrieve the vibrations of multiple positions. Combining several stand-alone LDV devices may be the simplest method for realizing such a multi-beam LDV. A clever design has been reported by taking advantage of the multiple diffracted beams in an acousto-optic modulator [46, 47]. In this design, the multiple diffracted light beams (with different frequency shift) created in an acousto-optic (AO) modulator are focused to different positions on the target surface. Thanks to the frequency differences among these beams, the optical modulations of these beams are uncorrelated to each other since they belong to different carriers in the frequency domain. Therefore, these reflected signals can be combined into one signals and detected with only one photo-detector.

1.2 Key parameters of an LDV

Several important parameters of LDV are discussed in this section, including light wavelength, displacement resolution, maximum velocity, device size, detection distance, power consumption, output accuracy, and production cost. These parameters are important for judging the performance of a specific LDV system, and thus they will be often mentioned in the following parts of the thesis. Note that not all LDV parameters are discussed here.

Wavelength (λ_0): the wavelength of light. This value is determined by the optical property of the actually used material system. Conventionally used light wavelength is 632.8 nm (red light). However, Polytec[®] has found that increasing the light wavelength helps to reduce the influence of noise [48]. In their new product RSV-150, light at a wavelength of 1.55 μm is used.

Displacement resolution (d_r) and **velocity resolution** (v_r): the displacement/velocity resolution of an LDV indicates the minimal measurable displacement/velocity. This displacement resolution is usually limited by noise. Thanks to the use of an OFS, a heterodyne LDV normally has a better resolution than a homodyne LDV. The best displacement resolution of the OFV-5000 vibrometer controller from Polytec[®] is below 0.1 pm [49], while the RPI20 parallel interface from RENISHAW[®] has a $d_r = 28.6$ pm. Both d_r and v_r are frequency dependent, and they are correlated according to the following relation $v_r(f) = 2\pi f d_r(f)$.

Maximum velocity (v_m): due to system limitations, there is a maximum measurable velocity in the LDV outputs. The maximum velocity for a heterodyne system is determined by f_{ofs} , while for homodyne it is only limited by the sam-

pling frequency of demodulation. For Polytec[®] OFV-5000 with $f_{ofs} = 40$ MHz, the maximal velocity $v_m = 10$ m/s. For homodyne LDV, the maximal velocity is limited by the sampling frequency and electronic bandwidth. For the RPI20 parallel interface from RENISHAW[®], $v_m \approx 2$ m/s. Note that this value for the homodyne case can be greatly enhanced with improved electronic designs.

Frequency range: The frequency range of an LDV indicates the minimal and the maximal frequency of a measurable mechanical vibration.

Device size: The size here especially means the size of the optical head, which is critical for applications with limited space used for measurement. For example, a very compact size is required when one wants to place the LDV in the ear to measure the vibration of the ear drum. When multiple LDVs are used to measure the vibration distribution of a surface with small size, the size of each LDV should also be very small.

Detection distance (L_D): The detection distance L_D indicates the maximal distance between the LDV and the target that still supports a high quality vibration detection, and it is determined by the numerous factors, including the power of the input laser light, the reflectivity of the target surface (or scattering particles), and the coherence length of the optical signal. With a carefully designed optical system, the detection distance can be very large. For instance, the RSV-150 from Polytec[®] has a detection distance of 300 m.

Power consumption (P_{ldv}): The power consumption is essential for portable LDVs. The power can be consumed by different components of the LDV, including the laser source, photo-detectors, demodulation electronics, temperature controller, and other auxiliary components. For a heterodyne LDV, the OFS is also an important power consuming component. The conventionally used acousto-optical modulator (AOM) may consume a great amount of power (up to several watt). Thus replacing the AOM with a low-power component may greatly reduce the power consumption compared to conventional LDV devices.

Output accuracy (δ_{ldv}): The output accuracy of the LDV is an important parameter for characterizing the loyalty of the LDV output to the real signal. We usually use the root-mean-square deviation of the displacement output as the output accuracy.

Production cost: Unlike those previously mentioned parameters, production cost is a commercial concern of an LDV system. Customers require a high-performance device as well as a low price of the product. The cost issue is the initial impetus of this thesis work. In this thesis, we try to reduce the production cost of LDV systems by integrating them on chips.

Some important parameters of several LDV manufacturers are listed in Table 1.1.

Company	Heterodyne Homodyne	v_m	frequency range	λ_0
Polytec [50]	Heterodyne @40 MHz	10 m/s	Up to 24 MHz	632.8 nm & 1550 nm
RENISHAW [51]	Homodyne	<2 m/s	not for vibration	632.8 nm
Metrolaser [52]	Heterodyne @10.7 MHz	800 mm/s	0-40 kHz	780 nm & 650 nm
Sintec Optronics [53]	-	3 m/s	1-100 kHz	632.8 nm
Ono Sokki [54]	Heterodyne	20 m/s	0.3 Hz-3 MHz	632.8 nm
Brüel & Kjær [55]	Homodyne	425 mm/s	0.1 Hz 25 kHz	632.8 nm

Table 1.1: Summary of different commercial LDVs.

1.3 Silicon-on-insulator (SOI) platform

We propose to integrate an LDV on the silicon-on-insulator (SOI) substrate, a promising platform for highly-miniaturized and low-cost photonic integrated circuits (PICs). The footprint of the PIC is determined by the size and bend radius of optical waveguides, which is the most basic optical component in PICs. A most commonly used single-mode rib waveguide has a cross section with a width of 450 nm and a height of 220 nm. Because of the high index-contrast between the core and cladding materials ($n_{core} = 3.478$, $n_{cladding} = 1.45$), the waveguide bend can be reduced to 2 μm with a negligible optical loss [56], and this ensures a compact circuit footprint by introducing more flexible waveguide links and bends. This waveguide structure can be fabricated using the 193 nm DUV lithography technology [57]. The SEM image of a fabricated waveguide bend is illustrated in figure 1.6. Based on the waveguide technology, multiple basic integrated optical components with small foot-print have been realized and demonstrated, such as Y-junction splitters/combiners, directional couplers, multi-mode interference couplers [58], micro-ring resonators, arrayed-waveguide gratings, optical reflectors, grating couplers [59–62], carrier-depletion based phase modulators [63], Ge-based photo-detectors [64], integrated optical isolators [65], adhesive bonded distributed-feedback (DFB) lasers [66]. It includes almost everything required in an LDV system. As a result, the miniaturization LDV is possible on this platform.

A conception design of a fully integrated heterodyne LDV (optical part) based on the SOI-platform is schematically shown in figure 1.7. The laser source, photo-detectors, and optical frequency shifters are integrated in on-chip Mach-Zehnder interferometer, and form the key part of a single-beam heterodyne-detection LDV. The measurement light beam is sent out of the chip via a grating coupler. Outside of the chip, an imaging optical system is used to focus the out-coupled measuring light beam to the vibrating target. Reflected light is coupled back to the same

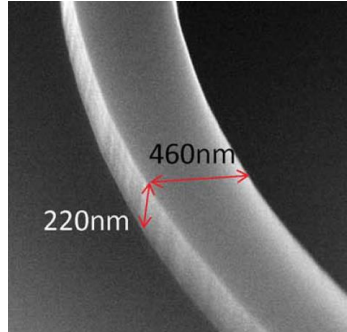


Figure 1.6: The SEM image of a waveguide bend on the silicon-on-insulator platform. Adapted from [67].

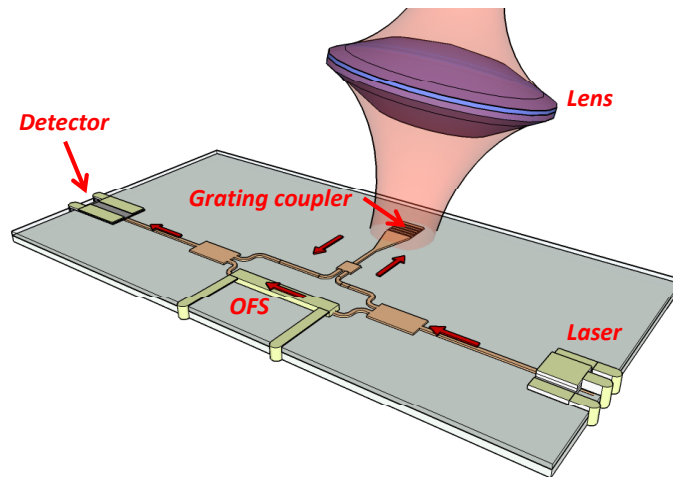


Figure 1.7: The 3d schematic of a heterodyne LDV integrated on SOI.

grating coupler. The reflected signal is mixed with the frequency shifted reference signal in an optical combiner on the chip, then the combined signal is received by on-chip photo-detectors. The demodulator can be an electric circuit integrated next to the PIC. Based on this basic structure, we can also realize other types of LDVs on SOI, i.e. homodyne LDV and multi-point LDV.

Sometimes the laser source can be implemented externally, if a fully integrated version is not required. In this case, a fiber or fiber array can be used to connect the laser and the optical chip. This semi-integrated LDV is usually a reasonable solution when the integration technique of the laser is difficult and expensive. Although this method may increase the packaging cost, it provides a benefit that the heat generated from the laser does not influence the performance of the interfer-

ometer. In this thesis, we will focus on this semi-integrated LDV.

1.4 Contents and outline

In this thesis, the focus is on realizing proof-of-concept designs of miniaturized LDVs based on SOI technology. Because of the complicated processing steps of an integrated laser and photo-detectors, we decide to test only the on-chip interferometers for the first step. In this thesis, we will analytically check the working principles of different on-chip LDVs, and try to pinpoint the existing influential factors.

The major problems with the on-chip LDV system are the spurious reflection at the interfaces where large mode-mismatch occurs and an imperfect optical frequency shift for the heterodyne technique. The LDV circuit is also sensitive to temperature variations. However, the influence of the temperature variation is problematic only when a strong spurious reflection exists in the interferometer. To deal with these problems, on one hand we will demonstrate reflectionless designs for some important on-chip optical components, on the other hand two different methods to realize an OFS with highly suppressed sidebands are analyzed. With these devices, two typical single-beam LDV configurations, heterodyne and homodyne, are realized and reported. A dual-LDV PIC design used for the arterial pulse wave velocity (PWV) measurement is also demonstrated.

This thesis is organized as follows. In Chapter 2, we mainly focus on the theoretical analysis of an on-chip LDV. The basic blocks of an on-chip LDV, two typical LDV detection schemes (homodyne and heterodyne), demodulation algorithms, and the influence of different deviation sources are discussed and analyzed in this chapter. Chapter 3 focuses on reflectionless optical component designs, including reflectionless grating couplers and reflectionless multi-mode interference couplers. In Chapter 4, methods of integrating optical frequency shifters on SOI are discussed. Designs and experimental results for several fabricated on-chip homodyne and heterodyne LDVs are demonstrated and analyzed in Chapter 5. In Chapter 6, the arterial PWV measurement measured with an on-chip dual homodyne LDV is reported. Finally, we conclude the thesis.

1.5 Publications

1.5.1 Publications in international journals

1. **Y. Li**, P. Segers, J. Dirckx, and R. Baets, *Miniaturized dual homodyne laser Doppler vibrometer on silicon-on-insulator for arterial pulse wave velocity measurement*, Biomedical Optics Express, 4(7), p.1229-1235 (2013).

2. **Y. Li** and R. Baets, *Homodyne laser Doppler vibrometer on silicon-on-insulator with integrated 90 degree optical hybrids*, Optics Express, 21(11), p.13342-13350 (2013).
3. **Y. Li**, L. Li, B. Tian, G. Roelkens, and R. Baets, *Reflectionless tilted grating couplers with improved coupling efficiency based on a silicon overlay*, IEEE Photonics Technology Letters, 25(13), p1195-1198 (2013).
4. **Y. Li**, S. Verstuyft, G. Yurtsever, S. Keyvaninia, G. Roelkens, D. Van Thourhout, and R. Baets, *Heterodyne laser Doppler vibrometers integrated on silicon-on-insulator with thermo-optic based frequency shifters*, Applied Optics, 52(10), p.2145-2152 (2013).
5. **Y. Li**, D. Vermeulen, Y. De Koninck, G. Yurtsever, G. Roelkens, and R. Baets, *Compact grating couplers on silicon-on-insulator with reduced backreflection*, Optics Letters, 37(21), p.4356-4358 (2012).
6. D. Vermeulen, Y. De Koninck, **Y. Li**, W. Bogaerts, R. Baets, and G. Roelkens, *Reflectionless grating couplers for SOI photonic integrated circuits*, Optics Express, p.22278-22283 (2012).
7. H. Yu, M. Pantouvaki, J. Van Campenhout, D. Korn, K. Komorowska, P. Dumon, **Y. Li**, P. Verheyen, P. Absil, L. Alloatti, D. Hillerkuss, J. Leuthold, R. Baets, and W. Bogaerts, *Performance tradeoff between lateral and interdigitated doping patterns for high speed carrier-depletion based silicon modulators*, Optics Express, 20(12), p.12926-12938 (2012).
8. L. Wang, **Y. Li**, M. Porcel, D. Vermeulen, X. Han, J. Wang, X. Jian, R. Baets, M. Zhao, and G. Morthier, *A polymer-based surface grating coupler with an embedded Si₃N₄ layer*, Journal of Applied Physics, 111(11), p.114507 (2012).
9. **Y. Li**, S. Meersman, and R. Baets, *Realization of fiber based laser Doppler vibrometer with heterodyne frequency shifting*, Applied Optics, 50(17), p.2809 (2011).

1.5.2 Patents

1. R. Baets, D. Vermeulen, **Y. Li**, and Y. De Koninck, *Integrated photonics waveguide grating coupler*, WO/2013/037900, 22 March (2013).

1.5.3 Publications in international conferences

1. L. Li, **Y. Li**, G. Morthier, *Properties of shallowly etched second order grating in silicon-on-insulator (SOI) waveguide*, 2013 Annual Workshop of the IEEE Photonics Benelux Chapter, Belgium, p.23-24 (2013).

2. W. Bogaerts, **Y. Li**, S. Pathak, A. Ruocco, M. Fiers, A. Ribeiro, E. Lambert, and P. Dumon, *Integrated design for integrated photonics: from the physical to the circuit level and back*, Proc. SPIE 8781, Integrated Optics: Physics and Simulations (invited), Czech Republic, p.878102 (2013)
3. G. Roelkens, D. Vermeulen, **Y. Li**, Y. De Koninck, S. Selvaraja, K. Van Acoleyen, D. Van Thourhout, and R. Baets, *High index contrast gratings for silicon photonic integrated circuits*, Photonics West 2013 (invited), United States, (2013).
4. **Y. Li** and R. Baets, *Single-channel laser Doppler vibrometers integrated on silicon-on-insulator (SOI)*, 5th International Conference on Optical Measurement Techniques for Structures & Systems, Belgium, p.235 (2012)
5. **Y. Li**, S. Verstuyft, G. Yurtsever, S. Keyvaninia, G. Roelkens, D. Van Thourhout, and R. Baets, *Miniaturized laser Doppler vibrometers integrated on silicon-on-insulator with thermo-optic serrodyne optical frequency shifter*, 9th International Conference on Group IV Photonics, United States, p.219-221 (2012)
6. L. Wang, **Y. Li**, M. Porcel, D. Vermeulen, X. Han, J. Wang, X. Jian, M. Zhao, and G. Morthier, *Grating couplers in polymer with a thin Si₃N₄ layer embedded*, SPIE Photonics West 2012, United States, p.8258 (2012)
7. **Y. Li**, D. Vermeulen, Y. De Koninck, G. Yurtsever, G. Roelkens, and R. Baets, *Fiber couplers for silicon-on-insulator photonic IC with optimized on-chip return loss*, Optical Fiber Communication Conference (OFC) 2012, p.JTh2A.8 (2012)
8. **Y. Li** and R. Baets, *Improved multi-mode interferometers (MMIs) on silicon-on-insulator with the optimized return loss and isolation*, Proceedings of the 2011 annual symposium of the IEEE Photonics Benelux Chapter, p. 205-208, (2011)
9. D. Vermeulen, Y. De Koninck, **Y. Li**, E. Lambert, W. Bogaerts, R. Baets, and G. Roelkens, *Reflectionless Grating Coupling for Silicon-on-Insulator Integrated Circuits*, 2011 IEEE 8th International Conference on Group IV Photonics (GFP), United Kingdom, p.74-76 (2011)
10. **Y. Li**, S. Meersman, and R. Baets, *Optical frequency shifter on SOI using thermo-optic serrodyne modulation*, 2010 7th IEEE International conference on group IV photonics, China, p.75-77 (2010)
11. **Y. Li** and R. Baets, *Miniaturized laser doppler velocimeters (LDVs) integrated on silicon-on-insulator (SOI)*, Proceedings of the 2009 Annual Symposium of the IEEE Photonics Benelux Chapter, Belgium, p.97-100 (2009)

1.5.4 Publications in national conferences

1. **Y. Li**, *Miniaturized laser doppler vibrometers on SOI*, FEA PhD symposium, 12th. p.95-95 (2011)
2. **Y. Li**, *Miniaturized laser doppler velocimeters (LDVs) integrated on silicon-on-insulator (SOI)*, Ugent-Firw Doctoraatssymposium, 10e, Belgium, (2009)

References

- [1] C. Doppler. *Über das farbige Licht der Doppelsterne und einiger anderer Gestirne des Himmels*, 1842.
- [2] B. Buys. *Akustische Versuche auf der Niederländischen Eisenbahn, nebst gelegentlichen Bemerkungen zur Theorie des Hrn. Prof. Doppler*. *Annalen der Physik und Chemie*, 11:321–351, 1845.
- [3] T. H. Maiman. *Stimulated Optical Radiation in Ruby*. *Nature*, 187:493–494, 1960.
- [4] Y. Yeh and H. Z. Cummins. *Localized Fluid Flow Measurements With an He-Ne Laser Spectrometer*. *Applied Physics Letters*, 4(10):176–178, 1964.
- [5] H. D. vom Stein and H. J. Pfeifer. *A Doppler difference method for velocity measurements*. *Metrologia*, 5:59, 1969.
- [6] C. M. Penney. *Differential Doppler Velocity Measurements*. *IEEE Journal of Quantum Electronics*, 5(6):318, 1969.
- [7] M. J. Rudd. *A laser Doppler velocimeter employing the laser as a mixer-oscillator*. *Journal of Physics E: Scientific Instruments*, 1(7):723–726, July 1968.
- [8] Y. Zhong, G. Zhang, C. Leng, and T. Zhang. *A differential laser Doppler system for one-dimensional in-plane motion measurement of MEMS*. *Measurement*, 40(6):623–627, July 2007.
- [9] S. Weissner and F. E. Talke. *Load/unload measurements using laser doppler vibrometry and acoustic emission*. *Tribology International*, 33(5-6):367–372, May 2000.
- [10] N. Paone and G. M. Revel. *Laser vibration measurements through combusive flows: application to an industrial burner in working conditions*. *Measurement*, 28(1):21–31, July 2000.
- [11] M. Leutenegger, E. Martin-Williams, P. Harbi, T. Thacher, W. Raffoul, M. André, A. Lopez, P. Lasser, and T. Lasser. *Real-time full field laser Doppler imaging*. *Biomedical Optics Express*, 2(6):1470–7, June 2011.
- [12] S. D. Holland, J. Renshaw, and R. Roberts. *Measurement of dynamic full-field internal stresses through surface laser Doppler vibrometry*. *Applied Physics Letters*, 91(13):134101, 2007.

-
- [13] T. Guo, H. Chang, J. Chen, X. Fu, and X. Hu. *Micro-motion analyzer used for dynamic MEMS characterization*. Optics and Lasers in Engineering, 47(3-4):512–517, March 2009.
- [14] W. P. Arnott and J. M. Sabatier. *Laser-Doppler vibrometer measurements of acoustic to seismic coupling*. Applied Acoustics, 30:279–291, 1990.
- [15] <http://www.new.mmf.de/introduction.htm>.
- [16] P. Castellini and E. P. Tomasini. *Image-based tracking laser Doppler vibrometer*. Review of Scientific Instruments, 75(1):222, 2004.
- [17] G. W. Vogl, K. K. Harper, B. Payne, and E. P. Tomasini. *Modeling and Experimental Analysis of Piezoelectric Shakers for High-Frequency Calibration of Accelerometers*. In The 9th International Conference on Vibration Measurements by Laser and Noncontact Techniques and Short Course, pages 383–394, 2010.
- [18] T. O. H. Charrett, S. W. James, and R. P. Tatam. *Optical fibre laser velocimetry: a review*. Measurement Science and Technology, 23(3):032001, March 2012.
- [19] Z. Zhang. *LDA Application Methods: Laser Doppler Anemometry for Fluid Dynamics*. Springer Verlag, 2010.
- [20] A. T. Waz, P. R. Kaczmarek, and K. M. Abramski. *Laser-fibre vibrometry at 1550 nm*. Measurement Science and Technology, 20(10):105301, October 2009.
- [21] D. A. Jackson, R. Priest, A. Dandridge, and A. B. Tveten. *Elimination of drift in a single-mode optical fibre interferometer using a piezo-electrically stretched coiled fibre*. Applied optics, 19:2926–9, 1980.
- [22] H. Toda, M. Haruna, and H. Nishihara. *Optical integrated circuit for a fiber laser doppler velocimeter*. Journal of Lightwave Technology, 5(7):901–905, 1987.
- [23] A. C. Lewin, A. D. Kersey, and D. A. Jackson. *Non-Contact surface vibration analysis using a monomode fibre optic interferometer incorporating an open air path*. Journal of Physics E: Scientific Instruments, 18:604, 1985.
- [24] Y. L. Lo and C. H. Chuang. *New synthetic-heterodyne demodulator for an optical fiber interferometer*. IEEE Journal of Quantum Electronics, 37(5):658–663, May 2001.

- [25] S. Kang, J. La, H. Yoon, and K. Park. *A synthetic heterodyne interferometer for small amplitude of vibration measurement*. The Review of scientific instruments, 79(5):053106, May 2008.
- [26] L. Zimmermann, K. Voigt, G. Winzer, K. Petermann, and C. M. Weinert. *C-Band Optical 90-Hybrids Based on silicon-on-insulator 4×4 waveguide couplers*. IEEE Photonics Technology Letters, 21(3):143–145, 2009.
- [27] L. Scalise, P. Marchionni, I. Ercoli, and E. P. Tomasini. *Simultaneous measurement of respiration and cardiac period in preterm infants by laser Doppler vibrometry*. In 10th International Conference on Vibration Measurements by Laser and Noncontact Techniques, volume 275, pages 275–281, Aivela, 2012.
- [28] L. Scalise, M. Memeo, F. Cannella, M. Valente, D. G. Caldwell, and E. P. Tomasini. *Laser application on haptics: Tactile stiffness measurement*. In 10th International Conference on Vibration Measurements by Laser and Noncontact Techniques, volume 287, pages 287–293, Aivela, 2012.
- [29] W. Chien, J. J. Rosowski, M. E. Ravicz, S. D. Rauch, J. Smullen, and S. N. Merchant. *Measurements of stapes velocity in live human ears*. Hearing research, 249(1-2):54–61, March 2009.
- [30] Y. Yeh and H.Z. Cummings. *Localised fluid flow measurements with a HeNe spectrometer*. Applied Physics Letters, 4:176–178, 1964.
- [31] W. T. Mayo Jr. *Simplified laser Doppler velocimeter optics*. Journal of Physics E: Scientific Instruments, 3:235–237, 1970.
- [32] M. H. Koelink, M. Slot, F. F. de Mul, J. Greve, R. Graaff, A. C. Dassel, and J. G. Aarnoudse. *Laser Doppler velocimeter based on the self-mixing effect in a fiber-coupled semiconductor laser: theory*. Applied Optics, 31(18):3401–3408, June 1992.
- [33] P. J. De Groot, G. M. Gallatin, and S. H. Macomber. *Ranging and velocimetry signal generation in a backscatter-modulated laser diode*. Applied Optics, 27(21):4475–4480, 1988.
- [34] W. M. Wang, K. T. V. Grattan, A. W. Palmer, and W. J. O. Boyle. *Self-mixing interference inside a single-mode diode laser for optical sensing applications*. Journal of Lightwave Technology, 12(9):1577–1587, 1994.
- [35] G. Giuliani, M. Norgia, S. Donati, and T. Bosch. *Laser diode self-mixing technique for sensing applications*. Journal of Optics A: Pure and Applied Optics, 4(6):S283–S294, November 2002.

-
- [36] F. F. M. Mul, M. H. Koelink, and A. L. Weijers. *Self-mixing laser-Doppler velocimetry of liquid flow and of blood perfusion in tissue*. *Applied optics*, 31(27):5844–5851, 1992.
- [37] K. Meigas, H. Hinrikus, R. Kattai, and J. Lass. *Self-mixing in a diode laser as a method for cardiovascular diagnostics*. *Journal of Biomedical Optics*, 8(1):152–60, January 2003.
- [38] D. Larsson, A. Greve, and J. M. Hvam. *Self-mixing interferometry in VCSELs for nanomechanical cantilever sensing*. In *Conference on Lasers and Electro-Optics*, page CMG2, Baltimore, 2009.
- [39] personal communication with Dr. Christian Rembe from Polytec, 2013.
- [40] O. Ivanchenko, E. Esirgemez, and S. Ölçmen. *A miniature three-component LDV probe*. *Measurement Science and Technology*, 18(7):2014–2020, July 2007.
- [41] S. Vanlanduit, F. Prezniak, R. Longo, C. Vuye, P. Guillaume, and E. P. Tomasini. *Fluid flow measurements using a scanning laser Doppler vibrometer*. In *The 9th International Conference on Vibration Measurements by Laser and Noncontact Techniques and Short Course*, pages 123–130, 2010.
- [42] J.-F. Brouckaert, R. Marsili, G. Rossi, and R. Tomassini. *Development and experimental characterization of a new non contact sensor for blade tip timing*. In *10th International Conference on Vibration Measurements by Laser and Noncontact Techniques*, volume 61, pages 61–68, AIVELA, 2012.
- [43] U. Pfeifer and M. Zidorn. *Tip timing measurement chain validation with the Universal Tip Timing Calibrator UTTC, approach and experience*. In *10th International Conference on Vibration Measurements by Laser and Noncontact Techniques*, volume 43, pages 43–51, AIVELA, 2012.
- [44] C. Rembe and A. Drabenstedt. *Laser-scanning confocal vibrometer microscope: Theory and experiments*. *Review of Scientific Instruments*, 77(8):083702, 2006.
- [45] A Stanbridge. *Modal Testing Using a Scanning Laser Doppler Vibrometer*. *Mechanical Systems and Signal Processing*, 13(2):255–270, March 1999.
- [46] Y. Fu, M. Guo, and P. B. Phua. *Multipoint laser Doppler vibrometry with single detector: principles, implementations, and signal analyses*. *Applied Optics*, 50(10):1280–8, April 2011.
- [47] E. Li, J. Xi, J Chicharo, J. Yao, and D. Yu. *Multi-point laser Doppler velocimeter*. *Optics Communications*, 245(1-6):309–313, January 2005.

- [48] A. Drabenstedt, J. Sauer, and C. Rembe. *Remote-sensing vibrometry at 1550 nm wavelength*. In 19th International conference on Vibration Measurements by Laser and Noncontact Techniques, volume 113, pages 113–121, AIVELA, 2012.
- [49] Polytec. *Vibrometer Controller OFV-5000: User Manual*.
- [50] Polytec. *Data sheet: VD/DD Decoder Guideline*, 2013.
- [51] RENISHAW. *Data sheet: RLE system performance*, 2013.
- [52] MetroLaser Inc. *VibroMet 500V Laser Doppler Vibrometer: Specifications*, 2013.
- [53] Sintec Optronics. *Laser Doppler Vibrometer*, 2013.
- [54] Ono Sokki. *Laser Doppler Vibrometer LV-1800*, 2013.
- [55] Brüel & Kjær. *Product Data: Laser Doppler Vibrometer Type 8329*, 2013.
- [56] S. K. Selvaraja, W. Bogaerts, and D. Van Thourhout. *Loss reduction in silicon nanophotonic waveguide micro-bends through etch profile improvement*. Optics Communications, 284(8):2141–2144, April 2011.
- [57] <http://www.epxfab.eu>.
- [58] R. Halir, G. Roelkens, A. Ortega-Moñux, and J. G. Wangüemert-Pérez. *High-performance 90 hybrid based on a silicon-on-insulator multimode interference coupler*. Optics Letters, 36(2):178–80, January 2011.
- [59] D. Taillaert, P. Bienstman, and R. Baets. *Compact efficient broadband grating coupler for silicon-on-insulator waveguides*. Optics Letters, 29(23):2749–2751, 2004.
- [60] G. Roelkens, D. Van Thourhout, and R. Baets. *High efficiency Silicon-on-Insulator grating coupler based on a poly-Silicon overlay*. Optics Express, 14(24):11622–11630, 2006.
- [61] F. Van Laere, T. Claes, and J. Schrauwen. *Compact focusing grating couplers for silicon-on-insulator integrated circuits*. IEEE Photonics Technology Letters, 19(23):1919–1921, 2007.
- [62] D. Vermeulen, S. Selvaraja, P. Verheyen, G. Lepage, W. Bogaerts, P. Absil, D. Van Thourhout, and G. Roelkens. *High-efficiency fiber-to-chip grating couplers realized using an advanced platform*. Optics Express, 18(17):18278–18283, 2010.

-
- [63] H. Yu, W. Bogaerts, and A. De Keersgieter. *Optimization of ion implantation condition for depletion-type silicon optical modulators*. IEEE Journal of Quantum Electronics, 46(12):1763–1768, 2010.
- [64] L. Vivien, J. Osmond, J.-M. Fédéli, D. Marris-Morini, P. Crozat, J.-F. Damlencourt, E. Cassan, Y. Lecunff, and S. Laval. *42 GHz p.i.n Germanium photodetector integrated in a silicon-on-insulator waveguide*. Optics Express, 17(8):6252–7, April 2009.
- [65] S. Ghosh, S. Keyvaninia, Y. Shoji, W. Van Roy, G. Roelkens, and R. Baets. *Compact Mach-Zehnder Interferometer Ce: YIG/SOI Optical Isolators*. IEEE Photonics Technology Letters, 24(18):1653–1656, 2012.
- [66] S. Stankovic, R. Jones, M. N. Sysak, J. M. Heck, G. Roelkens, and D. Van Thourhout. *Hybrid III-V/Si Distributed-Feedback Laser Based on Adhesive Bonding*. IEEE Photonics Technology Letters, 24:2155–2158, 2012.
- [67] W. Bogaerts and S. K. Selvaraja. *Compact Single-Mode Silicon Hybrid Rib/Strip Waveguide With Adiabatic Bends*. IEEE Photonics Journal, 3(3):422–432, 2011.

2

Working principle of on-chip LDVs

As is mentioned above, a laser Doppler vibrometer (LDV) is an optical coherent detection system consisting of different electrical and optical components, e.g. laser sources and photo-detectors. The performance of an LDV is strongly related to the properties of these basic components. However, the influence of a certain component on the whole system may vary for different system configurations. For instance, the low frequency noise in a photodetector causes a critical deviation in the output signals of a homodyne LDV, while it may not be a major concern in heterodyne LDV since low frequency noise is filtered out. So it is important to understand the influence of each component on each specific LDV system. In this chapter, we will focus on two different detection schemes, namely homodyne and heterodyne, and theoretically analyze their performance degradations when non-ideal components are used. The main system concern in this chapter is the output accuracy and displacement resolution, while other system parameters, e.g. power consumption and device size, will be mentioned afterwards in this thesis. The discussions in this chapter are mainly focused on the problems of on-chip LDVs, but it can also be extended to a general LDV system.

This chapter is organized as follows. The descriptions of all building blocks in an LDV system are firstly described. Then, the demodulation methods corresponding to the homodyne and heterodyne detection schemes are separately introduced and analyzed. With a digital signal processing (DSP) based approach, we will show several demodulation algorithms. Meanwhile, some efficient compensation methods for those deviation problems with integrated LDVs, e.g. on-chip spurious reflections, are also demonstrated.

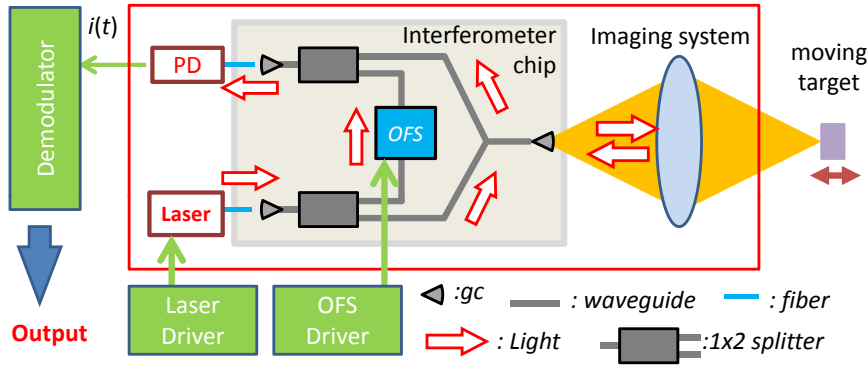


Figure 2.1: The schematic of a typical heterodyne on-chip LDV, in which **PD** stands for photodetector, **OFS** for optical frequency shifter, **gc** for grating coupler.

2.1 Basic building blocks

The schematic of a typical on-chip LDV is in figure 2.1, which is divided into two parts: the photonic part (in the red box) and the electronic part. The photonic part usually consists of a laser source, a photo-detector (PD), an interferometer, and an imaging system. In a heterodyne system, an optical frequency shifter (OFS) is also included. The electronic part basically consists of a demodulator and the driving circuits for the laser, the PD, and the OFS. Descriptions of these components will be given in this section. Note that there will be no dedicated sections for the drivers in this thesis.

The signal process of the LDV is briefly described as follows. During operation, coherent light is generated from the laser source and sent to the interferometer, where it is split by an optical splitter into two parts: the measurement and the reference signals. The measurement signal is sent to the vibrating target with the help of an imaging system. After being reflected by the target, the measurement signal is recaptured and sent back to the measurement arm again. Meanwhile, the reference signal either undergoes a frequency shift (heterodyne) or remains intact (homodyne). The reference and measurement signals are recombined in an optical combiner and sent to a PD, where the information of the Doppler shift in the measurement signal is converted into an intensity variation in the photocurrent. A demodulator is then used to recover the measured Doppler shift, and hence the instantaneous velocity (or displacement) of the target is obtained. In the following part, each component will be discussed separately.

2.1.1 Laser source

The coherent light signal generated from the laser source is denoted as

$$E_0(t) = A \exp(i2\pi f_0 t), \quad (2.1)$$

where A is the amplitude of the electric field, $f_0 = c/\lambda_0$ is the frequency of light, c is the speed of light in a vacuum, and λ_0 is the light wavelength in vacuum.

For SOI-based on-chip LDVs, the signal used for detection is infrared light ($\lambda_0 = 1.55 \mu\text{m}$) rather than the conventionally used red light ($\lambda_0 = 632.8 \text{ nm}$), for example, in OFV-534 in Polytec[®] [1]. This wavelength lies in the C-band (1530-1565 nm), where many low-cost optical components can be found. Most integrated optical components on SOI are also dedicated to this band [2]. Besides, the low photon energy of infrared light at 1550 nm substantially increases the carrier-to-noise-ratio (CNR) compared to the red light [3]. This wavelength is also basically safe for the retina. That's because light with this wavelength is strongly absorbed in the water in the eye. Therefore, it has less chance to damage the retina. For $\lambda_0 = 1.55 \mu\text{m}$, the minimal optical power allowed as the eye safe laser class 1 by the DIN/IEC 60825 laser safety norm is 10 mW, which is 10 times as much as that for $\lambda_0 = 632.8 \text{ nm}$ [3].

As is already mentioned in Chapter 1, the light signal used for the vibration measurement should have a good temporal coherence, so that the coherence length of the light L_c is much longer than the optical path difference between the measurement and the reference arm in the LDV interferometry. The coherence length L_c is determined by the phase noise of the laser, being described by the linewidth of the laser $\Delta\lambda$:

$$L_c = K \frac{\lambda_0^2}{\Delta\lambda}, \quad (2.2)$$

where K is a constant defined by the lineshape of the laser spectrum, e.g. $K = 0.32$ for a Lorentzian lineshape [4]. A distributed feedback (DFB) laser is normally used as the laser source because it usually has a narrow linewidth. Since the reference arm of the interferometer is implemented on chip and is very short, the optical path difference of these two signals is determined by the detection distance L_D . To ensure the coherence, the relation $L_D \leq L_c/2$ should be fulfilled. A typical DFB laser with a linewidth of 2 MHz has a coherence length of around 50 m, which indicates that $L_D \leq 25 \text{ m}$.

The indirect bandgap of silicon makes it incapable of generating stimulated emissions. However, it is still desired to integrate the laser sources with the other components on the same SOI chip in many applications. Therefore, a lot of efforts have been made to realize such an integration on SOI [5, 6]. In this thesis, however, we try to avoid this integration and use external laser sources instead. That's because external lasers can be easily characterized and have no thermal influence

on the interferometer's performance. Coherent light can be sent to the chip via a fiber from the external laser source.

2.1.2 Interferometer

The light signal is directly sent to the on-chip interferometer from the laser source. The major function of the interferometer is to create a combined light signal, of which the beat frequency is linearly related to the instantaneous velocity of the vibrating target. In our proposed design, the interferometer is realized with on-chip optical waveguides, optical splitters/combiners and grating couplers.

The rib waveguides used in the system is a single-mode waveguide (220 nm thick and 450 nm wide) for 1550 nm coherent light with a propagation loss of around 2.7 dB/cm [7]. Thanks to the high index contrast between the waveguide core ($n=3.47$) and the cladding ($n=1$), the waveguide bend radius can be reduced to 2 μm with no apparent loss (0.028 dB/90° [7]). This small waveguide bend ensures a largely reduced PIC footprint and leads to a lower production cost.

The optical splitters/combiners can also be realized using the waveguide technology on SOI. Typically used optical splitter/combiners are Y-junctions, directional couplers, 1×2 multimode interference (MMI) couplers, and 2×2 MMI couplers [8]. Sometimes we also use 2×4 MMI couplers, which will be discussed later as a 90° optical hybrid [9]. The working mechanism of the 2×2 MMI is described as follows. After light is launched from the two input ports of an MMI into the multimode section, different modes will be excited and propagate to the output side with different phase velocities. According to the self-imaging theory [10], the excited modes will form replicas of the input field at a certain distance, where two output waveguides can be presented. If only one input port is excited, this optical power can be equally distributed to the two outputs. Since MMI structures have a better balance in power splitting ratio than the other components, they are used in most on-chip LDV systems reported in this thesis. However, reflections and cross talks in an MMI coupler are usually very strong, hence they may introduce large deviations in the LDV outputs. To solve this problem, several improvements have been designed to reduce these reflections and cross talks, which will be discussed in Chapter 3. Another solution is to replace the MMI couplers with directional couplers which have relatively small reflections and cross-talks, though their splitting ratios strongly depend on fabrication processes and hence cannot be well controlled. In addition, an unbalanced splitting ratio is sometimes required to obtain a better signal-to-noise ratio (SNR) in the output signals. For this purpose, directional couplers have to be used.

A light transmitting antenna (TA) and a light receiving antenna (RA) are needed in the measurement arm of the interferometer. The TA is the optical component used for sending light signals to the vibrating target, while the RA is a compo-

ment for collecting back-reflection from the target. In this system, both the TA and RA are realized with on-chip grating coupler (GC) structures, which have been thoroughly studied on the SOI platform [11–15]. Depending on different interferometer configurations, a TA and an RA can be the same GC or two adjacent GCs.

The mathematical description of the interferometer is given as follows. During the operation, the light signal is split by the optical splitter into two parts: the measurement signal (denoted with a subscript m) and the reference signal (denoted with a subscript r), with their amplitudes denoted as $\kappa_m E_0(t)$ and $\kappa_r E_0(t)$, respectively, where κ_m and κ_r are the optical splitting efficiencies into the measurement and reference arms, respectively. For an ideal optical splitter without power loss, $|\kappa_m|^2 + |\kappa_r|^2 = 1$ is fulfilled. The measurement signal will be sent out of the chip via the TA, and a portion of light is collected back into the measurement arm again by the RA. The recollected measurement signal carries the information of the Doppler shift, but also undergoes a strong power loss. Consider the process of the measurement signal as a black box. The effect of this black box to the measurement light can be considered as the combination of a power attenuation (remaining power = α_m) and a frequency modulation $f_D(t)$ (or a phase modulation $\theta_D(t) = 2\pi \int_0^t f_D(t) dt$).

There may be a loss in the reference arm as well, but the corresponding remaining power α_r is usually much larger than α_m . Before recombination, the electric fields of the measurement and reference signals of a homodyne LDV can be expressed as

$$E_m(t) = \alpha_m \kappa_m e^{i\theta_D(t)} E_0(t) \quad (2.3)$$

$$E_r(t) = \alpha_r \kappa_r E_0(t). \quad (2.4)$$

These two signals will be recombined in the optical combiner

$$E_o(t) = \frac{1}{\sqrt{2}} [E_m(t) + E_r(t)]. \quad (2.5)$$

In this case we assume that the optical combiner is an ideal 3 dB coupler. Due to the Doppler shift in the measurement signal, the intensity of this mixture signal is oscillating. This oscillation will be used for the Doppler shift recovery in later stages. For a heterodyne LDV, the reference signal has to be written as

$$E_r(t) = \alpha_r \kappa_r e^{i2\pi f_{ofst} t} E_0(t). \quad (2.6)$$

2.1.3 Imaging optical system

The black box in the measurement arm mentioned above includes three parts: an on-chip optical coupler including the TA and/or RA, a free-space imaging system,

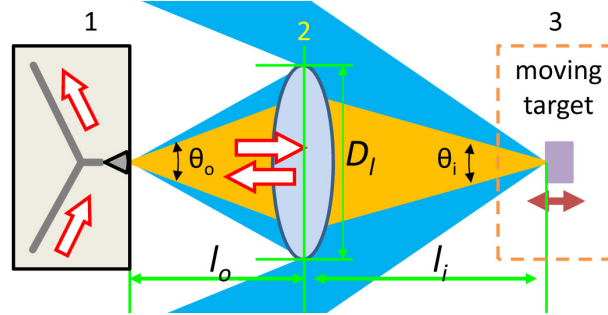


Figure 2.2: Three important parts of the imaging optical system: 1. on-chip optical coupler, 2. free-space imaging system, 3. a vibrating surface.

and a vibrating target. A simplified imaging system is shown in figure 2.2, where only one lens is used.

In order to avoid a strong attenuation in the measurement signal, a proper imaging system is required. The numerical aperture (NA) on the chip side is determined by the on-chip TA and/or RA. Here we assume that the TA and RA are realized with grating couplers (GCs). Therefore, the chip-side NA is determined by the effective size of the GC (s_{gc}), i.e. the size of the out-coupled optical mode from the GC. Assuming that $s_{gc} = 10 \times 10 \mu\text{m}^2$ and $\lambda_0 = 1.55 \mu\text{m}$, the NA will be around 0.1 and the divergence angle $\theta_o = 11.3^\circ$.

When the lens diameter $D_l > 2l_o \tan(\theta_o/2)$, the NA in the image side is determined by the magnification of the system $M = l_i/l_o$, where l_o and l_i are the object and image distances respectively (see figure 2.2). Though the light coupled back to the grating coupler seems to have a larger divergence angle, the portion that lies outside of the NA of the grating coupler will be filtered out by the GC and hence can not be coupled into the chip.

If the vibrating surface is a Lambertian reflector and the system magnification is much larger than 1, the power of the back-coupled light is inversely proportional to l_i^2 . Therefore if the image distance l_i is increased by 10 times, the power of the back-reflected light will be reduced to 1% of the original power.

To enhance the backreflection, a retroreflective tape is sometimes attached to the target to increase the optical power reflected to the LDV. The most commonly used retroreflective tapes consist of numerous glass microspheres glued on top of a reflective metal sheet.

2.1.4 Photo-detectors

For a homodyne LDV, the recombined signal will be sent to the photo-detectors and transformed into a time dependent photocurrent signals ($i(t)$), which can be

written as [3]

$$\begin{aligned} i(t) &= \frac{\eta}{2} |E_m(t) + E_r(t)|^2 \\ &= \frac{\eta A^2}{2} \{ \alpha_m^2 \kappa_m^2 + \alpha_r^2 \kappa_r^2 + 2\alpha_m \alpha_r \kappa_m \kappa_r \cos[\theta_D(t)] \}, \end{aligned} \quad (2.7)$$

where η is the detection efficiency of the PD. The photocurrent signal is usually separated into two parts, a *dc* term and an *ac* term.

$$\begin{aligned} i(t) &= i_{dc}(t) + i_{ac}(t) \\ i_{dc}(t) &= \frac{\eta A^2}{2} (\alpha_m^2 \kappa_m^2 + \alpha_r^2 \kappa_r^2) \\ i_{ac}(t) &= \rho \cos[\theta_D(t)], \end{aligned} \quad (2.8)$$

where $\rho = \eta A^2 \alpha_m \alpha_r \kappa_m \kappa_r$ is the amplitude of the vector.

In the heterodyne case, the *ac* term would become

$$i_{ac}(t) = \rho \cos[2\pi f_{ofs} t - \theta_D(t)], \quad (2.9)$$

where f_{ofs} is the optical frequency shift of the reference signal.

2.1.5 90° optical hybrid

A 90° optical hybrid is a special optical combiner with two optical inputs and four outputs. Assuming that the transfer function of an ideal 90° optical hybrid is denoted as \mathbf{T}_h , the four outputs of the hybrid should be written as

$$\begin{pmatrix} E_1(t) \\ E_2(t) \\ E_3(t) \\ E_4(t) \end{pmatrix} = \mathbf{T}_h \begin{pmatrix} E_r(t) \\ E_m(t) \end{pmatrix}, \quad (2.10)$$

where

$$\mathbf{T}_h = \frac{1}{2} \begin{pmatrix} 1 & 1 \\ 1 & -1 \\ 1 & i \\ 1 & -i \end{pmatrix} \quad (2.11)$$

The phase differences among these outputs are ignored in the transfer function, since they have no impact on the photocurrent signals.

The 90° optical hybrid has been realized on an SOI chip using MMI structures [9, 16], which is based on a 2×4 MMI design. Due to fabrication errors, however, on-chip 90° optical hybrids are usually not ideal. A general transfer function of the 90° optical hybrid is written as

$$\mathbf{T}_h = \begin{pmatrix} \kappa_{1,1} & \kappa_{1,2} e^{i\phi_{1,2}} \\ \kappa_{2,1} & \kappa_{2,2} e^{i\phi_{2,2}} \\ \kappa_{3,1} & \kappa_{3,2} e^{i\phi_{3,2}} \\ \kappa_{4,1} & \kappa_{4,2} e^{i\phi_{4,2}} \end{pmatrix}. \quad (2.12)$$

The impact of wavelength and temperature variations on this 90° optical hybrid have been assessed by simulation with the commercial FimmWave mode solver. From the simulation result, it can be found that the $\kappa_{j,k}$ and $\phi_{j,2}$ of the 90° optical hybrid change slowly with wavelength. When the wavelength increases from 1545 nm to 1555 nm, the maximal changes of $\kappa_{j,k}$ and $\phi_{j,2}$ are small values of 4% and 4°, respectively. The influence of the temperature is also very weak. For a temperature change of 20°C in simulation, the maximal change of $\kappa_{j,k}$ is 0.3%, and the maximal phase deviation $\phi_{j,2}$ is 0.3°. These results indicate that the hybrid itself is insensitive to wavelength and temperature variations.

2.1.6 Optical frequency shifter

As is already mentioned, an optical frequency shifter (OFS) works as a local oscillator (LO) in the heterodyne LDV to solve noise problems. Acousto-optic modulators are conventionally used as the OFSs in LDVs. However, the difficulty in generating an acoustic wave in silicon (due to the lack of piezoelectricity) hinders the integration of an acousto-optic modulator on the SOI chip. In order to generate acoustic waves, one may need to attach another material with strong piezo-electric effect, i.e. ZnO, to the silicon substrate. Although this integration has been demonstrated on a blank SOI substrate, the efficiency in the acoustic-wave generation is still very weak. Besides, it is still difficult to fabricate a high quality piezo-electric material layer on a patterned SOI substrate.

There are also other alternatives that can be used to realize an OFS on the SOI substrate, including the serrodyne frequency shift technique which will be discussed in detail in Chapter 4. Most of these approaches may introduce several high-order harmonics in the reference signal, and hence bring some extra problems to the LDV outputs. Considering an imperfect OFS, the frequency shifted signal can be described as

$$E_{ofs}(t) = E_r(t) \sum_k \mu_k e^{i2\pi k f_{ofs} t}, \quad (2.13)$$

where k is the order of the harmonic. Under an ideal situation, the OFS should have only the harmonic order with $k = 1$ (fundamental harmonic), and the rest should be strongly suppressed.

2.1.7 Demodulators

With the help of a photo-detector (PD), the beat in the light intensity can be converted to an electrical signal used for recovering the Doppler frequency shift. However, the frequency change of the photocurrent can not be directly read out from the photocurrent oscillations, and thus a demodulator is needed.

On one hand, the demodulation can be done with various electric circuits, e.g. FM demodulator based on phase-locked loop (PLL). On the other hand, the demodulation can also be realized numerically once the photocurrent signals are digitized and sent to a computer. For the sake of convenience, the numerical demodulation method is used.

Within this work, an analog-to-digital converter (ADC) is used to transform the photocurrent signal to a digitized form. According to the Nyquist-Shannon sampling theorem, the sampling frequency f_s of the ADC should be at least two times as large as the maximum useful frequency in the photocurrent. For homodyne LDV, the relation between the sampling rate f_s should follow Nyquist-Shannon sampling theorem,

$$f_s > 2\left(f_v + \frac{2v_m}{\lambda_0}\right), \quad (2.14)$$

where f_v and v_m are the frequency and the maximal velocity of the measured mechanical vibration, respectively. This means that the sampling frequency should be larger than 2.58 MHz when $v_m = 1$ m/s (not considering f_v). For heterodyne LDV, the relation $f_s > 2f_{ofs}$ should be realized.

The demodulation methods for homodyne and heterodyne LDVs are quite different from each other. To conquer some difficulties related with imperfect designs and noise, some special tricks have been designed and used in the demodulation. These methods will be discussed in detail in the following sections.

2.2 Demodulation method for typical homodyne LDVs

Since no frequency shift is needed in the reference signal of a homodyne detection, the corresponding demodulation method will also be different from the one for heterodyne. The actual differences between these two demodulation methods are significant. Therefore, it is necessary to discuss them separately.

In this section, we focus the discussion on DSP-based demodulation algorithms for on-chip homodyne LDVs. Moreover, the LDV outputs (demodulated signals) can be deformed when some deviation sources exist. This deformation will also be theoretically analyzed in this section

2.2.1 Different demodulation methods for homodyne LDVs

There are several demodulation algorithms for homodyne LDV. A short discussion about these methods is as follows.

To retrieve the Doppler phase shift for a weak vibration, one can directly use the photocurrent of the combined signal. Considering that the phase in the reference arm can be tuned with a phase modulator, the photocurrent is

$$i(t) = i_{dc} + \rho \cos[\theta_D(t) - \theta_{ref}], \quad (2.15)$$

where θ_{ref} is an extra phase shift applied to the reference signal. Assuming that θ_{ref} is kept at 90° (in quadrature) and $\theta_D(t) \ll \pi$, the photocurrent $i(t)$ can be simplified to

$$i(t) = i_{dc} + \rho\theta_D(t). \quad (2.16)$$

Therefore the measured photocurrent and $\theta_D(t)$ can be a simple linear relation. However, this method needs a well-controlled phase in the reference arm. If the environmentally-induced phase deviations in the reference arm are significant, a feedback system is needed to keep the interferometer working in quadrature ($\theta_{ref} = 90^\circ$). Its measuring range of displacement is also very small. The required maximum measurable displacement of our device is much larger than the light wavelength, so this method is not suitable for us.

Another method is called the $J_1 \dots J_4$ method [17, 18]. It has a large measurable displacement range and require no feedback phase bias in the reference signal. In this method, the amplitude of a sinusoidal vibration can be calculated by analyzing the power distributions of several harmonic orders in the frequency spectra. However, this method works only for sinusoidal mechanical vibrations.

A fringe counting method is also usually used. In this method, the phase (or frequency) variation of the measurement signal is estimated by counting number of fringes in the photocurrent signal as a function of time. However, this method has a low distance resolution ($< \lambda_0/2$), and can thus only be used for large vibration measurement.

In order to have a broad measurable displacement range, an in-phase & quadrature (IQ) demodulation method is used. As is mentioned above, this method usually requires a 90° optical hybrid and two pairs of photo-detectors. Compared to the aforementioned methods, the IQ demodulation method is more powerful since it has a larger measuring range. A sub-nanometer displacement resolution has been reported with this method as well [19].

2.2.2 IQ demodulation for ideal optical components

According to previous discussions, the four photocurrent of signals $i_j(t)$ from an ideal 90° optical hybrid are expressed as

$$i_1(t) = i_{dc} + \frac{\rho}{2} \cos[\theta_D(t)] \quad (2.17)$$

$$i_2(t) = i_{dc} - \frac{\rho}{2} \cos[\theta_D(t)] \quad (2.18)$$

$$i_3(t) = i_{dc} + \frac{\rho}{2} \sin[\theta_D(t)] \quad (2.19)$$

$$i_4(t) = i_{dc} - \frac{\rho}{2} \sin[\theta_D(t)], \quad (2.20)$$

$$(2.21)$$

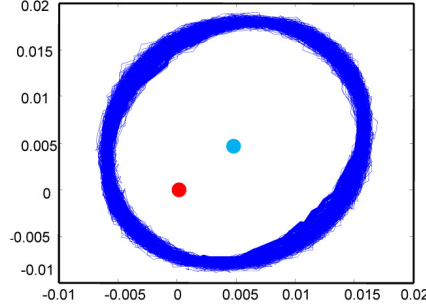


Figure 2.3: A typical IQ Lissajous curve for the homodyne outputs.

where $i_{dc} = \eta A^2 (\alpha_m^2 \kappa_m^2 + \alpha_r^2 \kappa_r^2) / 4$ and $\rho = \eta A^2 \alpha_m \alpha_r \kappa_m \kappa_r$. The two required signal $I(t)$ and $Q(t)$ can be derived from the differential signals between $i_1(t)$ and $i_2(t)$, and between $i_3(t)$ and $i_4(t)$, i.e.

$$\begin{aligned} I(t) &\equiv i_1(t) - i_2(t) = \rho \cos[\theta_D(t)] \\ Q(t) &\equiv i_3(t) - i_4(t) = \rho \sin[\theta_D(t)]. \end{aligned}$$

The Doppler phase shift $\theta_D(t)$ can thus be obtained using a so-called ‘‘arc-tangent’’ method,

$$\theta_D(t) = \arctan \left[\frac{Q(t)}{I(t)} \right]. \quad (2.22)$$

It can be found that the variations in i_{dc} and ρ can be canceled out after implementing this method.

The Lissajous curve formed by $I(t)$ and $Q(t)$ is found to be a circle in this ideal situation, and the circle center is at the origin of the coordinate system. Therefore, the Doppler phase shift $\theta_D(t)$ equals the angle of the corresponding point in the Lissajous curve.

2.2.3 IQ demodulation for real devices

In practice, however, the photocurrent signals are not as expected, and the corresponding IQ Lissajous curves are usually changed to ellipses with the center also shifted away from the origin (see figure 2.3).

As is mentioned in a previous section, the transfer matrix of the 90° hybrid can be changed due to device deviations that occurred in fabrication. Thus it is normally expressed in the general form of Eq. 2.12. Apart from the fabrication errors in the hybrid, several other problems may also contribute to changes in the photocurrent:

- Due to misalignment, the detection efficiencies η_j may be different from one another.
- Some significant on-chip spurious reflections can be mixed with the useful signal and therefore change the corresponding photocurrents. These spurious reflections may be introduced both in the reference and the measurement arms.
- As the target surface is vibrating, the focus point of the reflected measurement light can also change, which leads to an amplitude variation $\alpha_m(t)$ in the measurement light due to the changing coupling efficiency. The amplitude change is sometimes significant when the surface vibration is not parallel to the light direction.

Considering these deviations, the LDV photocurrents can be divided into three parts

$$i_j(t) = C_j(t) + S_j(t) + R_j(t), \quad (2.23)$$

where $C_j(t)$ is the total power of the reference and measurement signals, $S_j(t)$ is an amplitude modulation induced by the phase variation of the measurement light, and $R_j(t)$ is the amplitude modulations caused by the spurious reflections.

Assume that the reference and the measurement signals have the same amplitude before the optical hybrid, i.e.

$$B(t) = \kappa_m E_0(t) = \kappa_r E_0(t). \quad (2.24)$$

Considering Eq. 2.12, the first two terms in Eq. 2.23 can be expressed as

$$\begin{aligned} C_j(t) &= \zeta_j(t) [\kappa_{j,1}^2 \alpha_r^2 + \kappa_{j,2}^2 \alpha_m^2(t)] \\ S_j(t) &= 2\zeta_j(t) \kappa_{j,1} \kappa_{j,2} \alpha_m(t) \alpha_r \cos[\phi_{j,2} + \theta_D(t)], \end{aligned} \quad (2.25)$$

where $\zeta_j(t) = \eta_j B^2(t)$. It can be seen that the amplitudes of both $C_j(t)$ and $S_j(t)$ may be different among the four outputs and vary with time due to the power variation in the laser source and in the back-coupled measurement signal, which leads to an elliptical IQ Lissajous curve.

The third term in Eq. 2.23 is caused by spurious reflections. Since the optical path lengths of the spurious reflections are different from those of the reference and measurement signals, a temperature change of the chip will introduce different phase shifts among these signals, which may cause strong amplitude and phase modulations in the interferometer outputs. The impact of these spurious reflections can be estimated as follows. For simplicity, we only consider two spurious reflections: one is introduced in the reference arm and the other is from the measurement arm. These two spurious reflections can be denoted as

$$E_{s,r}(t) = s_r B(t) \exp(i\beta_r) \quad (2.26)$$

$$E_{s,m}(t) = s_m B(t) \exp(i\beta_m), \quad (2.27)$$

where $\beta_r = 2\pi n_{eff} L_{s,r}/\lambda_0$ and $\beta_m = 2\pi n_{eff} L_{m,r}/\lambda_0$ are the extra phase changes of the reference and measurement signals due to spurious reflections, respectively, $L_{s,r}$ and $L_{s,m}$ are the corresponding increases in the optical path for the two spurious reflections, and n_{eff} is the effective index of the guided optical mode in the waveguide.

Considering these two spurious reflections, $R_j(t)$ can be divided into four parts

$$\begin{aligned} R_j(t) = & C_{j,m}(t) + S_{j,m}(t) \\ & + C_{j,r}(t) + S_{j,r}(t), \end{aligned} \quad (2.28)$$

where

$$\begin{aligned} C_{j,m}(t) &= 2\zeta_j(t)\kappa_{j,1}\kappa_{j,2}\alpha_r s_m \cos(\phi_{j,2} + \beta_m) \\ S_{j,m}(t) &= 2\zeta_j(t)\kappa_{j,2}^2\alpha_m(t)s_m \cos[\theta_D(t) - \beta_m] \\ C_{j,r}(t) &= 2\zeta_j(t)\kappa_{j,1}^2\alpha_r s_r \cos(\beta_r) \\ S_{j,r}(t) &= 2\zeta_j(t)\kappa_{j,1}\kappa_{j,2}\alpha_m(t)s_r \cos[\phi_{j,2} + \theta_D(t) - \beta_r]. \end{aligned} \quad (2.29)$$

It can be seen that the terms β_m and β_r are involved in these expressions. Since the values of β_m and β_r are sensitive to the variations of temperature and of wavelength, the LDV outputs will be influenced as well.

2.2.4 Compensation method

Sometimes it is hard to avoid these spurious reflections, thus compensation methods are needed. It is found that both $I(t)$ and $Q(t)$ can be simplified to the form $A + B \cos[\theta_D(t) + C]$ even when strong spurious reflections are mixed with the useful signals. Since these two signals share the same frequency with respect to the variable $\theta_D(t)$, the Lissajous curve generated from these signals turns out to be an ellipse. Consequently, $I(t)$ and $Q(t)$ can be expressed as

$$\begin{aligned} I(t) &= I_0 + a \cos[\theta_D(t) + \varphi_1] \cos(\varphi_0) - b \sin[\theta_D(t) + \varphi_1] \sin(\varphi_0) \\ Q(t) &= Q_0 + a \cos[\theta_D(t) + \varphi_1] \sin(\varphi_0) + b \sin[\theta_D(t) + \varphi_1] \cos(\varphi_0), \end{aligned}$$

where (I_0, Q_0) is the center position of the ellipse, φ_0 is the inclination angle, φ_1 is a constant phase shift, a and b are the semi-major and semi-minor axes of the ellipse, respectively.

When the amplitude of the measured vibration is larger than $\lambda_0/2$, the Lissajous curve is a complete ellipse. A compensation approach can proceed as follows:

1. The parameters $(I_0, Q_0, a, b, \text{ and } \varphi_0)$ of the measured IQ trace are obtained with a numerical method.

2. The center of the IQ ellipse is shifted to the origin according to the following algorithm

$$\begin{aligned} I_1(t) &= I(t) - I_0 \\ Q_1(t) &= Q(t) - Q_0. \end{aligned} \quad (2.30)$$

3. The ellipse is then transformed to a circle by using the following formula

$$I'(t) = b[I_1(t) \cos(\varphi_0) + Q_1(t) \sin(\varphi_0)] \quad (2.31)$$

$$Q'(t) = a[-I_1(t) \sin(\varphi_0) + Q_1(t) \cos(\varphi_0)]. \quad (2.32)$$

The eventually achieved trace of $(I'(t), Q'(t))$ is a circle with a radius of $a \cdot b$. The aforementioned arc-tangent approach can then be used to calculate the Doppler phase shift. The retrieved phase in this case is the sum of the desired Doppler phase shift $\theta_D(t)$ and a constant phase shift φ_1 . Since this φ_1 is a constant value and is not important for the outputs, it can be omitted.

However, fluctuations in the light amplitude are hardly avoidable, resulting in variations of the compensation parameters (I_0 , Q_0 , a , b and φ_0). To solve this problem, one can use an active compensation approach, in which the five compensation parameters are measured and updated at regular intervals. With this approach, the changes of these compensation parameters can be tracked. However, when the vibrating amplitude is less than $\lambda_0/2$, the IQ trace will become an incomplete ellipse, thus the five compensation parameters will be unachievable. An improved active compensation approach can be used in this case, in which an assumption is made that the only deviation source is the change of $E_0(t)$. A calibration measurement on a large vibration should be done in the beginning to obtain the initial five parameters. After the initializing calibration, the target vibration with a small amplitude is measured and the average values of $I(t)$ and $Q(t)$ are tracked. The measured variations of these average values can be used to calculate the changes of the other compensation parameters. This method should be done when the temperature of the chip and the wavelength of the laser source is stabilized. The active compensation approach also requires more calculating time, and hence it may not be suitable for measuring vibrations with higher frequencies.

2.2.5 Noise issues

The fundamental limiting factor of the homodyne LDV outputs is the noise. Noise also reduces the compensation quality since it increases the errors in the compensation algorithm, especially the “center-finding” algorithm. In this short section we will provide the value of phase deviation due to the existence of noise.

In homodyne, there are several noise sources: the relative intensity noise (RIN) of the laser source, the low frequency noise in the subsequent electronics of the

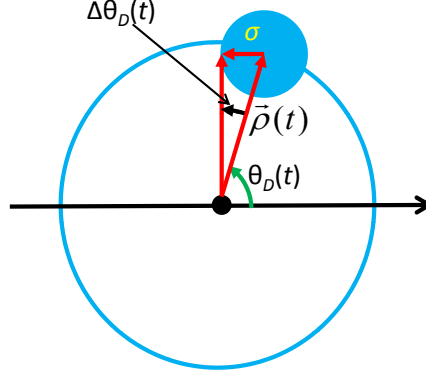


Figure 2.4: IQ curve for homodyne output signals with noise.

PDs, and shot noise. In the DSP method, the ADC discretization noise should also be considered. Here we consider the total root-mean-square fluctuations σ in the photocurrent as a measure for all these types of noise.

Due to the existence of noise, the derived phase shift could be changed, which can be understood with the help of the diagram in figure 2.4. It can be found that the maximal phase deviation $\Delta\theta_{D,m}$ can be calculated from

$$\Delta\theta_{D,m} = \arcsin\left(\frac{\sigma}{\rho}\right). \quad (2.33)$$

It can be seen that the signal-no-noise ratio ($20 \log(\rho/\sigma)$) is directly related to the maximal phase deviation. Once $\sigma \geq \rho$, the phase shift won't be resolved anymore. To ensure that the maximum phase deviation is lower than 0.01π (corresponding to a displacement of 3.9 nm), the SNR should be greater than 30 dB.

2.3 Demodulation method for heterodyne LDVs

In a heterodyne LDV, an OFS is used to ensure that the carrier frequency of the photocurrent signal is not zero, so as to avoid the influence of low frequency noise, such as low frequency noise in photo-detectors and subsequent electronics. A typical noise spectrum of a photo-detector is shown in figure 2.5, which shows that a strong noise exists at the frequency region lower than 20 MHz. The very strong noise occurring at the frequency region lower than 1 kHz shown in figure 2.5 originates from the measurement setup. This PD noise can also be found in our measurement setup. Therefore, it is necessary to have a frequency shift larger than several kilohertz. A frequency shift larger than 20 MHz is usually used in LDV systems to ensure a better measurement resolution. Note that the region of the low frequency noise depends on the specific PD design. Since a frequency shift

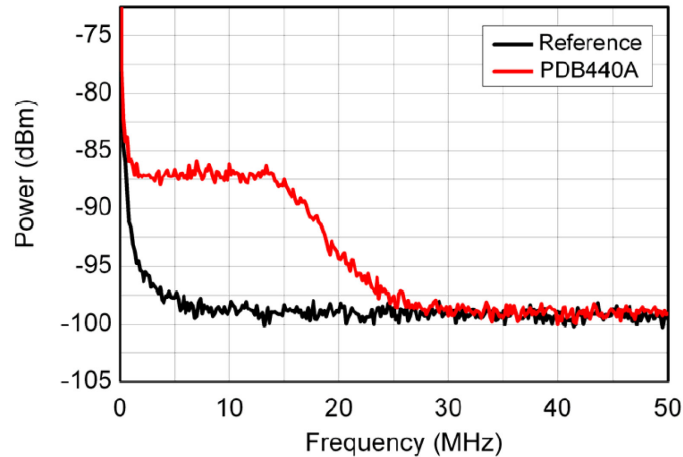


Figure 2.5: The typical noise spectrum for photo-detectors (Thorlabs PDB 440A). The red curve is measured when the inputs of the PD are blocked, while the black curve is for the case that the PD is switched off, which represents the system's noise floor. Reproduced from [20].

is required, the demodulation method for a heterodyne LDV is different from that for homodyne.

In the first part of this section, several conventional heterodyne demodulation methods are discussed, including the classic heterodyne method, synthetic heterodyne method and the demodulation algorithm used in this thesis. The influence of spurious reflections and imperfect optical frequency shift are theoretically analyzed afterwards.

2.3.1 Conventional demodulation method for heterodyne LDV

The demodulation for heterodyne LDV photocurrents can be realized with a conventional FM detector, which can be implemented in different ways. It can be a fringe counting technique, a Foster-Seeley discriminator, a radio detector, or a phase-locked loop (PLL) circuit [21].

In DSP, a digital quadrature demodulation is often used since it is easy to implement. In this method, two numerically generated local oscillators at a frequency f_{ofs} are mixed with two copies of the photocurrent. This procedure shifts the carrier of the useful signal to DC level. An “arc-tangent” algorithm is then used for the recovery of the Doppler shift. This looks similar to the IQ demodulation in homodyne, since both methods utilize the “arc-tangent” method. However, with the quadrature demodulation for heterodyne the low frequency noise can be filtered out before demodulation, which is difficult in homodyne. We will focus on this

quadrature demodulation method in this section.

2.3.2 Ideal digital quadrature demodulation

Firstly, the demodulation method for an ideal output signal is introduced. According to Eq. 2.9, we can obtain a photocurrent signal

$$\begin{aligned} I(t) &= \frac{\eta}{2} |E_m(t) + E_{ofs}(t)|^2 \\ &= \frac{\eta A^2}{2} \{ \alpha_m^2 \kappa_m^2 + \alpha_r^2 \kappa_r^2 \\ &\quad + 2\alpha_m \alpha_r \kappa_m \kappa_r \cos[2\pi f_{ofs} t - \theta_D(t)] \}. \end{aligned} \quad (2.34)$$

This signal is converted to digital signals using an analog-to-digital converter (ADC). According to Nyquist-Shannon sampling theorem, the sampling frequency of the ADC should be at least twice as large as the carrier frequency f_{ofs} .

In the demodulation process of a typical digital quadrature demodulation, two local oscillating (LO) signals with the same frequency f_{ofs} are digitally generated, expressed as $LO_i(t) = \cos(2\pi f_{ofs} t)$ and $LO_q(t) = \sin(2\pi f_{ofs} t)$, respectively. These two local oscillators are multiplied with the photocurrent signal $I(t)$, obtaining two mixture signals

$$\begin{aligned} S_i(t) &= I(t) \cdot LO_i(t) \\ &= \frac{\eta A^2}{2} \{ \alpha_m \alpha_r \kappa_m \kappa_r \cos[\theta_D(t)] + [\alpha_m^2 \kappa_m^2 + \alpha_r^2 \kappa_r^2] \cos(2\pi f_{ofs} t) \\ &\quad + \alpha_m \alpha_r \kappa_m \kappa_r \cos[4\pi f_{ofs} t - \theta_D(t)] \}. \end{aligned} \quad (2.35)$$

$$\begin{aligned} S_q(t) &= I(t) \cdot LO_q(t) \\ &= \frac{\eta A^2}{2} \{ \alpha_m \alpha_r \kappa_m \kappa_r \sin[\theta_D(t)] + [\alpha_m^2 \kappa_m^2 + \alpha_r^2 \kappa_r^2] \sin(2\pi f_{ofs} t) \\ &\quad + \alpha_m \alpha_r \kappa_m \kappa_r \sin[4\pi f_{ofs} t - \theta_D(t)] \}. \end{aligned} \quad (2.36)$$

It can be found that the useful term (the first terms in Eq. 2.35 and Eq. 2.36) is shifted to DC region, while the original DC signal including low frequency noise is moved to a carrier frequency of f_{ofs} . Low pass filters can then be used to remove the noise at high frequencies. The cutoff frequency of the filter f_{cutoff} should be lower than $f_{ofs}/2$. The bandwidth of the useful signal should be lower than f_{cutoff} . Therefore, for a sinusoidal vibration with a frequency of f_v and a maximal velocity of v_m , the following relation should be fulfilled in the demodulation:

$$\left(f_v + \frac{2v_m}{\lambda_0} \right) < f_{cutoff} < f_{ofs}/2 \quad (2.37)$$

After the filtering, two output signals denoted as $I(t)$ and $Q(t)$ are obtained.

They can be expressed as

$$I(t) = \frac{\rho}{2} \cos[\theta_D(t)] \quad (2.38)$$

$$Q(t) = \frac{\rho}{2} \sin[\theta_D(t)], \quad (2.39)$$

where $\rho = \eta A^2 \alpha_m \alpha_r \kappa_m \kappa_r$. These IQ signals should form a circular Lissajous curve under ideal conditions. The Doppler shift $\theta_D(t)$ can be derived with an ‘‘arc-tangent’’ function, which is similar to what has been used in homodyne demodulation.

However, in practice, this curve is influenced by the spurious reflections and imperfect optical frequency signals. Moreover, the amplitude modulation in the back reflected measurement signal can also be problematic. The impacts of these deviations will be discussed one by one in following sections. Meanwhile, some compensation methods will also be introduced.

2.3.3 Influence of spurious reflections and compensation methods

Spurious reflections from a heterodyne LDV system and external reflectors have important impacts on the performance of the demodulation. They can be introduced in many integrated optical components, as is mentioned in the previous chapter. External reflectors, like dust in the air, can also contribute to the spurious reflection. These spurious reflections are mixed with the useful signal in the LDV, resulting in an extra phase shift. Designs should be done to suppress these spurious reflections to ensure a good performance of the LDV demodulation. More details about the reflectionless PIC designs will be discussed in the next chapter. In this chapter, we will analyze the actual influence of the spurious reflection.

If the spurious reflection is stationary, the photocurrent in the detector will be a mixture of three signals: the measurement signal, the reference signal, and the spurious reflection. The measurement and the reference signals will be expressed as

$$\begin{aligned} E_m &= \alpha_m B(t) e^{i[2\pi f_0 + \theta_D(t)]} \\ E_r &= \alpha_r B(t) e^{i2\pi(f_0 + f_{ofs})t}. \end{aligned}$$

The spurious reflection is

$$E_{sp} = \alpha_{sp} B(t) e^{i(2\pi f_0 t + \theta_{sp})}. \quad (2.40)$$

As a results, the signal is expressed as

$$\begin{aligned}
i(t) &= \frac{\eta}{2} |E_m + E_r + E_{sp}|^2 \\
&= \frac{\eta B^2(t)}{2} \left| \alpha_m e^{i\theta_D(t)} + \alpha_r e^{i2\pi f_{ofst}} + \alpha_{sp} e^{i\theta_{sp}} \right|^2 \\
&\propto \alpha_m^2 + \alpha_r^2 + \alpha_{sp}^2 + 2\alpha_m \alpha_{sp} \cos[\theta_{sp} - \theta_D(t)] \\
&\quad + 2\alpha_r \alpha_m \cos[2\pi f_{ofst} - \theta_D(t)] + 2\alpha_{sp} \alpha_r \cos[2\pi f_{ofst} - \theta_{sp}].
\end{aligned}$$

In the demodulation, this signal is multiplied with two local oscillators $\cos(2\pi f_{ofst})$ and $\sin(2\pi f_{ofst})$. After being filtered with a low pass filter, two mixture signals are obtained

$$I(t) = I_{dc} + I_{ac}(t) \quad (2.41)$$

$$Q(t) = Q_{dc} + Q_{ac}(t), \quad (2.42)$$

where

$$I_{dc} = \varrho \rho \cos(\theta_{sp}) \quad (2.43)$$

$$Q_{dc} = \varrho \rho \sin(\theta_{sp}) \quad (2.44)$$

$$I_{ac}(t) = \rho \cos[\theta_D(t)] \quad (2.45)$$

$$Q_{ac}(t) = \rho \sin[\theta_D(t)], \quad (2.46)$$

$\rho = \eta B^2(t) \alpha_m \alpha_r$, and $\varrho = \alpha_{sp} / \alpha_m$ is a spurious-reflection to measurement-signal ratio. Therefore the center of the IQ Lissajous circle is moved away from the origin to the position $[\varrho \rho \cos(\theta_{sp}), \varrho \rho \sin(\theta_{sp})]$, while the radius of the Lissajous circle remains ρ . If this shift is not noticed during demodulation, a wrong phase $\theta'_D(t)$ can be calculated using the ‘‘arc-tangent’’ method

$$\theta'_D(t) = \arctan \left[\frac{\sin \theta_D(t)}{\cos \theta_D(t) + \varrho^{-1}} \right] + \theta_D(t). \quad (2.47)$$

According to this equation, the difference between the deviated and the original phase has a maximum value $\arcsin(\varrho)$. To ensure that this maximum phase deviation is lower than 0.01π (corresponding to a displacement of 3.9 nm), the spurious reflection should be at least 30 dB lower than the useful measurement signal.

To compensate for this center shift, the ‘‘center-finding’’ algorithm is used to find the circle center out of the $I(t)$ and $Q(t)$ data. The value of $I_{ac}(t)$ and $Q_{ac}(t)$ can then be obtained with the information of the circle center. The real Doppler shift will be recovered using $\theta_D(t) = \arctan[Q_{ac}(t)/I_{ac}(t)]$.

A simulation with $\varrho = 30\%$ is done to show the influence of this spurious reflection (see figure 2.6). If the center shift is not compensated, a deviation can be found in the demodulated result (see figure 2.6(b)). The LDV output accuracy δ_{ldv} ,

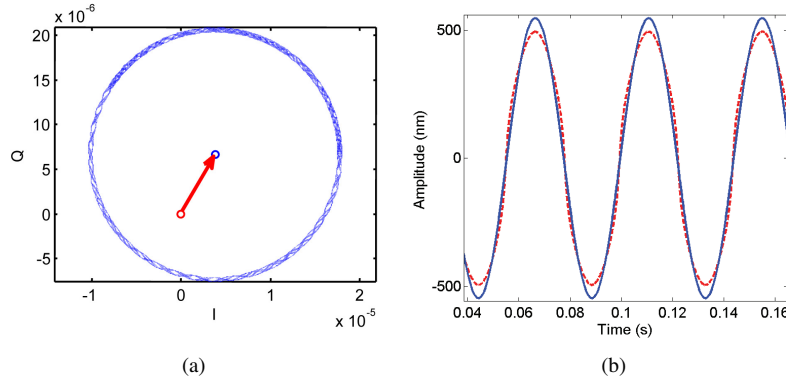


Figure 2.6: The influence of the spurious reflection on the demodulated results. In this case the power ratio between the spurious reflection and the useful reflection is around 30%. The vibrating frequency is 22.6 Hz. (a) the IQ Lissajous curve for signals with spurious reflection; (b) the solid curve represents for the original displacement signal and the dashed line is for the demodulated displacement.

or the root-mean-square (RMS) deviations between the original displacement and the demodulated results are plotted as a function of the relative power in the spurious reflection (see figure 2.7). The RMS deviation for the case with compensation is also shown in this figure (the dashed line), and it is found that the compensation is quite successful by limiting the deviation under 5 nm.

The compensation can be used for stationary spurious reflections while noise is not strong. Spurious reflections from the on-chip device may vary due to the temperature fluctuations. Luckily, in our integrated LDVs these fluctuations are not very strong due to the short interferometry arms. It is found that the Lissajous circle center (I_{dc} , Q_{dc}) in the same device is quite stable among different measurements. This indicates that the “center-finding” algorithm can be only required in the calibration measurement, while the measurements at later stages only need to use the stored value (I_{dc} , Q_{dc}) for compensation. If the center varies strongly with time, we will have to repeat the compensation frequently during the measurement.

2.3.4 Influence of residue harmonics in the frequency shift

As already mentioned, the reference signal with an imperfect frequency shift can be expressed as

$$E_{ofs}(t) = E_r(t) \sum_k \mu_k e^{i2\pi k f_{ofs} t}, \quad (2.48)$$

where k is the order of different harmonics. An imperfect OFS may excite high order harmonics, which can influence the LDV outputs. In this section we will just

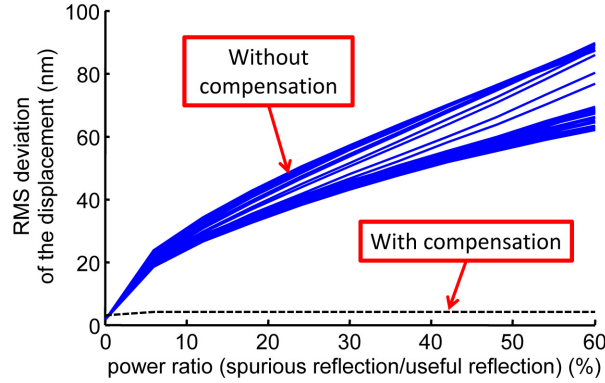


Figure 2.7: Simulated root-mean-square (RMS) deviations of the demodulated displacements versus spurious reflections with different power and phase values, for power ratios (spurious reflection/useful reflection) between 0% and 60%. The 36 solid curves represent for 36 evenly spaced phases of the spurious reflection from 0 to 2π . The dashed line is the RMS deviation when the spurious reflection compensation is applied.

discuss the influence of these residual harmonics regardless the actual causes of these deviations. More detailed discussions on the optical frequency shifter will be made in Chapter 4.

According to the quadrature demodulation method mentioned above, three residue harmonics with $k = -1, 0, 1$ are not removed after filtering. The -1st order lies in the same position as the fundamental harmonic and thus can be considered as a part of the optical frequency shift. Due to the existence of -1st order harmonic, the frequency shift is not a constant value anymore. The 0th order harmonic is very close to the measurement light in the frequency domain, and thus its influence to the demodulation result is similar to that of a spurious reflection. Therefore the compensation method for the 0th order harmonic is the same as that for spurious reflections, and thus it won't be elaborated in this chapter anymore.

In the heterodyne detection, the reflected measurement signal $E_m(t)$ will be mixed with the frequency shifted signal $E_{ofs}(t)$ in an optical combiner. Only considering the residue harmonics for $k = -1, 0, 1$, the obtained photocurrent

signals can be expressed as

$$\begin{aligned}
i(t) &= \frac{\eta}{2} |E_{ofs}(t) + E_m(t)|^2 & (2.49) \\
&\propto \left| \mu_{-1} e^{-i2\pi f_{ofs} t} + \mu_0 + \mu_1 e^{i2\pi f_{ofs} t} + e^{i\theta_D(t)} \right|^2 \\
&= |\mu_{-1}|^2 + |\mu_0|^2 + |\mu_1|^2 + 1 \\
&\quad + 2|\mu_0| \cos[\theta_D(t) - \theta_0] \\
&\quad + 2|\mu_1| |\mu_{-1}| \cos[4\pi f_{ofs} t + \theta_1 - \theta_{-1}] \\
&\quad + 2|\mu_0| |\mu_{-1}| \cos[2\pi f_{ofs} t - \theta_{-1} + \theta_0] \\
&\quad + 2|\mu_0| |\mu_1| \cos[2\pi f_{ofs} t + \theta_1 - \theta_0] \\
&\quad + 2|\mu_{-1}| \cos[2\pi f_{ofs} t - \theta_{-1} + \theta_D(t)] \\
&\quad + 2|\mu_1| \cos[2\pi f_{ofs} t + \theta_1 - \theta_D(t)]
\end{aligned}$$

where $\mu_k = |\mu_k| e^{i\theta_k}$. Here an assumption is made that $\alpha_m \kappa_m E_0(t) = \alpha_r \kappa_r E_0(t)$. With a quadrature demodulator, the photocurrent is multiplied with two local oscillators $\cos(2\pi f_{ofs} t)$ and $\sin(2\pi f_{ofs} t)$. After filtering we have

$$I_{dc} = \varrho_r \rho |\mu_0| [|\mu_{-1}| \cos(\theta_{-1} - \theta_0) + |\mu_1| \cos(\theta_0 - \theta_1)] \quad (2.50)$$

$$Q_{dc} = \varrho_r \rho |\mu_0| [|\mu_{-1}| \sin(\theta_{-1} - \theta_0) + |\mu_1| \sin(\theta_0 - \theta_1)] \quad (2.51)$$

$$I_{ac}(t) = \rho \{ |\mu_{-1}| \cos[\theta_{-1} - \theta_D(t)] + |\mu_1| \cos[\theta_D(t) - \theta_1] \} \quad (2.52)$$

$$Q_{ac}(t) = \rho \{ |\mu_{-1}| \sin[\theta_{-1} - \theta_D(t)] + |\mu_1| \sin[\theta_D(t) - \theta_1] \}, \quad (2.53)$$

where $\rho = \alpha_m \alpha_r \kappa_m \kappa_r A^2$, and $\varrho_r = \alpha_r / \alpha_m$. The radius of the curve from the center (I_{dc}, Q_{dc}) changes with time t and can be calculated as

$$\begin{aligned}
\Upsilon(t) &= \sqrt{I_{ac}^2(t) + Q_{ac}^2(t)} & (2.54) \\
&= \rho \sqrt{|\mu_{-1}|^2 + |\mu_1|^2 + 2|\mu_{-1}| |\mu_1| \cos[2\theta_D(t) - \theta_1 - \theta_{-1}]}
\end{aligned}$$

From this equation, we find that the IQ curve forms an ellipse with the eccentricity expressed as

$$e = \frac{2\sqrt{|\mu_1| |\mu_{-1}|}}{|\mu_1| + |\mu_{-1}|}. \quad (2.55)$$

The measured Doppler phase shift $\theta'_D(t)$ is deviated from the real value $\theta_D(t)$, and it can be calculated as

$$\theta'_D(t) = \theta_D(t) - \theta_1 - \arctan \left\{ \frac{\mu_{-1} \sin[2\theta_D(t) - \theta_1 - \theta_{-1}]}{\mu_1 + \mu_{-1} \cos[2\theta_D(t) - \theta_1 - \theta_{-1}]} \right\}. \quad (2.56)$$

From this equation, the maximum phase deviation is derived as $\arcsin(\mu_{-1}/\mu_1)$. To ensure a maximal phase deviation lower than 0.01π (corresponding to 3.9 nm), the -1st order harmonic should be 30 dB lower than the fundamental harmonic.

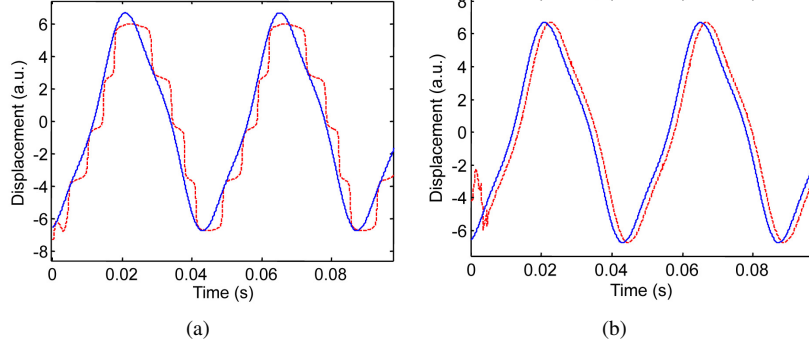


Figure 2.8: Photocurrent signals with strong -1st order harmonics generated by using an imperfect sawtooth driving signal. The solid curves show the original displacement value and break curves are the demodulated results. In 2.8(a), no phase compensation was done. In 2.8(b), the phase is compensated using equation 2.57.

In practice, we can obtain the information of $\theta'_D(t)$ and $\Upsilon(t)$ from the measured data. The original Doppler shift value $\theta_D(t)$ can be derived from these two values with the following equation

$$\theta_D(t) = \theta'_D(t) + \text{sign} \cdot \arccos \left[\frac{|\mu_{-1}|^2 - |\mu_1|^2 - \Upsilon^2(t)}{2\Upsilon(t)|\mu_1|} \right], \quad (2.57)$$

where sign is positive for $\theta'_D(t) - (\theta_1 + \theta_{-1})/2 \in (0, \pi/2) \cup (\pi, 3\pi/2)$ and negative for the rest. Figure 2.8 shows a comparison between the demodulations without and with the phase compensation. It is seen that the compensation works quite well. It is also found that the phase deviation in this case looks similar to the one introduced by spurious reflection. The biggest difference is the frequency of the phase deviation, i.e. for the -1st harmonic the frequency of the signal deviation doubles that of the spurious reflection.

2.3.5 Influence of coupling variations in the reflected measurement light

Due to the displacement of the vibrating surface, the coupling efficiency of the reflected measurement signal may also change. This coupling efficiency change in the reflected signal causes a shape deviation in the IQ trace. In this section, the influence of amplitude change in the measurement light is briefly discussed.

Considering the coupling efficiency change, we can rewrite the measurement signal as $E_m = \alpha_m(t)\kappa_m A \exp\{i[2\pi f_0 t + \phi(t)]\}$, where $\alpha_m(t)$ indicates that the amplitude in the measurement signal changes with time. Because the measuring surface is vibrating, $\alpha_m(t)$ turns out to be a periodic signal with a frequency

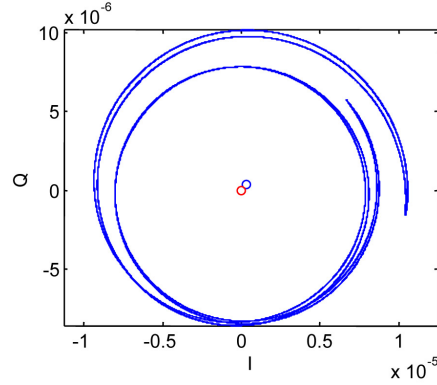


Figure 2.9: The IQ Lissajous curve with a coupling modulation

$$\alpha_m(t) = [1 + 0.1 \cos(2\pi f_v t) + 0.1 \cos(4\pi f_v t)].$$

equal to f_v , which is the vibrating frequency of the target. An example is shown in figure 2.9. It can be found that, under such an amplitude modulation, the IQ Lissajous curve is not an ellipse anymore. The trace shape is determined by the imaging system, and may be different from case to case.

If the Lissajous curve center (I_{dc} , Q_{dc}) can be successfully obtained, the recovered phase $\theta'_D(t)$ from the “arc-tangent” method should equal $\theta_D(t)$. However, the change of $\alpha_m(t)$ leads to a varying Lissajous curve center, which increases the difficulty in finding the correct center. As is shown in figure 2.9, the center of the trace found by the previously used “center-finding” algorithm is not at the real center (red circle). In order to solve this problem, we suggest using a balanced detection, which helps to cancel the DC variations in the PDs.

2.3.6 Influence of noise

The influence of noise on the demodulated phase shift in the heterodyne case can also be calculated using Eq. 2.33. However, since the most significant low frequency noise in PDs is removed in the heterodyne case, the SNR is usually much larger than in the homodyne case. That’s the reason why heterodyne LDV has a better spatial resolution than homodyne.

2.4 Conclusions

In this chapter, we have discussed the basic building blocks in LDV systems and the demodulation methods for two typical detection schemes. We found that except the noise issues, several important imperfections may also strongly influence the

LDV outputs. For homodyne, these are the imperfect 90° optical hybrid and device spurious reflections; for heterodyne, these are the imperfect frequency shift and on-chip spurious reflections.

It is also found that some compensation algorithms can be used to alleviate the influence of spurious reflections, imperfect 90° optical hybrid, and residual harmonics in the frequency shift. The problems with the spurious reflections exist in both detection schemes, but they have different impacts to the LDV outputs: in homodyne it mainly changes the eccentricity of the IQ curve, while in heterodyne the effect is to shift the whole IQ curve.

Though these compensation algorithms are successful under ideal situations, in practice noise does deteriorate the compensation. In order to solve this problem, we should try to reduce these deviations by improving the on-chip designs. The reflectionless designs on SOI chip are going to be discussed in Chapter 3, and the sideband-suppressed optical frequency shifter will be addressed in Chapter 4. In these two chapters, we will present several novel designs that can greatly improve the performance of on-chip LDVs.

References

- [1] <http://www.polytec.com>.
- [2] W. Bogaerts, R. Baets, and P. Dumon. *Nanophotonic waveguides in silicon-on-insulator fabricated with CMOS technology*. *Journal of Lightwave Technology*, 23(1):401–412, 2005.
- [3] A. Drabenstedt, J. Sauer, and C. Rembe. *Remote-sensing vibrometry at 1550 nm wavelength*. In 19th International conference on Vibration Measurements by Laser and Noncontact Techniques, volume 113, pages 113–121, AIVELA, 2012.
- [4] M. Bass, E. W. Van Stryland, D. R. Williams, and W. L. Wolfe, editors. *Handbook of Optics, Volume I - Fundamentals, Techniques, and Design*. McGraw-Hill, 2 edition, 1995.
- [5] D. Liang and J. E. Bowers. *Recent progress in lasers on silicon*. *Nature Photonics*, 4:511–517, 2010.
- [6] S. Stankovic, R. Jones, M. N. Sysak, J. M. Heck, G. Roelkens, and D. Van Thourhout. *Hybrid III-V/Si Distributed-Feedback Laser Based on Adhesive Bonding*. *IEEE Photonics Technology Letters*, 24:2155–2158, 2012.
- [7] S. K. Selvaraja, W. Bogaerts, and D. Van Thourhout. *Loss reduction in silicon nanophotonic waveguide micro-bends through etch profile improvement*. *Optics Communications*, 284(8):2141–2144, April 2011.
- [8] M. Bachmann, P. A. Besse, and H. Melchior. *Overlapping-image multimode interference couplers with a reduced number of self-images for uniform and nonuniform power splitting*. *Applied optics*, 34(30):6898–6910, 1995.
- [9] R. Halir, G. Roelkens, A. Ortega-Moñux, and J. G. Wangüemert-Pérez. *High-performance 90 degree hybrid based on a silicon-on-insulator multimode interference coupler*. *Optics Letters*, 36(2):178–80, January 2011.
- [10] M. Bachmann, P. A. Besse, and H. Melchior. *General self-imaging properties in NxN multimode interference couplers including phase relations*. *Applied Optics*, 33(18):1994, 1994.
- [11] D. Taillaert, P. Bienstman, and R. Baets. *Compact efficient broadband grating coupler for silicon-on-insulator waveguides*. *Optics Letters*, 29(23):2749–2751, 2004.
- [12] G. Roelkens, D. Van Thourhout, and R. Baets. *High efficiency Silicon-on-Insulator grating coupler based on a poly-Silicon overlay*. *Optics Express*, 14(24):11622–11630, 2006.

-
- [13] D. Vermeulen, S. Selvaraja, P. Verheyen, G. Lepage, W. Bogaerts, P. Absil, D. Van Thourhout, and G. Roelkens. *High-efficiency fiber-to-chip grating couplers realized using an advanced platform*. *Optics Express*, 18(17):18278–18283, 2010.
- [14] F. Van Laere, T. Claes, and J. Schrauwen. *Compact focusing grating couplers for silicon-on-insulator integrated circuits*. *IEEE Photonics Technology Letters*, 19(23):1919–1921, 2007.
- [15] Y. Li, L. Li, B. Tian, G. Roelkens, and R. Baets. *Reflectionless tilted grating couplers with improved coupling efficiency based on a silicon overlay*, 2013.
- [16] L. Zimmermann, K. Voigt, G. Winzer, K. Petermann, and C. M. Weinert. *C-Band Optical 90-Hybrids Based on silicon-on-insulator 4×4 waveguide couplers*. *IEEE Photonics Technology Letters*, 21(3):143–145, 2009.
- [17] V. S. Sudarshanam and K. Srinivasan. *Linear readout of dynamic phase change in a fiber-optic homodyne interferometer*. *Optics Letters*, 14(2):140–2, January 1989.
- [18] W. Jin, L. M. Zhang, D. Uttamchandani, and B. Cuishaw. *Modified J1...J4 method for linear readout of dynamic phase changes in a fiber-optic homodyne interferometer*. *Applied optics*, 30(31), 1991.
- [19] J. La, S. Wang, K. Kim, and K. Park. *High-speed FM demodulator of a homodyne laser interferometer for measuring mechanical vibration*. *Optical Engineering*, 43(6):1341, 2004.
- [20] Thorlabs. *Manual: Balanced Amplified Photodetectors*, 2012.
- [21] D. Christiansen, C. K. Alexander, and R. K. Jurgen. *Standard handbook of electronic engineering*. McGRAW-HILL, 5 edition, 2004.

3

Low-reflection optical components on SOI

3.1 Introduction

As is mentioned in Chapter 2, spurious reflections have a significant influence on the LDV outputs. To obtain high quality LDV outputs, the total power of the spurious reflection should be 30-40 dB lower than that of the useful signal, which is however not fulfilled in many SOI-based photonic devices. These spurious reflections often occur at the interfaces between two different materials or structures, e.g. the boundary between a rib waveguide (450 nm wide) and a slab waveguide (infinitely wide). A PIC-based LDV system may have several such interfaces with its optical components, especially in grating couplers (GCs) and optical splitters.

In this chapter, we will discuss the origins of these spurious reflections and demonstrate some methods to suppress them. The following sections are organized as follows. Firstly, we demonstrate several grating coupler designs with strongly reduced backreflection. Afterwards, multimode interference (MMI) couplers with low backreflection and high isolation are introduced. Finally is a short discussion about other possible spurious reflections on the SOI-based PIC.

This chapter includes works collaborated with other people: Section 3.2.2 and section 3.2.5 are the work collaborated with L. Li, B. Tian, G. Roelkens, and R. Baets; section 3.2.4 is the work collaborated with D. Vermeulen, Y. De Koninck, G. Yurtsever, G. Roelkens, and R. Baets; section 3.3 uses the simulation framework developed by E. Lambert, W. Bogaerts *et al*; the work of section 3.4 is

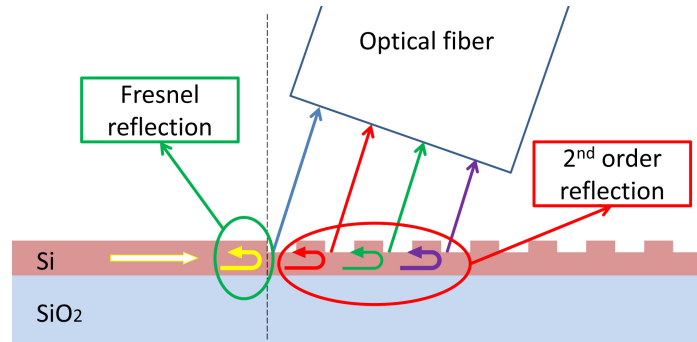


Figure 3.1: Schematic of Fresnel reflections and 2nd order reflections of a grating coupler.

finished with the help of S. Stankovic.

3.2 Low-reflection grating couplers

Surface grating coupler (GC) structures are extensively used in photonic integrated circuits (PICs) to couple light into and out of chips. Since this coupling method does not require polished waveguide facets on the edge of a photonic chip, it can thus be used in wafer-scale testing of PICs. Unlike the coupler design assisted with a spot size converter [1], these structures can be fabricated along with the other photonic components and no extra post-processing is needed. Thanks to these strengths, the GC structure becomes a good candidate for realizing on-chip light transmitting antennas (TAs) and light receiving antennas (RAs).

The waveguide to free space coupling efficiency is essential for a TA or an RA in the LDV, since it determines the SNR of the LDV photocurrent. Regarding the coupling efficiency and transmission bandwidth, the GC structures have been thoroughly studied in a lot of publications [2–4]. Depending on different methods, the waveguide-to-fiber coupling efficiency on SOI can be 35% (standard grating coupler) or 69% (with silicon overlay) [3].

Another concern of the GC design is the on-chip back-reflection. In general, two types of reflections may be introduced in a GC (see figure 3.1): the second order Bragg reflection of the grating and the Fresnel reflection due to the mode mismatch between the grating and the input waveguide regions. The zenith of the fiber ϕ (the angle between the normal of the PIC surface and the direction of the fiber) is often set as 10° or more to ensure that the second order reflection is suppressed in the wavelength range of interest. However, the Fresnel reflection can still be reflected back to the waveguide.

A technique called the optical frequency domain reflectometry (OFDR) can be

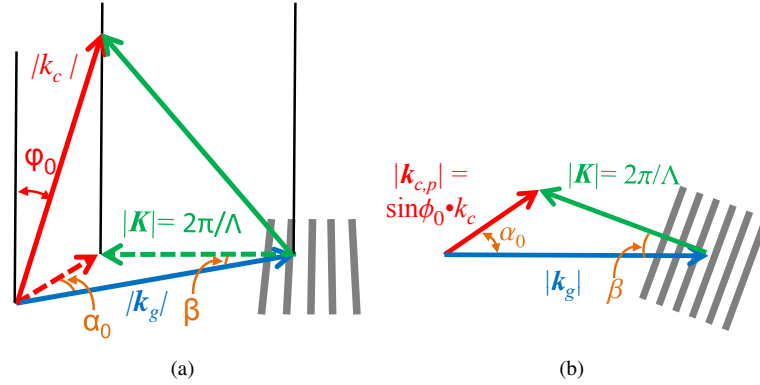


Figure 3.2: (a) 3D wave vector relations in a tilted 1D grating coupler; (b) Relations of the projections of the wave vectors on the chip surface.

used to measure the reflection of a grating coupler (see appendix A). Measurement results show that, for a standard grating coupler (630 nm grating period, 220 nm waveguide height, and 70 nm trench depth), the power ratio of the spurious reflection to the input light is around -20 dB. This value is not acceptable in the LDV system. Previous publications have suggested several different methods to suppress this back reflection, i.e. improving the mode matching between the grating region and input waveguide [5, 6], or using an apodized GC design [7, 8]. However, their reflection suppressions are still not strong enough. In addition, some of them require an electron-beam lithography for fabrication.

To ensure a sufficient suppression in the spurious reflection of GCs, we propose to use a tilted design, in which the trenched gratings are purposely tilted so that the angle of incidence of the incoming light is not zero. With this design, the Fresnel reflection will be sent to somewhere else rather than the input waveguide. Hence less reflection is realized. We will see that the reflection suppression with this method is much better than those from previously reported methods. This new method will be discussed in detail in the following sections.

3.2.1 Tilted 1D grating couplers

In normal GC designs, the grating trenches are perpendicular to the light from the entrance waveguide. If the grating trenches are tilted, the coupling situation will be changed, which is shown in the 3D schematic in figure 3.2(a). For a tilted 1D GC structure, the relations among the wave vector of the input light (\vec{k}_g), the reciprocal lattice vector of the grating (\vec{K}), and the projection of the output light wave vector onto the chip surface ($\vec{k}_{c,p}$) are shown figure 3.2(b). According to

these relations, the tilt angle β of the GC and the grating period Λ are defined by the required direction of the output light, being described by the zenith angle ϕ_0 and the azimuth α_0 , with the following equations:

$$\beta(\phi_0, \alpha_0) = \arctan\left(\frac{n_{c,p} \sin \alpha_0}{n_g^0 - n_{c,p} \cos \alpha_0}\right), \quad (3.1)$$

$$\Lambda(\phi_0, \alpha_0) = \frac{\lambda_0 \cos \beta(\phi_0, \alpha_0)}{n_g^0 - n_{c,p} \cos \alpha_0}, \quad (3.2)$$

where $n_{c,p} = n_c \sin \phi_0$, λ_0 is the vacuum wavelength of the light, n_g^0 is the effective index of the light propagating in the waveguide corrugated by the grating, and n_c is the refractive index of the superstrate (air in this case), respectively. Note that the refraction of light on the boundary of the GC and the slab region is not considered here, because the angle change due to refraction is relatively small ($< 1^\circ$) in our designs.

With this design, both the out-coupled light direction and the reflected light direction are changed. Since the reflected light is not sent directly to the source of the incoming light, the on-chip spurious reflection may be reduced.

3.2.2 Enhancement transmission in tilted 1D GCs

Sometimes, it is necessary to improve the transmission of the GC. According to [3, 9], an extra Si overlay (polycrystalline or amorphous) with a thickness of 160 nm can be locally deposited on top of a 1D GC to increase the fraction of the upward diffracted power, so as to increase the waveguide-to-fiber coupling efficiency. The cross section of such a GC is shown in figure 3.3(a).

The 3D finite difference time domain (FDTD) method is used to analyze the power directionality of a tilted GC with a Si overlay. Considering the speed of the 3D FDTD simulations, there are some simplifications in the simulation.

- The simulation domains (the dashed box in figure 3.3(a)) do not include the lower boundary of the 2 μm oxide layer. This is an acceptable approximation according to [9], which demonstrated that the influence of this boundary is not important for the GCs with Si overlays. This assertion is also confirmed by a 2D FDTD simulation, showing that the upward power of a GC with Si overlays is only increased by 0.7 dB (at 1550 nm) after considering this oxide layer.
- The widths of the input waveguide and the GC are shortened from 10 μm to 4 μm to further reduce the simulation time. For calculating the fraction of the upward diffracted power, this is a good approximation. However, this simplification can not be used for tilted FGCs, since FGCs do not have a translational invariance in any direction. Therefore, the simulations of tilted

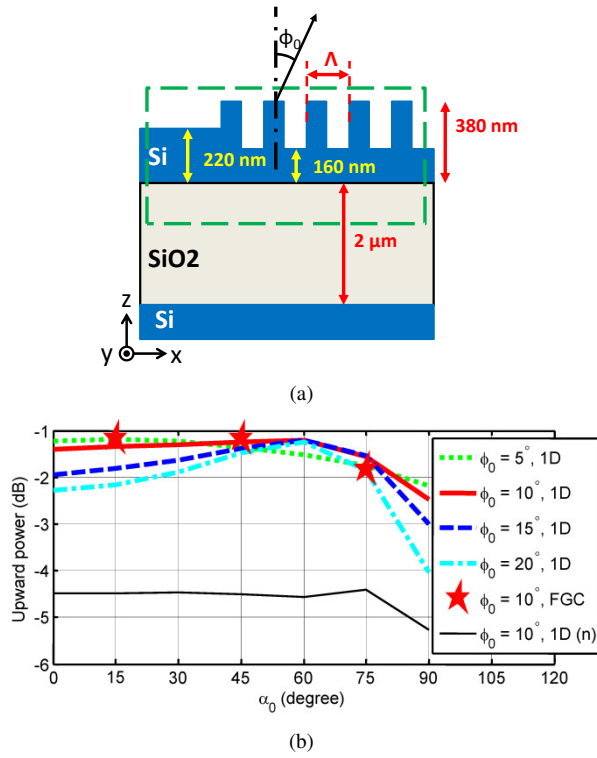


Figure 3.3: (a) The cross-section of a grating coupler with a silicon overlay; (b) Fractions of light coupled into the upward direction of different tilted GCs as a function of the azimuth α_0 ($\lambda_0 = 1550$ nm). The curves called “1D” are for the tilted 1D GCs with a 160 nm thick Si overlay, the curves called “1D (n)” are for the tilted 1D GCs without Si overlay, and the curve called “FGC” is for a tilted FGC designed for $\alpha_0 = 15^\circ, 45^\circ, 75^\circ$.

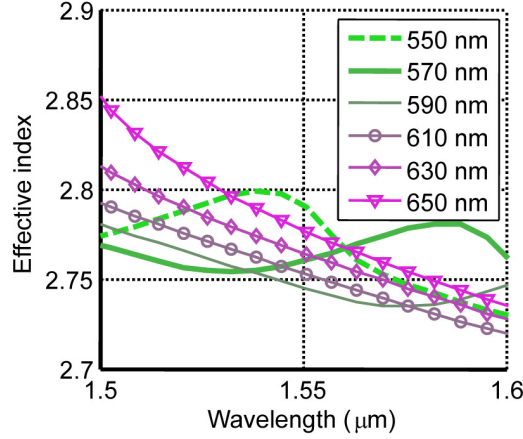


Figure 3.4: The effective indices of 1D grating couplers with silicon overlay as a function of wavelength and grating period. In this case $\beta = 0^\circ$.

FGCs are more time and memory consuming compared to those of tilted 1D GCs.

The upwardly coupled power ratio ($\lambda_0 = 1550$ nm) of four groups of tilted 1D GC designs ($\phi_0 = 5^\circ, 10^\circ, 15^\circ$ and 20°) with 160 nm Si overlays are simulated as functions of α_0 values, and the results are illustrated in figure 3.3(b). The tilted 1D GC designs in this simulation follow the expressions of Eq. 3.1 and Eq. 3.2, with assumptions that $n_g^0 = 2.75$, $n_c = 1.0$, and the duty cycle of the gratings is 50% everywhere. From the simulation results, it is seen that the upward power transmissions of the tilted 1D GC designs with $\phi_0 = 10^\circ$ are larger than -1.5 dB for $\alpha_0 \leq 60^\circ$, and the variation among these transmissions is also smaller than those with other ϕ_0 values. Therefore the condition $\phi_0 = 10^\circ$ is used for further discussions. Another phenomenon is that the upwardly coupled power drops rapidly when α_0 increases from 75° . This is because the period Λ approaches the value supporting a strong 2nd order reflection as α_0 increases.

3.2.3 Angle deviation in the out coupled light

One problem with this design is that n_g^0 can be wrongly estimated. The effective indices of 1D GCs ($\beta = 0^\circ$) as functions of Λ and λ_0 are calculated by means of 2D FDTD simulation. In the simulation, we first calculate the phase slope $k_{phi} = \Delta\Phi/\Delta L$ of light along its propagation direction in the grating region, and this slope value is used for the effective index approximation according to $n_g^0 = k_{phi} \cdot \lambda_0/2\pi$. The results (see figure 3.4) show that the n_g^0 value changes

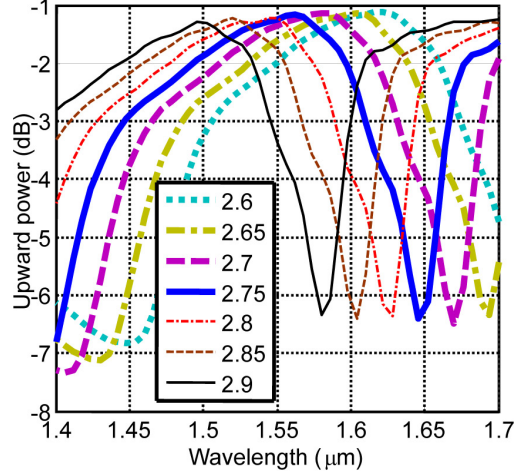


Figure 3.5: Spectra of the upward coupled power of tilted 1D GCs with silicon overlay ($\alpha_0 = 45^\circ$), for different n_g values.

with wavelength and grating period, and can be strongly deviating when Λ supports strong 2nd order reflections (see the curves for $\Lambda = 550$ nm and $\Lambda = 570$ nm in figure 3.4). Even if an accurate effective index value is obtained from simulation, the variation caused by fabrication uncertainty is hardly controllable.

As a result, the value of n_g^0 used in Eq. 3.1 and Eq. 3.2 is usually different from the actual effective index of the grating. For clarification, a symbol n_g is used to stand for the refractive index value used in the design, in order to be distinguished from the actual index of the grating n_g^0 . The difference between n_g and n_g^0 causes a direction change in the output light and thus a shift in its transmission spectrum.

To find out the value of n_g^0 in real devices, one can make a scan of n_g and test the corresponding transmissions in measurement. However, scanning n_g is not a proper solution in many cases. The central wavelength shift is caused by the direction change of the output light with the required wavelength. By adjusting the direction of the output fiber to accommodate the new direction of the output light, the central wavelength can be changed back to the required value.

The changed direction of the output light (α'_0, ϕ'_0) is theoretically calculated as a function of $\Delta n_g = n_g - n_g^0$, which is

$$\alpha'_0 = \alpha_0 + \arctan \left(\frac{\Delta n_g \sin \alpha_0}{n_{c,p} - \Delta n_g \cos \alpha_0} \right), \quad (3.3)$$

$$\phi'_0 = \arcsin \left(\frac{\sqrt{n_{c,p}^2 + \Delta n_g^2 - 2n_{c,p} \Delta n_g \cos \alpha_0}}{n_c} \right). \quad (3.4)$$

The derivations of these two equations are explained in Appendix B.

The wavelength for maximal transmission depends also on the GC period. Since a wrong estimation of n_g^0 leads to a period change, it will also cause a change in the peak wavelength. According to a 3D FDTD simulation, the spectra of the upward coupled light for 1D GCs with $\alpha_0 = 45^\circ$, $\phi_0 = 10^\circ$, and $\lambda_0 = 1550$ nm are shown in figure 3.5 as functions of n_g . It can be found that the spectrum has a blue shift as n_g increases. The designs with $n_g = 2.75$ and 2.8 have the optimal upward coupling efficiencies at 1550 nm. If other n_g values are used, the coupling efficiencies at 1500 nm will not be optimized, even with corrections in the direction of the output fiber.

3.2.4 Tilted Focusing grating couplers

For tilted 1D GC, the incoming light in the slab should have a planar wavefront, which requires a longer distance between the normal waveguide (450 nm thickness) and the grating coupler. In this situation, the footprint of the PIC device is limited by these long tapers and cannot be greatly reduced. To solve this problem, Van Laere *et al.* [10] have proposed a compact focusing grating coupler (FGC) design on SOI, which has an eight-fold length reduction compared to a fiber coupler with a taper. In this section, we will theoretically and experimentally demonstrate a low-reflection focusing grating coupler design [11, 12] which is similar to the FGC reported by Van Laere *et al.* [10].

The trench shapes in the FGC reported in [10] can be expressed in a polar coordinate system

$$r(q, \alpha) = \frac{q\lambda_0}{n_g^0 - n_c \sin \phi_0 \cos \alpha}, \quad (3.5)$$

where $r(q, \alpha)$ represents the length of each grating to the origin, α is the corresponding azimuth, $q \in N$ is the index of each line, λ_0 is the central wavelength of light in vacuum, ϕ_0 is the zenith of the coupling direction in free space, and n_g^0 and n_c are the effective indices of the grating region and the top cladding material, respectively. In this formula, it is assumed that the effective index value of the slab region n_s is the same as n_g^0 , which is however not exact.

Considering the effective index difference between n_s and n_g^0 , a more general equation is derived (see Appendix B):

$$r(q, \alpha) = \frac{(q - q_0) \cdot \lambda_0}{n_g^0 - n_c \sin \phi_0 \cos \alpha} + p(q_0, \alpha), \quad q = q_0, q_0 + 1, \dots, \quad (3.6)$$

where

$$p(q_0, \alpha) = \frac{\kappa q_0 \lambda_0}{n_s - n_c \sin \phi_0 \cos \alpha}, \quad (3.7)$$

$q_0 \in N$ is the index of the first line in the grating, and κ is a factor to determine the distance L between the first line and the entrance waveguide. In this thesis, κ

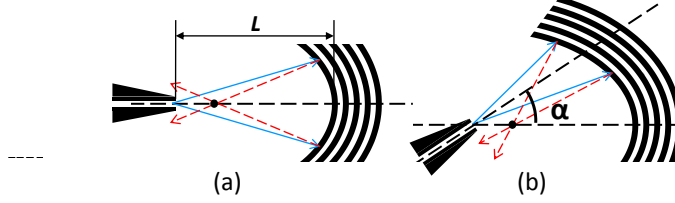


Figure 3.6: Schematic of tilted FGCs (exaggerated) on SOI with different azimuths: (a) $\alpha = 0$, (b) $\alpha \neq 0$. The black region is etched 70 nm into a 220 nm silicon layer while the rest is unetched. The light lines diffracting from the waveguide and the Fresnel reflections are indicated with the blue and red lines, respectively.

is chosen as $(n_s - n_c \sin \phi)/(n_g^0 - n_c \sin \phi_0)$ so that $r(q_0, 0)$ is the same as that from the conventional design. A similar formula was also reported in [13].

These curves form an array of ellipses with all of their first focus points $f_{1,q}$ located at the same position. According to Eq. 3.6, if the end of the entrance waveguide is located on $f_{1,q}$, light coming from this waveguide can be coupled out of the chip to the predesigned direction in free space, regardless the choice of α . In previously used FGCs [10] (will be mentioned as the standard FGC afterwards), the input waveguide points to the grating region with $\alpha = 0^\circ$ (seen in figure 3.6(a)). Actually, light can be coupled to almost the same predesigned direction if the input waveguide is rotated around $f_{1,q}$ and another part of the grating is used (the actual coupling direction might be slightly different due to the second order reflection). In the case with $\alpha \neq 0^\circ$, the back reflection which is refocused on a location near the second focus points of the ellipses $f_{2,q}$ will not be coupled back to the input waveguide (seen in figure 3.6(b)). Therefore the reflection back to the input waveguide can be suppressed with a different part of the FGC design. The reduced reflection in this design has been demonstrated by means of simulation [14], and the results confirm the suppression in the back reflections for the FGCs with $\alpha = 45^\circ$ or 90° .

The redirected backreflection may influence adjacent designs. To avoid this influence, the back-reflection can be collected to another waveguide and then sent to a high loss region. Another concern about this design is the asymmetry of the output mode. This asymmetry exists but is sometimes not significant when $\phi = 10^\circ$, thus its influence on the grating-to-fiber coupling efficiency is negligible.

A series of tilted FGCs (with different α) designed to couple 1550 nm light to the direction with $\phi = 10^\circ$ has been fabricated using deep UV (193 nm) lithography through the ePIXfab multi-project wafer service [15]. The width of the entrance waveguide aperture ($0.9 \mu\text{m}$) was chosen to be neither too small to introduce extra reflection nor too large to collect the redirected Fresnel reflection from the grating. As is mentioned above, the azimuth of the out coupled light equals

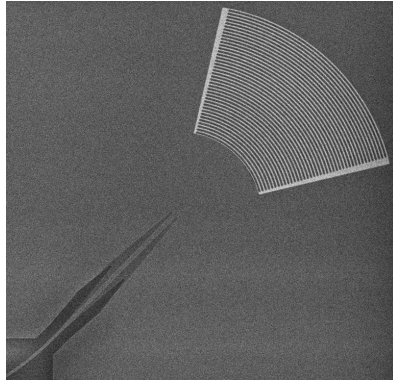


Figure 3.7: A scanning electron microscope image of a tilted FGC designed for $\alpha = 45^\circ$.

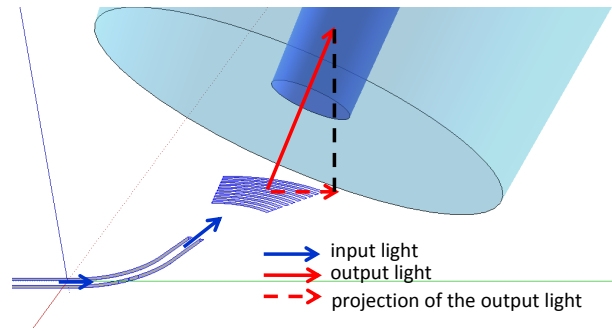


Figure 3.8: 3D Schematic of a tilted FGC (exaggerated) on SOI and its corresponding output fiber.

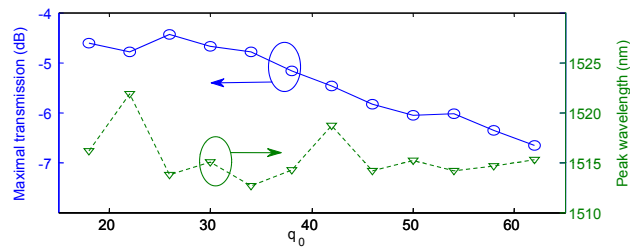


Figure 3.9: Maximal coupling efficiency between a single mode fiber and FGCs with different q_0 values and corresponding central wavelengths. The width of the waveguide aperture is $0.9 \mu\text{m}$.

α_0 . In many measurement setups, it is not possible to change the azimuths of the fibers. In order to be used in these setups, the tilted FGCs and the input waveguides are purposely rotated around the surface normal with an angle of $-\alpha_0$ when they are designed on the PIC (see figure 3.7 and figure 3.8). The alignment procedure for these tilted FGCs is similar to that for a standard GC.

The distance L determines the size of the output mode in the grating coupler and thus influences the maximal grating-to-single-mode-fiber coupling efficiency η . In order to know the optimal value of L , a number of FGCs ($\alpha = 0^\circ$) with different first grating indices q_0 were fabricated and measured. The η values of different FGCs and the corresponding central wavelengths λ_0 are plotted in figure 3.9. It is found that the best q_0 is 26 ($L = 16 \mu\text{m}$). All the following designs use this q_0 value. The variation of the λ_0 is within 5 nm, and it might be caused by the alignment variations of fibers.

Designs with two identical tilted FGCs connected by a shallowly etched waveguide were measured to retrieve η for different α , and these transmission spectra are plotted in figure 3.10. The η and λ_0 values are plotted in figure 3.11. The solid horizontal line in figure 3.11 stands for the η of a standard FGC (-4.6 dB). It can be found that the λ_0 values are lower than 1550 nm. Two main reasons are responsible for this shift:

- n_g and ϕ_0 are wrongly estimated in the design, and hence the measured central wavelength becomes $\lambda' = \lambda_0(n'_g - n_c \sin \phi'_0 \cos \alpha) / (n_g - n_c \sin \phi_0 \cos \alpha)$, where n'_g and ϕ'_0 stand for the real values of n_g and ϕ_0 , respectively. This expression indicates that λ' is a function of α , which can also be seen in the measurement results (see figure 3.10);
- The wavelength supporting the second order reflection has a blueshift as α increases, and the dip caused by this second order reflection strongly influences the transmission spectra of the tilted FGCs when α is close to 90° . The effect of this reflection dip is shown by both suppression of η and a shift of λ_0 . However, this influence is not apparent for $\alpha \geq 150^\circ$ or $\leq 60^\circ$, since the λ_0 of second order reflection stays far away from the transmission band in these situations. Note that the second order reflection also may cause a bandwidth increase in the tilted FGCs when α is approaching 90° .

It is hard to estimate the reflections directly from the fringes of the transmission spectra, because the reflections on the output fiber end facets are also mixed in the spectrum. In order to measure the reflection values of our tilted FGCs, we use another set of samples. In those samples, all the input FGCs use the same design with $\alpha = 0^\circ$, while the output tilted FGCs have a scan of the azimuth from 0° to 180° . The frequency average reflections are measured by a simplified optical frequency domain reflectometry (OFDR) setup (see Appendix A).

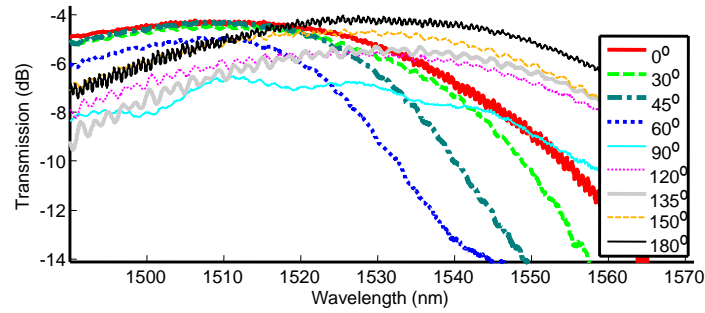


Figure 3.10: The transmission spectra of the tilted FGCs with different azimuths.

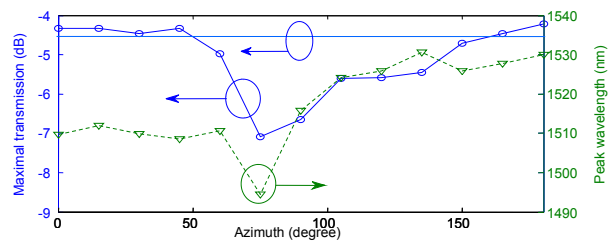


Figure 3.11: The maximal transmission efficiencies of the tilted FGCs and the corresponding central wavelengths. The horizontal line stands for the η of a standard FGC.

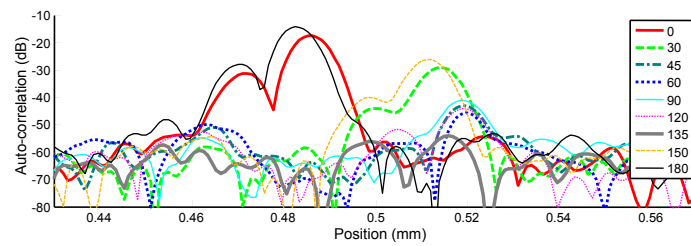


Figure 3.12: The peaks in the autocorrelation $R(z)$ caused by the reflection from the output tilted GCs with different azimuths. The autocorrelations are plotted in a logarithmic scale ($20 \times \log(R(z))$).

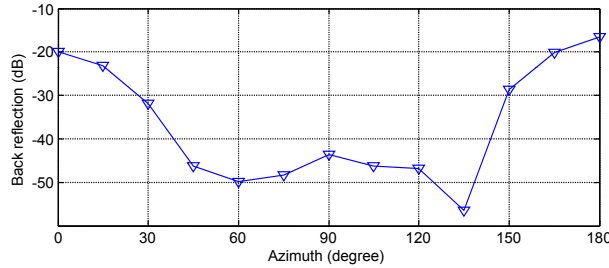


Figure 3.13: The maximal frequency averaged reflections of the tilted FGCs for different azimuths.

The distances between the input and output tilted FGCs are around $500 \mu\text{m}$, but not exactly the same. The reflection autocorrelations $R(z)$ for different azimuths with z near $500 \mu\text{m}$ are plotted in figure 3.16. Two maximal values can be found for each sample, which means that two different reflections are correlated with the reflection at the output tilted FGC. They are the reflections from the input fiber facet and from the input GC, respectively, and the former one corresponds to a larger z . The reflectance values of the tilted FGCs are obtained by calculating the integral over the 3 dB bandwidth around λ_0 . The frequency averaged reflections for different α are plotted in figure 3.13. Assuming that a 4% reflection occurs at the input fiber facet, the frequency average reflection for an FGC with $\alpha = 0^\circ$ is around -20 dB. Grating couplers with α between 45° and 135° have the frequency average back reflection suppressed to less than -40 dB. The best reflection suppression is for $\alpha = 135^\circ$, which is around -55 dB. The optimal α is not 90° , and that is because the central wavelength value of the second order reflection is near the transmission peak in this case.

For tilted FGCs with the azimuth α in the range between 45° and 60° , the frequency average reflection is highly suppressed (up to -50 dB) with no apparent transmission penalty.

3.2.5 Tilted Focusing grating couplers with silicon overlay

We also report about the coupling efficiency of different tilted focusing grating coupler (FGC) designs with Si overlays, by means of simulation and measurement.

The upward power coupling efficiency of tilted FGCs with the same Si overlay (designed for $\alpha_0 = 15^\circ, 45^\circ$ and 75°) are also simulated and shown in figure 3.3(b). It is seen that the upward powers of the tilted FGC with Si overlay have similar values to those of the tilted 1D GCs with Si overlay designed with the same α_0 and ϕ_0 . These results show that the upward power of tilted FGCs with Si overlay can be simply estimated from the results of tilted 1D GCs with Si overlay.

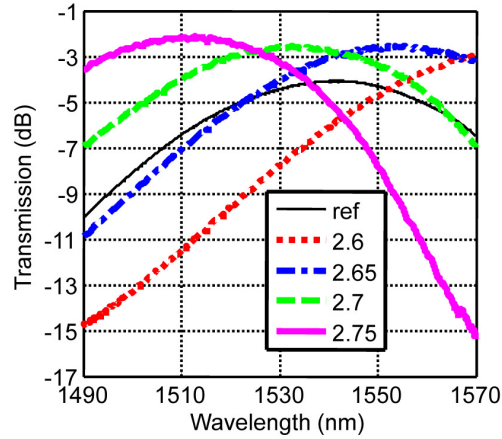


Figure 3.14: Measured transmission spectra of four tilted FGCs with Si overlays with different n_g values, $\alpha_0 = 45^\circ$. The “ref” curve stands for the transmission spectrum of a standard GC without any Si overlay.

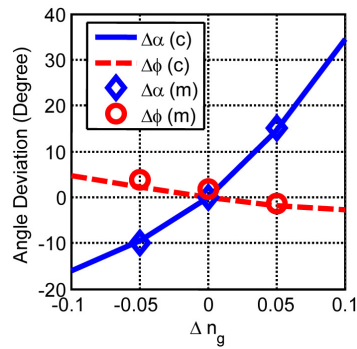


Figure 3.15: The deviation of α_0 and ϕ_0 as a function of Δn_g . The solid and curved lines are calculated values. The \diamond and \circ symbols are the measured values.

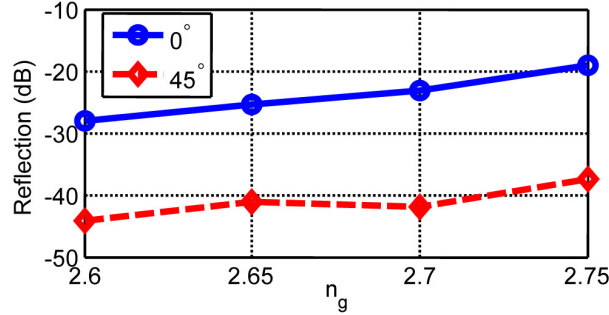


Figure 3.16: The reflection values for FGCs with $\alpha_0 = 0^\circ$ (solid line) and tilted FGCs with $\alpha_0 = 45^\circ$ (dashed line). Both are with 160 nm thick Si overlay.

A number of tilted focusing grating couplers with amorphous-Si overlays, designed for $\alpha_0 = 0^\circ$ or 45° , and $\phi_0 = 10^\circ$, were fabricated through ePIXfab. Since it is not easy to estimate the n_g^0 value of a grating with silicon overlay, a number of different values of n_g were used in Eq. 3.6 for the design instead of n_g^0 , so as to have different grating periods and shapes, out of which there may be a good design. The transmission spectra and the central wavelengths of tilted FGCs designed for $\alpha_0 = 45^\circ$ with different n_g values are shown in figure 3.14. It can be seen that, for the tilted FGCs with silicon overlay, the waveguide-to-single mode fiber coupling losses are reduced by more than 2 dB compared to a standard FGC (“ref” in figure 3.14, without Si overlay, 70 nm etch depth, 625 nm period), and it is also 2 dB lower than that of the tilted FGCs without Si overlay ($\alpha_0 = 45^\circ$, 70 nm etch depth). The lowest transmission is around -2.2 dB when $n_g = 2.75$, and this value is 0.5 dB lower than that of a normal FGC with silicon overlay ($\alpha_0 = 0^\circ$) which is designed with the same n_g value. The central wavelength decreases linearly as n_g increases, with a slope of $-0.4 \mu\text{m}$ per unit of index. The scanning results show that the real effective index n_g^0 at 1550 nm is about 2.65.

As is mentioned above, the central wavelength shift for different n_g can be compensated by changing the fiber direction, which was also observed in the measurements. For both the tilted 1D GC and tilted FGC designs, the angle deviations calculated by Eq. 3.3 and Eq. 3.4 can be used for adjusting the output fiber direction and getting an optimized coupling efficiency. For $\alpha_0 = 45^\circ$ and $\phi_0 = 10^\circ$, the angle deviations $\Delta\alpha_0 = \alpha'_0 - \alpha_0$ and $\Delta\phi_0 = \phi'_0 - \phi_0$ are calculated according to these equations and are shown in figure 3.15. The measured deviations of the output light ($\Delta\alpha_0$ and $\Delta\phi_0$) are also shown in the same figure to indicate the agreement between the theoretical analysis and the measurement results.

The back reflections of tilted FGCs with $\alpha_0 = 0^\circ$ and 45° are obtained using the OFDR method. This time we use fringes in the transmission for the reflection

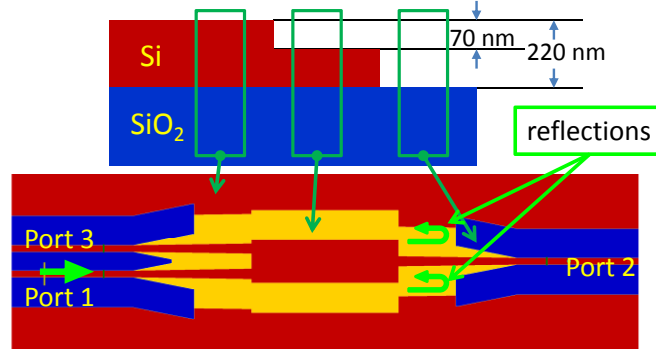


Figure 3.17: The top view of a 2×1 MMI.

calculation. In order to split the reflections from the fiber end and those from the GCs, the end facets of both the input and output fibers are placed far away from the GCs. The results are shown in figure 3.16. It is found that, for $\alpha_0 = 0^\circ$, the reflections are still considerably large (near -20 dB). For tilted FGCs with $\alpha_0 = 45^\circ$, the reflection averaged in the frequency range from 1490 nm to 1570 nm can be reduced to lower than -40 dB. Note that these tilted FGCs with $\alpha_0 = 45^\circ$ are the same tilted FGCs that yield the transmission spectra shown in figure 3.14.

3.3 Low-reflection multimode interference couplers

A 1×2 or a 2×2 multimode interference (MMI) coupler design is used in the on-chip LDV system for optical power splitting and combining. It has a highly balanced power splitting ratio between the two output ports. A reversed 1×2 MMI coupler, or a 2×1 MMI, is schematically shown in figure 3.17. It can be seen that the multi-mode waveguide section (the red box in the middle in figure 3.17) is surrounded by shallowly etched silicon slabs (the yellow region in figure 3.17) to avoid MMI phase errors due to high index contrast between the core and cladding regions [16].

However, spurious reflections may be introduced in these MMI structures as well. For example, when one left input port of the 2×1 MMI coupler (see figure 3.17) is excited, only 50% of the light power is transmitted to the right output port, while the rest power is leaked into the unused slab region of the chip or reflected to the two left ports by etching boundaries. We call the power ratio between the light coupled back to the input port (Port 1 in figure 3.17) and the input light as the MMI reflection. The power ratio of the input light (Port 1 in figure 3.17) to the light coupled to the other left port (Port 3 in figure 3.17) in the case that no reflection occurs in the waveguide connected to the output port (Port 2 in figure 3.17)

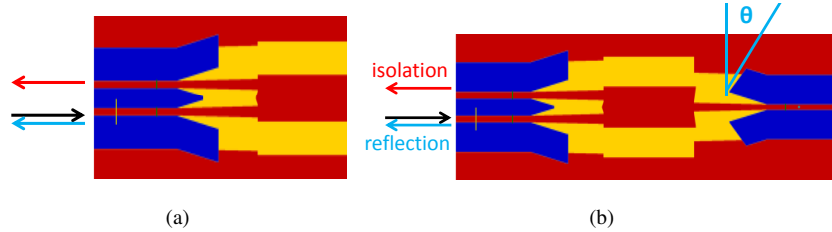


Figure 3.18: (a) Reference simulation (b) Simulation structure of the MMI.

is considered as the MMI isolation. These two parameters, especially the isolation, is important for the LDV performance. According to measurement results, the reflection is around -20 dB, which is higher than the required limit (-30 dB).

A close examination on this MMI structure indicates that the reflection is mainly caused by the boundaries of the deeply etched regions. Since these boundaries are perpendicular to the propagation direction of the leaked light, they can easily cause reflection. To reduce such reflections, one possible way is to tilt the boundaries with an oblique angle θ at each end of the MMI [17]. With this method, reflections are sent to the other regions away from the MMI, and thus low reflection and high isolation can be obtained.

3.3.1 Simulation

We have studied the effect of tilted etching boundaries in the MMI coupler by using the finite-difference time-domain (FDTD) method. The simulation structure is directly obtained from the mask design of the MMI with the help of the IPKISS framework [18, 19]. With the imported simulation structures, a Python-MEEP software package is used to make the FDTD simulation.

In the simulation, a source is put on the lower left input waveguide (Port 1 in figure 3.17), with the fundamental TE mode of the waveguide as its field profile. A light pulse with this field profile and a center frequency at 1550 nm is generated and sent to the MMI. By monitoring the energy flux in these three ports, transmissions from Port 1 to Port 2 and Port 3 can be calculated. In order to obtain the values of reflection and isolation, two simulation steps are done for each structure. The first simulation step is for a structure without the left-side reflection boundaries (see figure 3.18(a)), while the second one is for the actual MMI structure (see figure 3.18(b)). With this two-step method, the reflection and isolation can be estimated by calculating the flux difference of Port 1 and Port 3 between these two steps.

The simulated isolation and reflection results for 2×1 MMI couplers with different oblique angles are shown in figure 3.19(a) and figure 3.19(b). It is seen

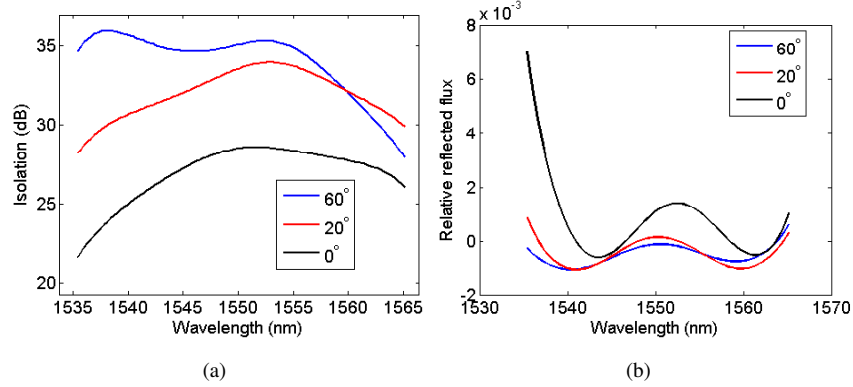


Figure 3.19: Simulation results for low-reflection MMIs: (a) isolation, (b) reflection.

from figure 3.19(a) that the isolation increases by more than 5 dB when the angle of the deeply etching boundaries is changed from 0° to 60° , and the maximal isolation can reach 35 dB. The reflection value is plotted in figure 3.19(b), which is calculated by subtracting the power flux in port 1 in the second step from that in the first step. It can be found that the reflected flux could be less than zero. This is because another reflection (probably occurs at the boundary between the input waveguide and the MMI) is neglected in the calculation. The interference between these two reflections causes a power fluctuation, which may lead to a negative flux value for some wavelengths. The reduced modulation depth for 60° tilt angle indicates that a reflection suppression is realized in this situation. However, it is difficult to calculate the exact reflection values with these simulation results. The optical power distributions in two structures representing the conventional and the improved MMI designs are shown in figure 3.20. It can be clearly seen that the reflection in the MMI design with oblique boundaries is directed to the substrate rather than being sent back to the left side.

One can also tilt the etching boundaries of the multimode region, which are the interfaces between the unetched region and shallowly etched region. But simulation results show that the corresponding improvement in isolation and reflection is not significant.

3.3.2 Measurement

The reflection reduction is also verified with measurements. The suppression of the reflection in a 2×1 MMI is measured using the optical frequency domain reflectometry (OFDR) method. In figure 3.21, the power spectral density of the reflection from the input port of two 2×1 MMI structures with different tilt angles

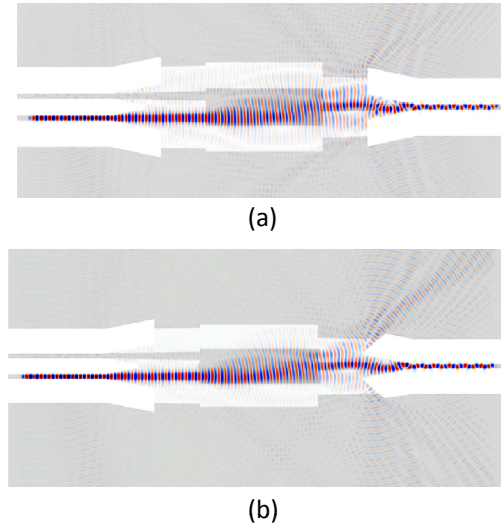


Figure 3.20: The energy flux in 2×1 MMI (a) conventional 2×1 MMI; (b) the improved 2×1 MMI with the deeply etched boundaries on the right side of the device tilted by 60° .

($\theta=0^\circ$ or 60°) of the deeply etched boundaries are shown. It can be found that the reflection of an MMI with $\theta = 60^\circ$ is 15 dB weaker than the conventional MMI couplers, and its value is around -35 dB lower than that of the input light.

The isolation measurement is a little tricky since the output power is very low and it can be easily influenced by variations in fiber alignment. Thus they were not obtained from these fabricated devices.

3.4 Other spurious reflections

Except the aforementioned two designs, other on-chip optical components may introduce spurious reflections as well.

Reflections can be introduced by the waveguide bends. Despite having a weak optical loss, a deeply etched waveguide bend with a radius of $5 \mu\text{m}$ has a strong spurious reflection. The reflection may originate from the mode mismatch between a straight waveguide and a circular bend. The estimated power of this reflection is around -20 dB less than the input light according to OFDR measurement. In order to reduce these reflections, we suggest using a bend larger than $10 \mu\text{m}$.

When the light signal is generated externally and sent to the chip via a fiber, another reflection peak can be found in the OFDR spectrum. By calculating the cavity distance of this spurious reflection in OFDR, it is found that this reflection

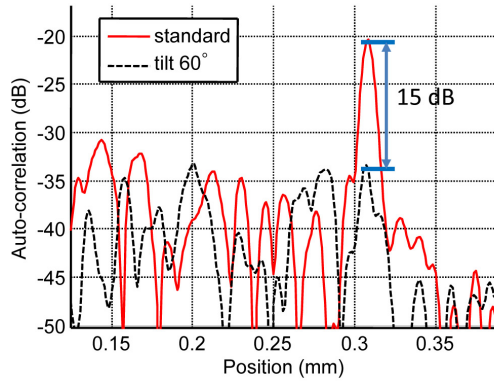


Figure 3.21: Reflections for two different 2×1 MMI couplers: the standard one with no boundary tilting and an improved one with a 60° tilt angle.

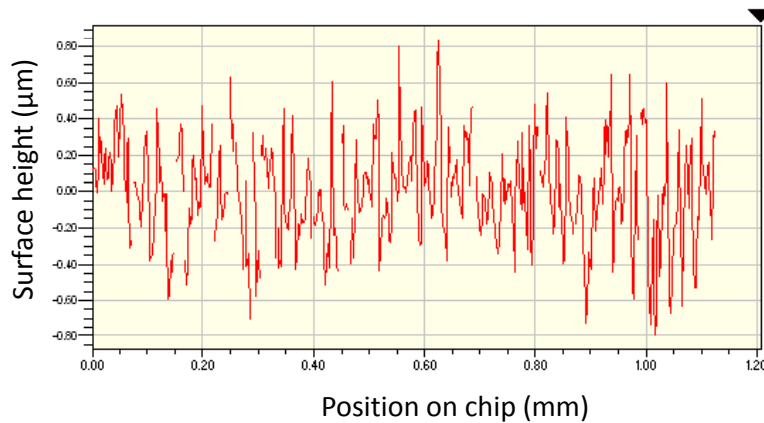


Figure 3.22: The roughness of the backside of the chip, with a root-mean-square deviation in height of $0.33 \mu\text{m}$.

is most probably from the backside of the chip. The backside of the chip is not polished and looks rather rough according to a white light interferometer measurement illuminated from back (see figure 3.22). Since a light beam from the top side of the chip usually covers several bumps of the back surface, it can be scattered to the top side of the chip. Some scattered light can be coupled back to the fiber as a spurious reflection. Since this scattered light signal may be directed to a grating coupler, it can be coupled back to the on-chip interferometer again and deteriorate the LDV outputs. This chip-backside reflection may be reduced by polishing the backside of the chip, or setting an anti-reflective or absorptive layer on the backside of the chip.

3.5 Conclusions

Spurious reflections of SOI-based optical designs are discussed in this chapter. It can be found that strong spurious reflections exist if on-chip designs are not carefully made. The spurious reflection of a grating coupler and the optical isolation between the two input ports of a 2×1 multimode interference coupler are mainly discussed, since these devices are used in the on-chip LDV system. In order to reduce these reflections, we purposely change the directions of some important mode-mismatching interfaces and direct the reflections to somewhere else rather than the input waveguide. With this method, the reflection in a grating coupler can be reduced to over 40 dB less than the input optical power. In 2×1 MMI couplers, the optical isolation between its two input ports can be larger than 35 dB. Therefore the requirement that the power of the spurious reflection is 30 dB lower than that of the incoming light (to ensure that the phase deviation of the LDV output is smaller than 0.01π) is realized.

References

- [1] G. Roelkens, P. Dumon, W. Bogaerts, D. Van Thourhout, and R. Baets. *Efficient silicon-on-insulator fiber coupler fabricated using 248-nm-deep UV lithography*. IEEE Photonics Technology Letters, 17(12):2613–2615, December 2005.
- [2] D. Taillaert, F. Van Laere, M. Ayre, W. Bogaerts, D. Van Thourhout, P. Bienstman, and R. Baets. *Grating Couplers for Coupling between Optical Fibers and Nanophotonic Waveguides*. Japanese Journal of Applied Physics, 45(No. 8A):6071–6077, August 2006.
- [3] D. Vermeulen, S. Selvaraja, P. Verheyen, G. Lepage, W. Bogaerts, P. Absil, D. Van Thourhout, and G. Roelkens. *High-efficiency fiber-to-chip grating couplers realized using an advanced platform*. Optics Express, 18(17):18278–18283, 2010.
- [4] A. Mekis and S. Gloeckner. *A grating-coupler-enabled CMOS photonics platform*. IEEE Journal of Selected Topics in Quantum Electronics, 17(3):597–608, 2011.
- [5] C. Alonso-Ramos, A. Ortega-Monux, I. Molina-Fernandez, P. Cheben, L. Zavargo-Peche, and R. Halir. *Efficient fiber-to-chip grating coupler for micrometric SOI rib waveguides*. Optics Express, 18(14):15189, 2010.
- [6] N. Na, H. Frish, I-W. Hsieh, O. Harel, R. George, A. Barkai, and H. Rong. *Efficient broadband silicon-on-insulator grating coupler with low backreflection*. Optics Letters, 36(11):2101, May 2011.
- [7] R. Halir, P. Cheben, and S. Janz. *Waveguide grating coupler with subwavelength microstructures*. Optics Letters, 34(9):1408–1410, 2009.
- [8] M. Antelius, K. B. Gylfason, and H. Sohlström. *An apodized SOI waveguide-to-fiber surface grating coupler for single lithography silicon photonics*. Optics Express, 19(4):3592–8, February 2011.
- [9] G. Roelkens, D. Van Thourhout, and R. Baets. *High efficiency Silicon-on-Insulator grating coupler based on a poly-Silicon overlay*. Optics Express, 14(24):11622–11630, 2006.
- [10] F. Van Laere, T. Claes, and J. Schrauwen. *Compact focusing grating couplers for silicon-on-insulator integrated circuits*. IEEE Photonics Technology Letters, 19(23):1919–1921, 2007.

- [11] Y. Li, D. Vermeulen, Y. De Koninck, G. Yurtsever, G. Roelkens, and R. Baets. *Fiber couplers for silicon-on-insulator photonic IC's with optimized on-chip return loss*. Optical Fiber Communication Conference (OFC) 2012, page JTh2A.8, 2012.
- [12] Y. Li, D. Vermeulen, Y. De Koninck, G. Yurtsever, G. Roelkens, and R. Baets. *Compact grating couplers on silicon-on-insulator with reduced backreflection*. Optics Letters, 37(21):4356–8, November 2012.
- [13] R. Waldhäusl, B. Schnabel, P. Dannberg, E. B. Kley, A. Bräuer, and W. Karthe. *Efficient coupling into polymer waveguides by gratings*. Applied Optics, 36(36):9383–90, December 1997.
- [14] D. Vermeulen, Y. De Koninck, Y. Li, E. Lambert, W. Bogaerts, R. Baets, and G. Roelkens. *Reflectionless grating coupling for silicon-on-insulator integrated circuits*. In Group IV Photonics (GFP), 2011 8th IEEE International Conference on, volume 1, pages 74–76. IEEE, 2011.
- [15] <http://www.epxfab.eu>.
- [16] A. Ortega-Monux, L. Zavargo-Peche, A. Maese-Novo, I. Molina-Fernandez, R. Halir, J. G. Wanguemert-Perez, P. Cheben, and J. H. Schmid. *High-Performance Multimode Interference Coupler in Silicon Waveguides With Subwavelength Structures*. IEEE Photonics Technology Letters, 23(19):1406–1408, October 2011.
- [17] R. Hanfoug, L. M. Augustin, Y. Barbarin, J. J. G. M. Van Der Tol, E. A. J. M. Bente, F. Karouta, D. Rogers, Y. S. Cole, Y. S. Oei, X. J. M. Leijtens, and M. K. Smit. *A Multimode Interference coupler with low reflections*. In Proceedings Symposium IEEE/LEOS Benelux Chapter, pages 97–100, 2005.
- [18] W. Bogaerts and Y. Li. *Integrated design for integrated photonics: from the physical to the circuit level and back*. In Proc. SPIE 8781, Integrated Optics: Physics and Simulations, page 878102, Prague, Czech Republic, 2013.
- [19] E. Lambert, M. Fiers, S. Nizamov, M. Tassaert, S.G. Johnson, P. Bienstman, and W. Bogaerts. *Python Bindings for the Open Source Electromagnetic Simulator Meep*. Computing in Science & Engineering, 13(3):53–65, 2011.

4

Optical frequency shifters

In this chapter, we focus the discussion on the realization of integrated and miniaturized optical frequency shifters (OFSs) on the SOI platform. The importance of the OFS for LDV is already mentioned in Chapter 2. Briefly speaking, the OFS is used to generate a non-zero carrier frequency in the photo-current signal of the LDV, and can hence circumvent the influence of low frequency noise. The output resolution of the LDV outputs can be greatly enhanced by the use of OFSs.

In conventional heterodyne LDVs built with discrete optical components, the OFS is usually realized with an acousto-optical modulator (AOM), in which the light beam interacts with an acoustic wave to generate a frequency shift. Two important effects are required for fabricating an efficient AOM: the elasto-optic effect and the piezoelectric effect. The former one is responsible for the efficiency of the acoustic-optic interaction and the latter one is responsible for generating an acoustic wave on the material. In conventional AOM devices, LiNbO_3 is usually used. Unstrained, single-crystalline silicon has a centrosymmetric lattice structure, which does not support a piezoelectric effect. Hence it is difficult to directly generate acoustic waves on SOI. An indirect method of generating acoustic waves on SOI may be used by attaching or bonding another piezoelectric material ZnO or LiNbO_3 to the silicon layer. However, realizing such devices on SOI chips with design patterns is still not a trivial problem.

We have made efforts to realize on-chip OFSs by using the serrodyne technique, which requires only a phase modulator (PM) and a driver that can modulate the phase of light in the PM to a sawtooth profile. With the help of this serrodyne technique, an optical frequency shift can be realized on SOI using phase modu-

lators based on the thermo-optic (TO) effect, or other effects. Details about this serrodyne frequency shifter will be further explained in this chapter. Furthermore, we have also theoretically analyzed another alternative method, which takes advantage of a four-arm interferometer and can work with sinusoidal phase modulation and sinusoidal amplitude modulation. This method will be explained theoretically after the discussion of serrodyne techniques.

The following part of this chapter is organized as follows. The working principles of different types of optical modulators are firstly discussed, including the electro-optic effect, acousto-optic effect, thermo-optic effect, and plasma-dispersion effect. The serrodyne technique is then discussed and analyzed. The sideband suppressions as functions of different deviations are theoretically analyzed first, followed by a discussion of an on-chip serrodyne OFS based on the TO effect. Since the TO effect is in principle very slow, the possibility to replace it with a carrier-depletion-based serrodyne OFS is also analyzed. The four-branch interferometry frequency shift technique is theoretically discussed afterwards.

This chapter includes works collaborated with other people: the work of section 4.2.1 was aided by S. Verstuyft; the modulator in section 4.2.2 is designed by H. Yu.

4.1 Optical modulation mechanisms in PICs

An OFS is in principle an optical modulator, which only changes the frequency of the optical signal. Assuming that the electric field of light is denoted by a phasor $E_i(t)$, the phasor of the optical signal after an OFS should be $E_i(t) \exp(i2\pi f_{ofs}t)$, where f_{ofs} is the desired optical frequency shift. From another point of view, the OFS is a special phase modulator, since the intensity of the output signal is not modulated. An OFS is equivalent to a phase modulator that changes the phase of light at a constant rate in time. This view is very useful in understanding the serrodyne modulation technique, which will be explained later in this section.

Waveguide optical modulators can be categorized into phase and absorptive modulators. In the former type, the light signal is modulated by manipulating the refractive index of the guided mode, while in the latter type the absorption coefficient is controlled. Because no amplitude modulation is allowed in an ideal OFS, the phase modulators are the best choices to implement an OFS. However, it is also possible to implement an OFS using pure absorptive modulators, which will be explained later in this chapter. But this absorptive modulator based OFS introduces a certain amount of optical loss to the modulated light.

In this section, the mechanisms of different optical modulation effects used in an optical waveguide, especially in the SOI-based waveguide, are briefly discussed.

4.1.1 Electro-optic effect

The electro-optic effect describes the relation between the optical properties of a material and the driving electric field. In the optical waveguide technology, there are several electro-optic (EO) effects, among which the Pockels effect (linear electro-optic effect) and the Kerr effect (quadratic electro-optic effect) are most frequently discussed and used. Both of these effects can be used to modulate the refractive index of a material [1]. We will briefly discuss the working mechanisms of these effects and how they can be implemented on SOI substrates.

To describe EO effects, the impermeability tensor of a material $b_{i,j}$ is usually used. This tensor is used in the constitutive relation of the medium, which is expressed as

$$E_i = \frac{1}{\epsilon_0} \sum_j b_{i,j} D_j, \quad i, j = 1, 2, 3, \quad (4.1)$$

where ϵ_0 is the permittivity of free space, and E_i , D_i are the electric field and the electric displacement in the i th direction, respectively. For a homogeneous, nonmagnetic, and lossless medium, the impermeability tensor of an material can be diagonalized [1], and a principle coordinate system can be found in which the aforementioned constitutive relation (equation 4.1) can be rewritten as

$$E_i = b_i D_i / \epsilon_0, \quad i = 1, 2, 3, \quad (4.2)$$

where $b_i = b_{i,i}$. According to the relation between the field energy density U and the electric displacement D_i , it can be derived from Eq 4.2 that:

$$b_1 x_1^2 + b_2 x_2^2 + b_3 x_3^2 = 1, \quad (4.3)$$

where $x_i = D_i / \sqrt{2\epsilon_0 U}$ is the reduced displacement in each principle axis. The refractive indices n_i for each principle axis can be introduced by using $b_{i,i} = 1/n_i^2$. Equation 4.3 is also called the index ellipsoid of the medium, which is usually used to calculate the phase velocity of a light beam propagating in this medium.

When an electric field $\mathbf{E} = [E_1 \hat{x}_1, E_2 \hat{x}_2, E_3 \hat{x}_3]$ is applied across the medium, the bound charges of each atom are redistributed and the crystal lattice may also be slightly changed (inverse piezoelectric effect). The direction of the principle axes can thus be changed, indicating that the impermeability tensor of the medium in an electric field may not be a diagonal matrix anymore. As a result, the expression of the index ellipsoid in the current coordinate system has to be rewritten as

$$(b_1 + \Delta_1)x_1^2 + (b_2 + \Delta_2)x_2^2 + (b_3 + \Delta_3)x_3^2 + 2\Delta_4 x_2 x_3 + 2\Delta_5 x_1 x_3 + 2\Delta_6 x_1 x_2 = 1. \quad (4.4)$$

It can be found that the change in the impermeability tensor Δ_i ($i = 1, \dots, 6$) is directly related to the phase velocity of the light beam and thus is a good measure for the electro-optic effect.

The Pockels effect and the Kerr effect are defined by the relation between Δ_i and \mathbf{E} . For the Pockels effect, changes in Δ_i are linearly related with the applied field, which is

$$\begin{pmatrix} \Delta_1 \\ \Delta_2 \\ \Delta_3 \\ \Delta_4 \\ \Delta_5 \\ \Delta_6 \end{pmatrix} = \mathbf{R} \begin{pmatrix} E_1 \\ E_2 \\ E_3 \end{pmatrix}, \quad (4.5)$$

where \mathbf{R} is the linear electro-optic tensor. For the Kerr effect, the constants Δ_i are changed due to the quadratic electro-optic effect:

$$\begin{pmatrix} \Delta_1 \\ \Delta_2 \\ \Delta_3 \\ \Delta_4 \\ \Delta_5 \\ \Delta_6 \end{pmatrix} = \mathbf{S} \begin{pmatrix} E_1^2 \\ E_2^2 \\ E_3^2 \\ E_2 E_3 \\ E_1 E_3 \\ E_1 E_3 \end{pmatrix}, \quad (4.6)$$

where \mathbf{S} is the quadratic electro-optic tensor.

The Pockels effect is a most commonly used electro-optic effect because of its linear relation with the voltage. The commonly used materials used for Pockels effect-based EO modulators include LiNbO_3 , KD_2PO_4 and LiTaO_3 , which are, however, difficult to integrate with SOI devices. Unfortunately, the Pockels effect does not exist in crystals that have inversion symmetry, so unstrained single-crystalline silicon can not be used for applying this effect. Some special techniques, e.g. introducing strain to silicon [2], can be used to change the lattice symmetry of silicon and induce a Pockels effect. However, it is still not easy to introduce a desired strain in SOI-based devices.

Unlike the Pockels effect, the Kerr effect exists in all materials. A typical Kerr effect coefficient of silicon is $\chi^{(3)} = -9 \times 10^{-16} \text{cm}^2/\text{V}^2$ [3].

4.1.2 Acousto-optic effect

The light propagating in a material can also be modulated by acoustic waves according to the acousto-optic effect. The elasto-optic effect is the basic mechanism responsible for the acousto-optic effect. Besides the elasto-optic effect, the roto-optic effect (due to the antisymmetric rotation part of the deformation gradient) and the indirect elasto-optic effect (the result of the piezoelectric effect and electro-optic effect in succession) can also affect the modulation [1]. However, both the roto-optic effect and indirect elasto-optic effect can be neglected in most crystals which do not have a strong birefringence. According to the elasto-optical effect, an acoustic wave produces a periodic modulation of the refraction index

in the medium where the acoustic wave propagates. Consider an acoustic plane wave traveling in the x direction in the medium with velocity v_s , frequency f , and wavelength $\Lambda = v_s/f$. The strain (relative displacement) at position x and time t is

$$s_{i,j}(x, t) = S_{i,j} \cos(\Omega t - qx), \quad (4.7)$$

where $S_{i,j}$ is the amplitude, $\Omega = 2\pi f$ is the angular frequency, $q = 2\pi/\Lambda$ is the wavenumber. According to the elasto-optic effect, the strain $s_{i,j}(x, t)$ creates a perturbation in the impermeability tensor, which can be described as

$$b_{i,j}(x, t) = \sum_{k,l} p_{i,j,k,l} \cdot s_{k,l}(x, t). \quad (4.8)$$

where $p_{i,j,k,l}$ is a dimensionless coefficient known as the elastic-optic coefficient. To simplify the question, we only consider the refractive index in one direction for a linearly polarized acoustic wave with $n_1 = 1/\sqrt{b_{1,1}}$, $s_1 = s_{1,1}$ and $p_1 = p_{1,1,1,1}$, the corresponding refractive index change can thus be calculated as

$$\Delta n_1(x, t) = -\frac{1}{2} n_1^3 p_1 S_1 \cdot \cos(\Omega t - qx), \quad (4.9)$$

with a maximal phase change of $n_1^3 p_1 S_1/2$.

However, one needs to be able to generate a strain in the medium so as to create an acoustic wave, which can be calculated according to the piezoelectric constitutive equation

$$\begin{aligned} s_{i,j} &= \sum_{k,l} s_{i,j,k,l}^E t_{k,l} + \sum_k d_{i,j,k}^t E_k, \\ D_i &= \sum_{j,k} d_{i,j,k} t_{j,k} + \epsilon_i^T E_i, \end{aligned}$$

where $t_{i,j}$ is the stress tensor, $s_{i,j,k,l}$ is the compliance tensor, $d_{i,j,k}$ is the piezoelectric tensor, the superscript E indicates the value is measured for constant electric field, the superscript T indicates the value is measured for a constant stress, and the superscript t stands for the transpose of the matrix.

According to this constitutive equation, two methods can be used to induce a strain in a medium: by applying a stress or an electric field. The former method relies on Hooke's law and the latter one depends on the piezoelectricity. Similar to the Pockels effect, the piezoelectric effect also requires an asymmetry in the crystal lattice, which is not suitable for silicon. However, by applying a stress on silicon, one can also generate an acoustic wave in silicon. Simulation has shown this in which a ZnO layer is attached to the silicon layer. This ZnO layer is responsible for generating a periodic stress on the silicon layer and thus creating a surface acoustic wave [4]. However, the fabrication has not been realized due to the difficulty in realizing a nicely grown ZnO layer. It is reported in [5] that a refractive index

change of 0.5×10^{-4} can be generated in a blank Si with the help of ZnO layer, which means that a π phase shift requires a waveguide length of 1.55 cm.

The frequency of the AO modulation is determined by the bandwidth of the acoustic wave. Recently, a surface acoustic wave at 35.5 GHz has been generated on silicon with the help of a ZnO layer [6].

4.1.3 Thermo-optic effect

For an optical material, the refractive index of the material also varies as temperature changes, which is called the thermo-optic (TO) effect. According to the macroscopic Clausius-Mossotti equation [7], which works well for isotropic dielectric, the temperature dependence of a dielectric constant (proportional to the square of the refractive index) can be divided to different factors: (1) the decrease in the number of polarizable particles per unit volume combined with the increase in the polarizability of a constant number of polarizable particles, caused by the thermal expansion as temperature increases; (2) the dependence of polarizability on temperature, when keeping the volume constant. The first factor is always positive as temperature increases, while the second can be either positive or negative. It is found that the absorption due to the TO effect is very weak, thus a TO can be a very good phase modulator.

Silicon has a relatively large thermo-optic coefficient ($dn/dT=1.86 \times 10^{-4}/K$ for $\lambda = 1.55 \mu\text{m}$ [8]). For a SOI waveguide, it can be calculated that the $\Delta T_{\pi} L_{\pi} = 4.16 \text{ mm}\cdot\text{K}$. The power consumption of the TO modulator is determined by the heating efficiency and the thermal-conductivity of the chip. Providing that all heat is generated in the waveguide core region, to generate a π phase shift, the heating energy should be around 0.67 nJ. However, in most cases the heating is not that efficient.

The TO effect has a disadvantage of slow speed, which is limited by the thermal properties of the materials. The upper limit of the TO bandwidth is around MHz range [9].

4.1.4 Plasma-dispersion effect

The plasma dispersion effect is widely used nowadays for silicon modulator. By changing the free carrier density in silicon, the refractive index as well as the absorption coefficient of the guided mode can be modulated. The plasma dispersion effect can be applied to the optical mode with two methods: carrier injection and carrier depletion. The former one is usually realized with a forward-biased PIN diode, while the latter one is often implemented as a reverse-biased PN junction.

The refractive index and the absorption coefficient modulation introduced by a

plasma dispersion effect can be denoted as

$$E_1(t) = E_0(t)e^{-\frac{\Delta\alpha}{2}L \cdot 100[\text{cm/m}]} \cdot e^{i\frac{2\pi}{\lambda_0}\Delta nL}, \quad (4.10)$$

where $E_0(t)$ and $E_1(t)$ are the electric fields before and after modulation, $\Delta\alpha$ [1/cm] is the change of the absorption coefficient, and Δn is the change of refractive index. According to Soref and Bennett's work [10], Δn and $\Delta\alpha$ at the wavelength of $1.55 \mu\text{m}$ can be expressed as,

$$\Delta n = -[8.8 \times 10^{-22}\Delta N_e + 8.5 \times 10^{-18}(\Delta N_h)^{0.8}], \quad (4.11)$$

$$\Delta\alpha = 8.5 \times 10^{-18}\Delta N_e + 6.0 \times 10^{-18}\Delta N_h. \quad (4.12)$$

where ΔN_e and ΔN_h are the changes in the concentration ($1/\text{cm}^3$) of free electrons and free holes. According to these equations, the phase can be controlled by changing the concentration of the free carriers, which is usually realized with the help of a PN junction.

However, a spurious amplitude modulation combined with the refractive index modulation may introduce problems to the OFS, especially in the serrodyne technology which requires a pure phase modulator. Assuming that the carrier concentration (applied to electrons or holes) is changed from zero to $2 \times 10^{18}/\text{cm}^3$ during a modulation, a $\Delta n - \Delta\alpha$ curve can be plot. It is found that the $\Delta n - \Delta\alpha$ curves are different for electrons and holes, which is shown in figure 4.1. It is found that, in this concentration range, the loss change due to the modulation of holes is less significant than that of electrons, while the effective index change for holes is much stronger than that for electrons. Therefore, modulating the concentration of holes is more efficient than that of electrons, and it also has less spurious amplitude modulation.

Unlike the $\Delta n - \Delta\alpha$ curve for electrons, the one for holes is not linear. The refractive index change becomes slower as the carrier concentration of holes increases. This effect indicates a method to reduce the spurious amplitude modulation in a plasma dispersion based phase modulator, which will be explained as follows.

In this thesis, the strength of the spurious amplitude modulation caused by the carrier concentration variation will be characterized by the optical power change under a 2π phase modulation, since this value is closely related to the parameters used in serrodyne. Only considering the dispersion effect of electrons, the absorption change combined with a 2π phase shift is around 6.5 dB, which is independent on the carrier concentration or modulator length. However, if we consider only the effect of holes, the optical power change with 2π phase shift can be different depending on the carrier concentration or the length L_m of the modulator. The relation between the loss and the modulator length L_m can be written as

$$Loss[dB] = \frac{0.825}{L_m^{1/4}[\text{cm}]}. \quad (4.13)$$

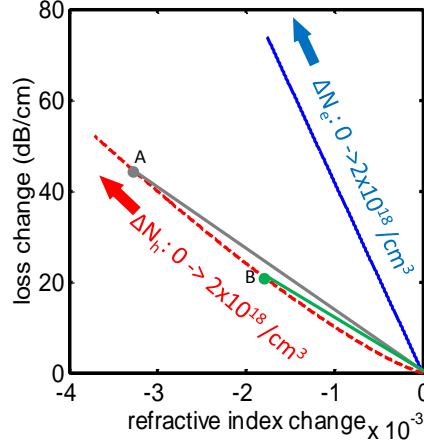


Figure 4.1: The relation between the refractive index change and the loss change (dB/cm) when the electron or hole concentration is changed from 0 to $2 \times 10^{18}/\text{cm}^3$.

This equation indicates that the longer the modulator is, the less the spurious amplitude modulation will be. The amplitude modulation is around 8.25 dB when $L_m = 1 \mu\text{m}$, and it is reduced to only 1.46 dB when $L_m = 1 \text{mm}$. Therefore if a phase modulation with less spurious amplitude modulation is needed, one can use a long phase modulator designed to be mainly controlled by concentration of holes.

The speed of a plasma dispersion effect can be fast. For a reverse-biased PN junction phase modulator, the speed is ultimately limited by the diode capacitance of the reverse-biased PN junction [11]. The speed of the reverse-biased PN junction has been reported to reach a level of 40 Gbit/s with a low power consumption. A small $L_\pi V_\pi$ value (0.62 V·cm) of this modulator is also reported [11].

4.1.5 Conclusions

As is mentioned above, it is difficult to realize an electro-optic (EO) and an acousto-optic (AO) modulator on the SOI platform, owing to the inversion symmetry of the silicon crystal lattice. The thermo-optic (TO) effect and plasma-dispersion effect can be implemented, but both have disadvantages. The TO effect is in principle slow (lower than MHz), while the plasma dispersion effect causes a spurious amplitude variation in the optical signal. In the following sections, we will analyze different OFS configurations based on these two effects.

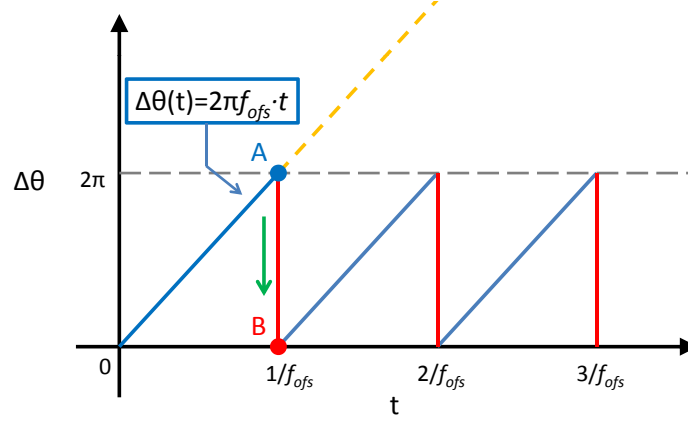


Figure 4.2: Time domain phase profile of an optical signal modulated with a serrodyne frequency shifter. In this case $\theta_{pp} = 2\pi$.

4.2 OFS based on serrodyne technique

The serrodyne modulation is an old technique for generating a pure frequency shift in radio wave signals. After the invention of laser, this technique has also been widely used in optical signals for frequency shift [12–15]. In this technique, the phase of the optical signal is modulated into a sawtooth profile as a function of time, of which the peak-to-peak phase amplitude is $\theta_{pp} = 2n\pi$, $n \in \mathbb{N}$ (see figure 4.2). If the fly-back time of the phase sawtooth, i.e. the duration from point A to point B in figure 4.2, is small enough, the receiver will not be able to resolve this time slot and still “believes” that this modulation is a linear phase change in time. Since a linear phase change $\theta(t) = k_{slope}t$ is equivalent to a constant frequency shift $\Delta f = k_{slope}/2\pi$, the sawtooth phase profile in figure 4.2 can be considered as a frequency shift of f_{ofs} .

However, under an imperfect modulation, e.g. a non-negligible fly-back time, the modulated optical signal has to be expressed as

$$E_{ofs}(t) = E_r(t) \sum_k \mu_k \exp(i2\pi k f_{ofs} t), \quad (4.14)$$

where $E_r(t)$ is the signal before the serrodyne modulation, and k is the order of the harmonic. For a perfect frequency shift, all the harmonics with $k \neq 1$ should be strongly suppressed.

As is already mentioned in Chapter 2, the harmonics that can greatly influence the LDV’s performance are the ones with $k = -1$ and $k = 0$, while the other non-fundamental orders can be filtered out in later stages. According to the analysis in Chapter 2, to limit the phase deviation of the LDV output within 0.01π , the power of the -1st order harmonic should be 30 dB lower than that of the fundamental

harmonic, and meanwhile the 0th order should also be 30 dB lower in power than the measurement reflection. Therefore we need to examine the influence of different serrrodyne deviations on these two residual harmonics.

In practice, we can not really retrieve the value of the -1st order harmonic from the power spectrum of the frequency shifted signal. Usually the power ratio between the fundamental harmonic and the combined -2nd and 2nd order harmonics (denoted as ς) is used as the figure of merit for characterizing the optical frequency shift. Thus it is important to know both the amplitude attenuations and the phase relations of -2nd and 2nd order harmonics.

For a serrrodyne modulator, several problems may occur, and they are described as follows.

- The peak-to-peak phase shift θ_{pp} may not be accurate enough.
- The fly-back time of the sawtooth may not be small enough due to the limited bandwidth of the phase modulator or the driver.
- The ramp of the sawtooth may not be linear.
- A spurious amplitude modulation of the optical signal may coexist with the phase modulation.

These deviations will be discussed in the following sections, with several simulation results. In the simulation, the sidebands are calculated according to

$$a_n = \frac{1}{T} \int_0^T E_{ofs}(t) e^{-\frac{2\pi n}{T} t} dt. \quad (4.15)$$

1. Peak-to-peak phase shift

It is important to ensure a $2n\pi$ phase amplitude in the sawtooth profile. However, it is not easy to find the exact driving signal for such a phase amplitude. When the applied driving signal is slightly smaller or larger than the desired phase amplitude, some other harmonics can be excited and influence the LDV output.

The power spectral densities of several important harmonic orders are simulated and plotted in figure 4.3(a) and figure 4.3(b) as functions of the peak-to-peak phase amplitude θ_{pp} . It is found that, if θ_{pp} is set to 2π , the fundamental harmonic has the maximal power density value while the other harmonic orders are strongly suppressed. The power will be redistributed from the fundamental harmonic to the second-order harmonic as θ_{pp} shifts from 2π to 4π , since the phase slope in the sawtooth ramp is doubled after this change. According to these simulated results, to ensure that the power of the -1st order harmonic is at least 30 dB lower than that in the fundamental harmonic (so that the phase deviation in the LDV output is smaller than

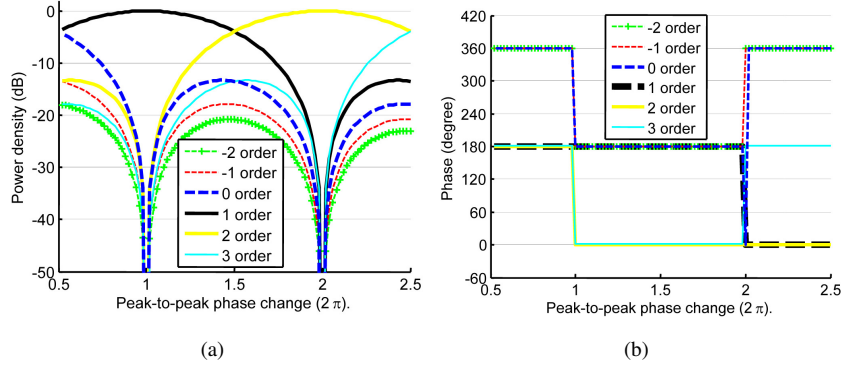


Figure 4.3: Different harmonic orders (simulated) as functions of the peak-to-peak phase change: (a) power (b) phase.

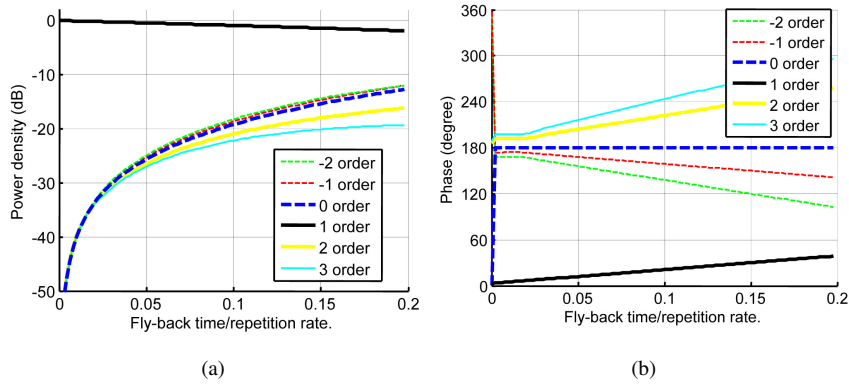


Figure 4.4: Different harmonic orders (simulated) as functions of the fly-back time: (a) power, (b) phase.

0.01π), the relation $|\theta_{pp} - 2\pi|/(2\pi) < 5\%$ has to be realized. Besides, it is found that the phases between the -2nd and 2nd order harmonics are always 180° out of phase when θ_{pp} is around 2π , which indicates that ζ is slightly larger than the actual power ratio between the fundamental harmonic and the 2nd order harmonic.

2. Finite fly-back time

The fly-back time of the sawtooth is crucial to the serrrodyne modulation since it can easily influence the optical frequency shift. The influence of a finite fly-back time on the serrrodyne frequency shift has been analyzed by

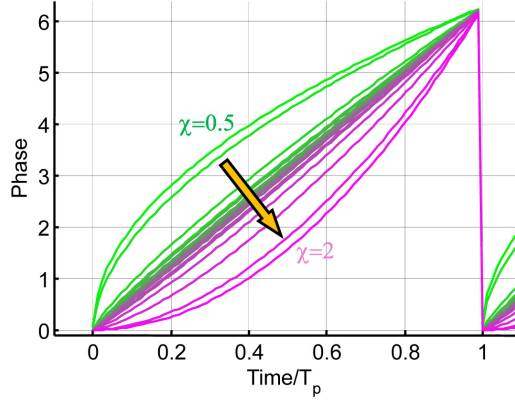


Figure 4.5: Several nonlinear ramp signal, with $\chi = 0.5, \dots, 2$.

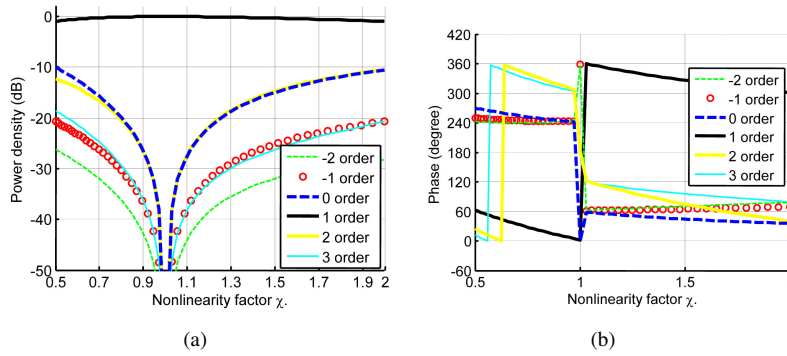


Figure 4.6: Different harmonic orders (simulated) as functions of nonlinearity factor χ : (a) power, (b) phase.

Johnson *et al.* [13]. The calculation is repeated and shown in figure 4.4(a) and figure 4.4(b). To ensure that the power ratio of the -1st order harmonic to the fundamental harmonic is lower than -30 dB, the fly-back time should not be larger than 3% of the sawtooth repetition rate. From the phase curves it is seen that the phases between the -2nd and 2nd order harmonics are approximately in phase. So that ζ is slightly smaller than the power ratio between the fundamental harmonic and the 2nd order harmonic.

3. Nonlinearity

For some phase modulators, the phase change is not linear to the applied electric field, e.g. the phase of a thermo-optic modulator is proportional to the square of the applied voltage. Therefore, sidebands can be excited.

The nonlinearity of the sawtooth ramp is described for the first period as

$$\theta(t) = 2\pi\left(\frac{t}{T_p}\right)^\chi, 0 < t < T_p, \quad (4.16)$$

where T_p is the period of the sawtooth signal, and χ is the nonlinearity factor. The signal profiles are shown in figure 4.5. The sideband suppressions of harmonics are simulated and shown in figure 4.6(a) and figure 4.6(b). It is found that in order to suppress the -1st order down to -30dB, the nonlinearity factor χ should fulfill $0.8 < \chi < 1.2$.

4. Amplitude modulation

For some modulators, e.g. carrier-depletion type phase modulators, the serrodyne modulation suffers from a spurious amplitude modulation. Though this amplitude modulation can be complex, we only consider a linear spurious amplitude modulation, being described by

$$E'_r(t) = E_r(0)\left(1 + \frac{\alpha_{2\pi}t}{T_p}\right) \exp\left[i\frac{2\pi t}{T_p}\right], 0 < t < T_p, \quad (4.17)$$

where $\alpha_{2\pi}$ indicates the extra amplitude modulation after the phase is modulated by 2π . The simulated results are shown in figure 4.7(a) and figure 4.7(b). To ensure the -1st order harmonic is 30 dB lower than the fundamental order, the spurious amplitude modulation ($20 \log(1 + \alpha_{2\pi})$) should be smaller than 4 dB. Note that these curves are symmetric and centered on 0 dB amplitude modulation, so only the positive modulation values are plotted.

The aforementioned four effects may coexist in the output signals, but the total effect may not be a simple addition of these four results. We suggest fulfilling all these four requirements simultaneously to ensure a good function of the LDV. Additionally, these deviations may be compensated with the mentioned algorithms in Chapter 2. However, since those compensation methods require a certain calculation time, therefore they limit the bandwidth of the LDV. Noise also deteriorates those demodulations.

4.2.1 Serrodyne OFS based on the thermo-optic effect

In this section, we demonstrate a serrodyne modulator integrated SOI using the thermo-optic (TO) effect. The cross-section of the TO modulator is shown in figure 4.8. In this modulator, the temperature of the waveguide is controlled by a metal heater on top.

The heater is a 2.25 μm wide (W_{Ti}), 320 nm thick (H_{Ti}) titanium (Ti) wire, which is fabricated on top of the waveguide with a liftoff process. However, since

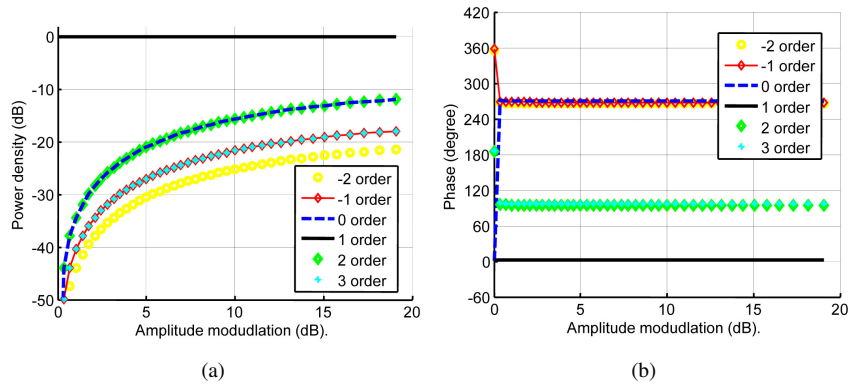


Figure 4.7: Different harmonic orders as functions of spurious amplitude modulation: (a) power, (b) phase. In these figures, the spurious amplitude modulation is denoted as $20 \log(1 + \alpha_{2\pi})$.

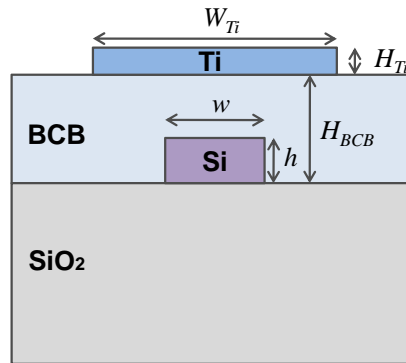


Figure 4.8: The cross section of the thermo-optic frequency modulator.

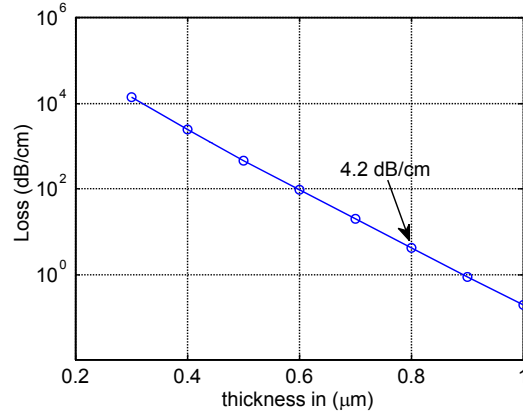


Figure 4.9: Optical loss due to the metal heater for different BCB thicknesses.

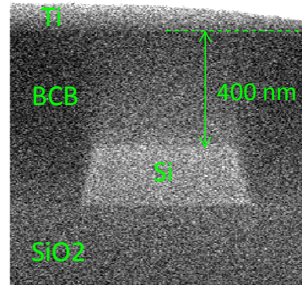


Figure 4.10: The SEM image of a thermo-optic modulator.

light can be absorbed by metals, a Benzocyclobutene (BCB) layer is inserted between the waveguide and the metal to avoid a significant optical absorption. The absorption of light due to the existence of the heater as a function of the BCB thickness H_{BCB} is simulated using a software package COMSOL-Multiphysics based on the finite element method (FEM). The results are shown in figure 4.9. According to the simulation results, to keep the absorption loss lower than 4.2 dB/cm, the thickness of the BCB should be larger than 800 nm. However, in our fabricated device, the thickness of the BCB H_{BCB} is estimated to be around 620 nm, which is shown in figure 4.10. The optical loss in this heater is around 3 dB for a length of 750 μm according to measurement results.

The speed of this modulator is limited by the thermal properties of the materials, especially the BCB and silica with small thermal conductivities. The response speed of this kind of TO modulator is also simulated with COMSOL. In the simulation, a sinusoidal thermal signal with an average power of $3.75 \times 10^{14} \text{ W/m}^3$ is

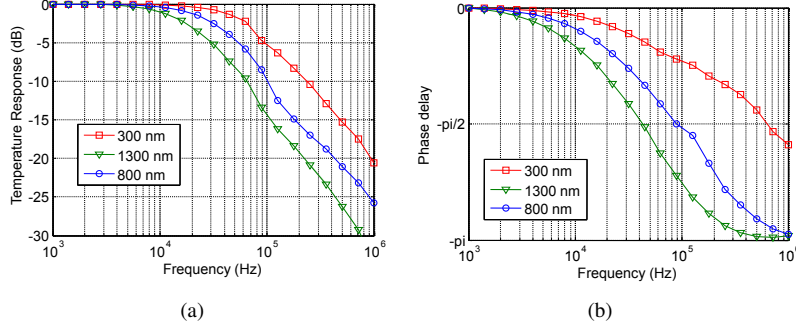


Figure 4.11: 4.11(a): The temperature response ($\frac{\Delta T_{pp}(f)}{\Delta T_{pp}(0)}$) for three TO modulators with different BCB thickness, where $\Delta T_{pp}(f)$ is the peak-to-peak temperature variation at frequency f . 4.11(b): The phase delay for three TO modulators with different BCB thickness

applied in the heater. A temperature monitor is set in the center of the waveguide to track the temperature variation for different frequency. It can be found that the temperature modulation becomes weaker as the frequency increases (see figure 4.11). From this figure, it can also be seen that the thinner the BCB is, the faster the heater works. The 3 dB bandwidths of these modulators (BCB thickness: 1300 nm, 800 nm, and 300 nm) are 19 kHz, 35 kHz, and 70 kHz, respectively.

In the real design, the length of the heater is set to be $750 \mu\text{m}$. Measurements show that the resistance of this heater $R = 1.0 \text{ k}\Omega$. In order to characterize the function of this TO modulator, the TO modulator is set in one arm of a Mach-Zehnder interferometer (MZI). Thus the phase modulation can be converted to an intensity modulation and can thus be monitored. Both the splitter and the combiner of the MZI are realized with 3 dB MMI couplers to ensure that the optical powers in these two arms are balanced. During the measurement, light at a wavelength of 1550 nm is generated from a temperature controlled DFB laser and is sent to the MZI with the TO modulator. A power meter is used to detect the modulated optical power at the MZI output. The signal is recorded with the help of a data acquisition card (NI USB-6218) working at the sampling frequency of 100 ksp/s.

The TO modulator is controlled by a function generator. A time-varying voltage is applied across the heater to change the temperature of the underlying waveguide and hence modulating its effective index. According to the relation between the driving voltage $V(t)$ and the induced thermal power $P(t)$, i.e. $P(t) = V^2(t)/R$, a voltage with a square-root-of-time profile

$$V(t) = V_{pp} \sqrt{t f_{ofs} - \text{floor}(t f_{ofs})} \quad (4.18)$$

was applied across the heater, where the function $\text{floor}(x)$ returns the largest inte-

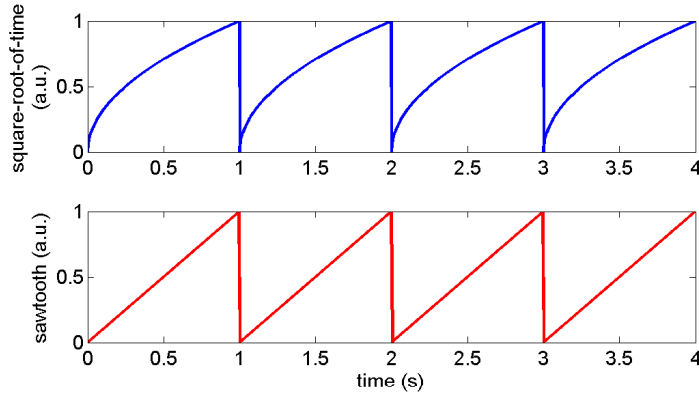


Figure 4.12: An example of the square-root-of-time (SQOT) and sawtooth signals with a frequency at 1 Hz. When the voltage signal applied across the heater has a SQOT profile, the phase profile of the optical signal should be a sawtooth.

ger not greater than x . The driving voltage and the corresponding phase change of the TO modulator are shown in figure 4.12. Here, the repetitive sawtooth signal has a frequency of 1 kHz.

The peak-to-peak voltage of the driving signal corresponding to a 2π phase change in the underlying optical mode is denoted as $V_{2\pi}$. This value has to be determined by the optical power of the MZI output. Since for each period the phase of the optical mode is linearly changed, a sinusoidal optical power can be obtained from the power meter. If the $V_{pp} \neq nV_{2\pi}$, a clear jump can be found in the optical power. By adjusting V_{pp} , an optimal situation can be reached in which the MZI output power has no apparent jump. The corresponding voltage should be just around $V_{2\pi}$. According to measurement results, our best device has a $V_{2\pi} = 3.75$ V. Considering the resistance of the heater, the average input power of this design is around 7 mW. This may not be the optimum power since the heater and the underlying waveguide are not well aligned. The photocurrent signals corresponding to the optical power of the MZI output is shown in figure 4.13. Its power spectral density is shown in figure 4.14.

From figure 4.14, it is seen that the second-order harmonic (combined with the -2nd harmonic) is 39 dB weaker than the fundamental harmonic frequency. Assuming that the fly-back time (limited by thermal time constants) is the main cause of the higher order harmonics, this result reveals that the fly-back time is less than $20 \mu\text{s}$ according to calculation.

The serrodyne bandwidth is measured with another TO phase modulator. The power spectral densities of the fundamental harmonic and the 2nd order harmonic are measured as functions of the sawtooth repetition rate. For each measurement,

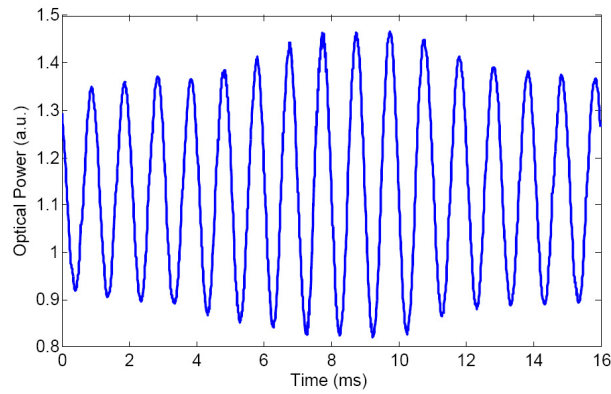


Figure 4.13: Optical power measured from the analog output of the powermeter as a function of time. An optimized thermo-optic serrrodyne modulation (at 1 kHz) is applied to the reference arm. The measurement arm is connected with a fiber, but without any intended frequency shifted.

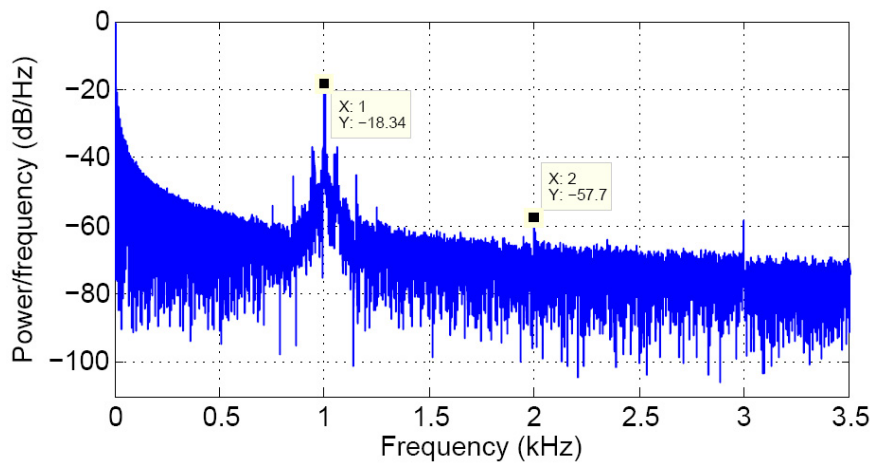


Figure 4.14: Power spectral density of the signal from the analog output. An optimized thermo-optic serrrodyne modulation (at 1 kHz) is applied to the reference arm. The measurement arm is connected with a fiber, but without any intended frequency shifted.

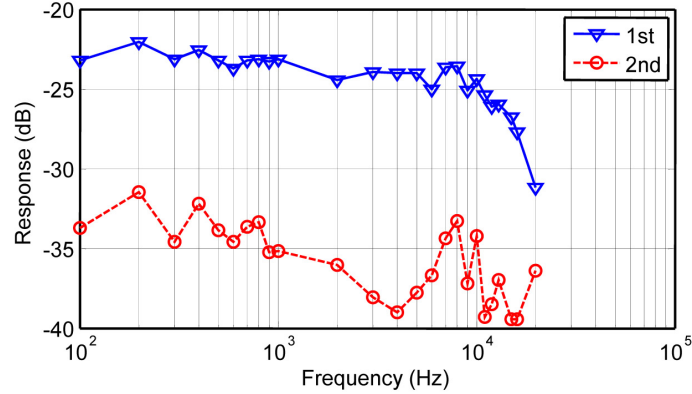


Figure 4.15: The amplitude of the fundamental harmonic and 2nd order harmonic as functions of the sawtooth repetition frequency.

we make sure that $V_{pp} = V_{2\pi}$ is realized. The measurement results are shown in the figure 4.15. From this figure it is found that the 3-dB bandwidth of the TO-based serrodyne OFS is around 10 kHz.

With this TO modulator, a serrodyne optical frequency shift of several kilohertz can be generated. This is good for some applications measuring small vibrations, with the maximal velocity of around several millimeters per second. This serrodyne modulator has a power of several milliwatts, this is not very small but can be acceptable for some applications.

4.2.2 Serrodyne OFS based on reverse biased PN junction

As is aforementioned, a plasma dispersion effect can be used to modulate the phase of light. The practical method is to inject carriers into the optical waveguide, or to deplete the carriers out of the waveguide. This is possible by implementing a PN junction in an optical waveguide, and changing the size of the depletion region with a changing voltage. The carrier injection can be realized by applying forward bias the PN junction, while the carrier depletion is implemented with a reversed bias. The forward biased PN junction is more efficient, but is not very fast and is combined with a strong thermo-optic effect, which counteracts with the plasma dispersion effect in the direction of phase shift. Therefore, the reverse biased PN junction is more suitable for the serrodyne modulation.

The cross-section of the PN junction is shown in figure 4.16. By doping in the waveguide region, a depletion area can be formed in the center of the waveguide, where most of the light power is concentrated. When a reverse biased electrical field is applied to this PN junction, the size of the depletion region can be changed, indicating that the total carriers in the waveguide region is modulated.

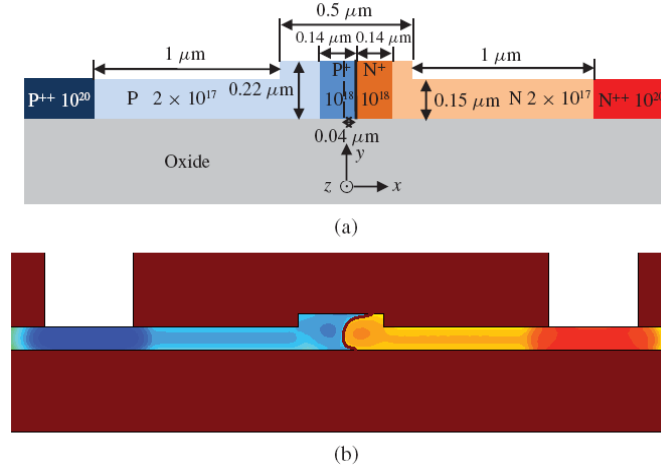


Figure 4.16: (a) Schematic cross section of an ideal abrupt p-n junction-based optical phase shifter. (b) A practical dopant distribution achieved by the implantation condition. Reproduced from [16]

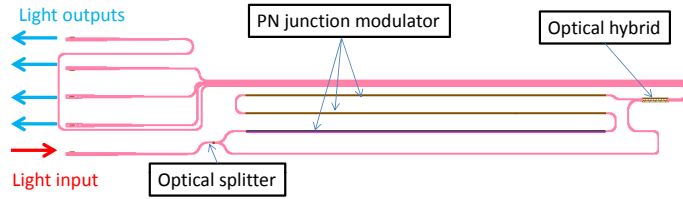


Figure 4.17: The test structure of a PN diode based phase modulator. The actual modulator is split into three parts with each has a length of 1.5 mm.

In order to generate a 2π phase shift with our function generator, we use a long ($L_m = 4.5$ mm) modulator with PN junction to modulate the phase of the guided light. To avoid a very long structure, the phase modulator is folded into three parts. The schematic of the design is shown in figure 4.17. In this figure it is seen that the phase modulator is set in one arm of an MZI, in which a 2×4 MMI coupler is used as the optical combiner. A Lissajous trace of two outputs signals, which are 90° out of phase, can be generated. With the help of this 2×4 MMI, we can easily tell the direction of the phase change and the corresponding change in amplitude.

The IV-curve of the reverse biased PN junction is shown in figure 4.18. It can be found that the break-down voltage is at around 15 V, which is large. A 2π phase shift can be realized before the voltage reaches breakdown.

Measurement results show that $V_{2\pi}$ of this modulator is around 13.6 V, which corresponds an $V_\pi L_\pi$ value of 3.06 V-cm. This PN modulator is driven by a saw-

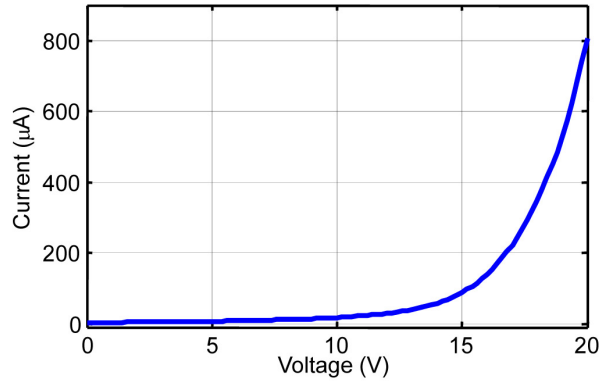


Figure 4.18: The current-voltage curve of the reverse biased PN junction.

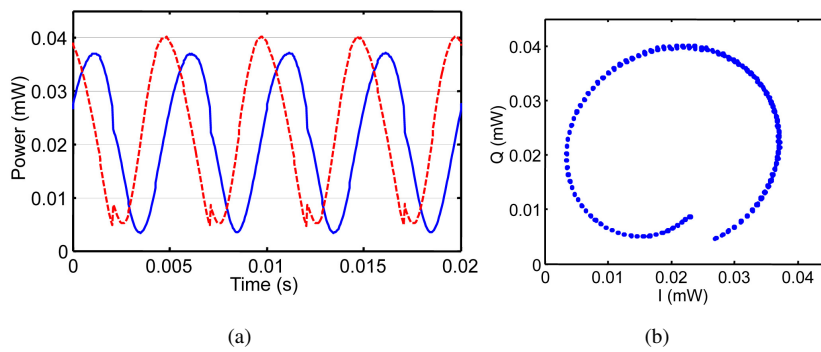


Figure 4.19: (a) The optical power of two outputs ports of the optical hybrid for a reverse biased PN junction, when a 2π peak-to-peak phase shift is generated in the PN phase modulator by a sawtooth voltage driving signal. (b) The Lissajous curve of the two outputs.

tooth voltage with the desired peak-to-peak value $V_{2\pi}$. The optical signals at the two output ports (in quadrature) are shown in figure 4.19(a), and the Lissajous curve formed by these two signals is shown in figure 4.19(b). From figure 4.19(b) we can find that a 2π phase shift can be realized, but the intensity has a variation of about 2-3 dB, which corresponds to a 4-6 dB absorption modulation in the reference optical signal. The average loss of the modulator can also be estimated to be around 6 dB by calculating the modulation depths of the outputs. The power spectral densities of these two signals (see figure 4.20) show that the second order is suppressed by around 23 dB relative to the fundamental harmonic.

The bandwidth of this modulator is high enough for generating a high frequency OFS [11], which will improve the velocity limit of a heterodyne LDV. However, the influence of the high-order harmonics brought by the spurious am-

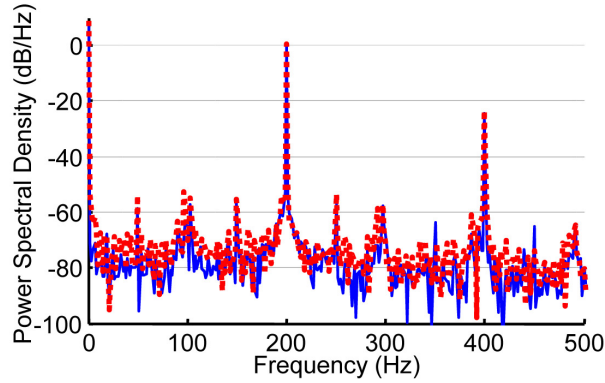


Figure 4.20: The power spectral densities of the two quadratic signals for a reverse biased PN junction.

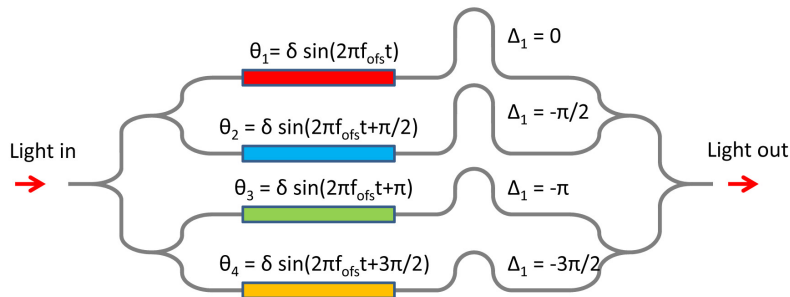


Figure 4.21: The schematic of a four-branch interferometry used for frequency shifting.

plitude modulation may deteriorate the LDV outputs. The distortions may be compensated with certain demodulation algorithms in DSP. However, influence of noise and requirement of high data acquisition speed limit the use of the DSP compensation.

Therefore it is important to reduce the spurious amplitude modulation in the PN phase modulator. From the view of the design, the PN modulators can be designed in such a way that n-type carriers dominate the modulation effect, so that the spurious amplitude modulation can be decreased by increasing the modulator length (see previous sections in this chapter). However, the required length normally is very long, which limits the miniaturization of LDV and may also introduce a significant loss in the reference arm.

4.3 Four-branch interferometry frequency shifter

The problems of serrodyne optical frequency shift hinder the realization of a high speed optical frequency shifter. To conquer this problem, a method based on sinusoidal phase modulations is introduced. This method is similar to the four-branch waveguide interferometer based single-side band (SSB) optical modulator with the help of a surface-acoustic-wave (SAW) [4]. In the analysis of a SAW-based SSB optical modulator, the spurious amplitude modulation is not considered. However, the spurious amplitude modulation is not avoidable in the fast reversed PN-junction phase modulation, their influence to this four-branch interferometry will be analyzed in this section.

4.3.1 Four-branch method with pure phase modulation

A sinusoidal phase modulation in the phase of the reference signal is described as

$$E_1(t) = E_0(t)e^{i\delta \sin(2\pi f_{ofst})}, \quad (4.19)$$

where δ is the modulation depth of the phase. The right side of this equation can be expanded as

$$e^{i\delta \sin(2\pi f_{ofst})} = \sum_{k=-\infty}^{\infty} J_k(\delta) e^{i2k\pi f_{ofst}}, \quad (4.20)$$

where $J_n(\delta)$ is the Bessel function of the first kind. This expansion indicates that the sidebands can not be neglected. However, many of these influential sidebands can be removed with the help of a four-branch interferometer is studied.

The schematic of a four-branch interferometer is shown in figure 4.21. In each arm, the phase of the signal $E_{0,n}(t) = E_0/2$, $n = 0, 1, 2, 3$ is sinusoidally modulated to $\delta \sin(2\pi f_{ofst} + n\pi/2)$, followed by a phase delay of $-n\pi/2$. Therefore, the modulated signals become

$$E_{1,n}(t) = \frac{E_0(t)}{2} e^{i[\delta \sin(2\pi f_{ofst} + n\pi/2) - n\pi/2]} \quad (4.21)$$

$$= \frac{E_0(t)}{2} \sum_{k=-\infty}^{\infty} J_k(\delta) e^{i[2k\pi f_{ofst} + (k-1)n\pi/2]} \quad (4.22)$$

$$= \frac{E_0(t)}{2} \sum_{k=-\infty}^{\infty} J_k(\delta) i^{(k-1)n} e^{i[2k\pi f_{ofst}]} \quad (4.23)$$

Only considering a certain k value, the combination of the four signals are

$$E_1^k(t) = \xi_k \sum_n i^{(k-1)n}, \quad n = 0, 1, 2, 3, \quad (4.24)$$

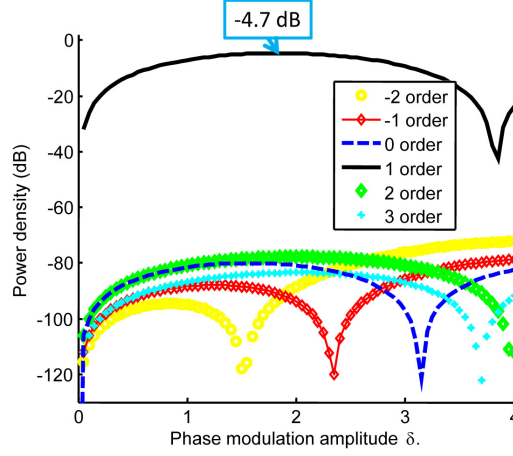


Figure 4.22: The power spectral densities of different harmonics using the four-branch interference OFS with different phase amplitude δ .

where $\xi_k = E_0(t)J_k(\delta)e^{i2k\pi f_{ofs}t}/4$. We can find that the value of $\sum_n i^{(k-1)n}$ ($n = 0, 1, 2, 3$) equals zero when $k = -2, -1, 0, 2, 3$, and equals 4 when $k = 1$ and -3 . Therefore, the most influential harmonics, i.e. $k = -1$ and 0 , are strongly suppressed. The calculated power spectral densities of these sidebands are simulated and shown in figure 4.22. From this figure, it can be seen that the sideband suppression is very strong. Besides, the optical loss of the fundamental harmonic is minimum when $\delta = 1.84$.

4.3.2 Four-branch method with pure amplitude modulation

Now consider a pure amplitude modulation, which reforms the combined signal of the four-branch interferometry

$$E_{1,n}(t) = \frac{E_0(t)}{4} [1 + \delta_a \sin(2\pi f_{ofs}t + n\pi/2)] e^{-in\pi/2} \quad (4.25)$$

$$= \frac{E_0(t)}{8} \{2e^{-in\pi/2} + \delta_a [e^{i2\pi f_{ofs}t} - e^{-i(2\pi f_{ofs}t + n\pi)}]\}, \quad (4.26)$$

where δ_a is the amplitude modulation depth. This signal can be considered as a combination of the original signal and two frequency shifts, i.e. f_{ofs} and $-f_{ofs}$. However, it can be found that the $-f_{ofs}$ part and the unshifted part are canceled out by combining the four signals ($n = 0, 1, 2, 3$), while the f_{ofs} part is enhanced after the combination. This indicates that a high quality frequency shift is generated.

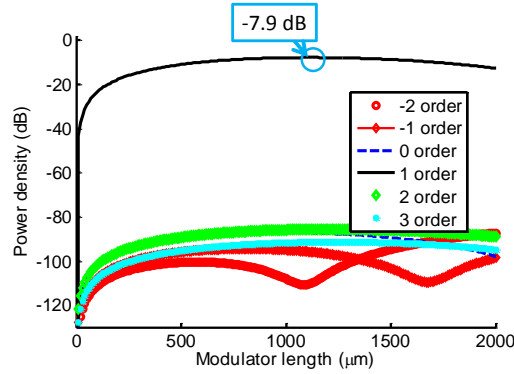


Figure 4.23: Power spectral densities of different harmonics as functions of modulator length when the carrier concentration of holes is modulated by a sinusoidal signal with an amplitude of $2 \times 10^{17}/\text{cm}$

4.3.3 Four-branch method for reversed PN modulators

In a phase modulator based on reversed PN junctions, spurious amplitude modulation can also be found in the output signal. It is interesting to know whether the four-branch technique can be applied to this type of modulator for generating OFS. In this section, we will theoretically analyse this problem by using Eq. 4.11 and Eq. 4.12. In the simulation, we consider only the plasma dispersion effect of holes, since holes are more efficient than electrons in the sense of phase modulation according to figure 4.1. It is assumed that the background hole concentration is $1 \times 10^{18}/\text{cm}$. A sinusoidal signal modulates the carrier concentration with an amplitude of $2 \times 10^{17}/\text{cm}$. The power of each harmonic is shown in figure 4.23. It is found that the maximal power of the fundamental harmonic is -7.9 dB lower than that of the input signal when $L_m \simeq 1100 \mu\text{m}$. This situation corresponds to a phase modulation of with the half phase amplitude $\delta = 1.53$, which is smaller than the value for four-branch method with pure phase modulation. When L_m is decreased to $500 \mu\text{m}$ (corresponding a total modulator length of 2 mm), the total modulator loss becomes 11 dB. Despite of this optical loss, the four-branch interferometry frequency shifter has shown several advantages over the serrodyne approach. Firstly, according to simulation, the sideband suppression ratio is very high (over 70 dB). Secondly, the modulator bandwidth is strongly reduced compared to the sawtooth signal.

According to the above analysis, the four-branch interferometry frequency shifter shows promising results with significantly reduced the sideband harmonics and modulator bandwidth. However, there are still some problems with this OFS. For example, the phase relations and power balance among these four arms

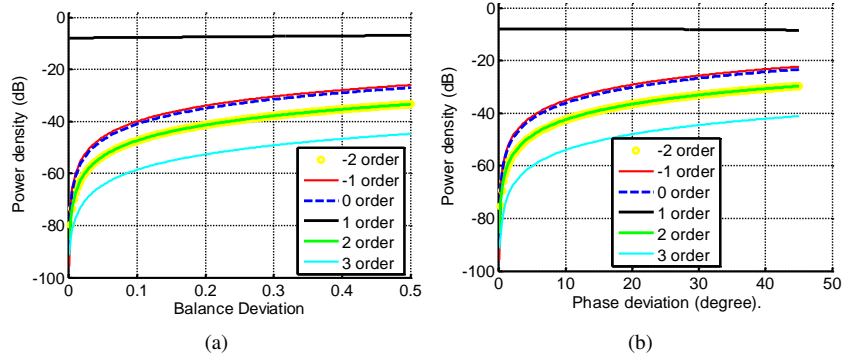


Figure 4.24: The power spectral densities of different harmonics using the four-branch interference OFS (a) as functions of the amplitude deviation ζ in one arm, indicating that the light amplitude in one arm is increased by $1 + \zeta$ times, when the half phase amplitude $\delta = 1.53$. (b) as functions of the phase deviations ξ in arm arm, indicating that in one arm the phase is increased by ξ degree.

are quite important to the performance of this OFS. Several simulations have been done with an assumption that the signal in one arm is deviated (see figure 4.24(a) and figure 4.24(b)). These results conclude that the balance deviation should be less than 20% and phase deviation should not go beyond 10° , so that the power of the -1st order harmonic is 30 dB lower than that of the fundamental order. In practice, all arms may be deviated, which makes the situation more complex. To solve this problem, the signal at each arm may be controlled by implementing phase and amplitude compensation modulators.

4.4 Conclusions

In this chapter, we have mainly focused on the realization of an optical frequency shifter on the SOI platform. It turned out that both the thermo-optic (TO) effect and the plasma dispersion effect can be good candidates for the serrodyne-based optical frequency shift. However, both effects have their drawbacks. The TO effect is slow, while the plasma dispersion effect has a significant spurious amplitude modulation in the optical signal.

To conquer the aforementioned problems in the serrodyne technique, we have analyzed an alternative method, the four-branch interferometry frequency shifter. With this method, we can implement a very fast OFS with strongly suppressed problematic sidebands. Simulations show that this method can be influenced by unbalanced power ratio and phase deviations in the four-branch interferometer, but these influences can be well compensated with auxiliary phase and amplitude

controllers.

References

- [1] M. Bass, E. W. Van Stryland, D. R. Williams, and W. L. Wolfe, editors. *Handbook of Optics, Volume II - Devices, Measurements, and Properties*. McGraw-Hill, 2 edition, 1995.
- [2] R. S. Jacobsen, K. N. Andersen, P. I. Borel, J. Fage-pedersen, L. H. Frandsen, O. Hansen, M. Kristensen, A. V. Lavrinenko, G. Moulin, H. Ou, C. Peucheret, and A. Bjarklev. *Strained silicon as a new electro-optic material*. *Nature*, 441(May):199–202, 2006.
- [3] Y Zheng, editor. *Wave Propagation Theories and Applications*. InTech, 2013.
- [4] E. C. S. Barretto. *Integrated Ultrasonic-Photonic Devices*. PhD thesis, Technical University of Denmark, 2011.
- [5] E. Bonnotte, C. Gorecki, H. Toshiyoshi, H. Kawakatsu, H. Fujita, K. Worhoff, and K. Hashimoto. *Guided-wave acoustooptic interaction with phase modulation in a ZnO thin-film transducer on an Si-based integrated Mach-Zehnder interferometer*. *Journal of Lightwave Technology*, 17:35–42, 1999.
- [6] S. Büyükköse, B. Vratzov, J. van der Veen, P. V. Santos, and W. G. van der Wiel. *Ultrahigh-frequency surface acoustic wave generation for acoustic charge transport in silicon*. *Applied Physics Letters*, 102:013112, 2013.
- [7] A. J. Bosman and E. E. Havinga. *Temperature dependence of dielectric constants of cubic ionic compounds*. *Physical Review*, 253(1961), 1963.
- [8] J. R. Meyer, M. R. Kruer, and F. J. Bartoli. *Optical heating in semiconductors: Laser damage in Ge, Si, InSb, and GaAs*. *Journal of Applied Physics*, 75(May), 1980.
- [9] M. Iodice, F. G. Della Corte, I. Rendina, and P. M. Sarro. *Transient analysis of a high-speed thermo-optic modulator integrated in an all-silicon waveguide*. *Optical Engineering*, 42(1):169–175, 2003.
- [10] R. Soref and B. Bennett. *IEEE Journal of Quantum Electronics*, 23(1):123–129, January 1987.
- [11] H. Yu, M. Pantouvaki, J. Van Campenhout, Di. Korn, K. Komorowska, P. Dumon, Y. Li, P. Verheyen, P. Absil, L. Alloatti, D. Hillerkuss, J. Leuthold, R. Baets, and W. Bogaerts. *Performance tradeoff between lateral and interdigitated doping patterns for high speed carrier-depletion based silicon modulators*. *Optics Express*, 20(12):12926–38, June 2012.

-
- [12] K. K. Wong, R. M. De La Rue, and S. Wright. *Electro-optic-waveguide frequency translator in LiNbO₃ fabricated by proton exchange*. Optics Letters, 7(11):546–8, November 1982.
- [13] L. M. Johnson. *Serrodyne optical frequency translation with high sideband suppression*. Journal of Lightwave Technology, 6(1), 1988.
- [14] P. A. S. Jorge, L. A. Ferreira, and J. L. Santos. *Analysis of the flyback effects on the serrodyne interferometric demodulation of fiber optic Bragg grating sensors*. Optical Engineering, 39(5):1399, 2000.
- [15] D. M. S. Johnson, J. M. Hogan, S. W. Chiow, and M. a. Kasevich. *Broadband Optical Serrodyne Frequency Shifting*. Optics Express, 17(21):3, September 2009.
- [16] H. Yu, W. Bogaerts, and A. De Keersgieter. *Optimization of ion implantation condition for depletion-type silicon optical modulators*. IEEE Journal of Quantum Electronics, 46(12):1763–1768, 2010.

5

Heterodyne and homodyne LDVs on SOI: measurement results

This chapter focuses on the realization of the PIC-based LDV designs in a CMOS-compatible SOI platform. The device fabrication is realized with the 193 nm deep ultra-violet lithography through ePIXfab [1], a multi-project wafer shuttle for SOI-based PIC designs. Two major types of LDVs are fabricated and examined: heterodyne and homodyne. As is already mentioned above, both the heterodyne and homodyne LDVs have their advantages and disadvantages. In this chapter, we will compare the theoretical predictions of these designs with the measurement results of the corresponding fabricated devices, and then give some suggestions to further improve the designs.

This chapter is organized as follows. Firstly, the general measurement setup used to characterize the on-chip LDV is described. Then the focus will be moved to the heterodyne LDV using the serrodyne optical frequency shift technique. For heterodyne LDVs, the proof-of-principle measurement is firstly demonstrated in an optical fiber system, and then an integrated version assisted with a thermo-optic (TO) based Serrodyne OFS is characterized and analyzed. After the discussion of heterodyne LDVs, we will report the realization of a homodyne type on-chip LDV using the quadrature demodulation technique. Conclusions will be drawn in the last part of this chapter.

This chapter includes works collaborated with other people: the work of section 5.1 is aided by J. Schrauwen, G. Yurtsever, G. Peter, and H. Shen; the work of section 5.2.1 was mainly done by S. Meersman, and was also received help from



Figure 5.1: The picture of a fiber array from OZ-optics. Reproduced from [4].

J. Allaert and S. Verstuylt; the work of section 5.2.2 is aided by S. Verstuylt.

5.1 Measurement setups

Lasers and photo-detectors (PDs) are the necessary parts of an LDV system. Nowadays, new technologies have been developed to integrate lasers and PDs on the SOI substrate [2, 3]. However, the corresponding fabrication processes include several complex steps, which reduce the yield of working devices. Besides, the existence of the integrated lasers and PDs may also conceal the impacts of other influential factors, e.g. on-chip spurious reflections. To simplify the LDV system, we will solely test the on-chip designs without integrating lasers and PDs in this thesis, by using external laser sources and PDs. The influence of integrated lasers and PDs will be studied in future research.

In order to connect external devices with the PIC designs, a fiber array (FA) is used as a connector in our setup. An FA normally consists of a V-grooved silicon substrate, multiple single-mode fibers and a cover (see figure 5.1), and it supports the transmission of multiple optical signals. The pitch between two adjacent fibers in an FA is normally chosen as $127 \mu\text{m}$ or $250 \mu\text{m}$. In order to optically connect the FA with the PIC, the grating couplers in the PIC are also evenly spaced in a line. The value of their pitch is set the same as that of the FA. The same pitch as the FA. The polish angle of the FA is another important parameter, and it has to be accustomed to the direction of the out-coupled light from the grating couplers, which is normally set to be $\phi = 8^\circ$ or 10° to avoid strong second order on-chip reflections.

The alignment process of the FA to the GC array in the PIC is not as simple as that of a single-mode fiber. On the contrary, it requires the use of a six-dimension positioning stage. A schematic of the setup and the corresponding photo are shown in figure 5.2(a) and figure 5.2(b), respectively. The alignment normally takes several steps:

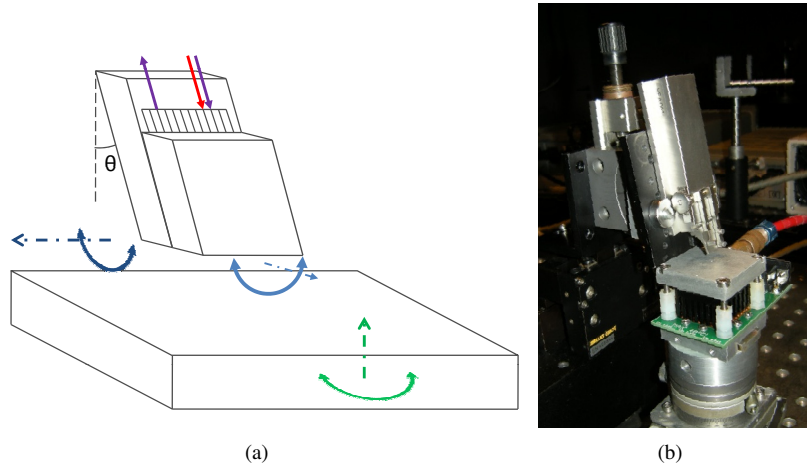


Figure 5.2: (a) The schematic of a fiber array setup. (b) The photo of the fiber array setup.

1. Make the end facet of the FA parallel to the chip surface;
2. Make the direction of the FA parallel to that of the GC array, by adjusting the azimuth of the chip;
3. Adjust the position of the FA with the help of a visible light (cannot be coupled to the waveguide) when the FA is kept a distance from the chip surface. So that the red spot from the FA is seen by the camera.
4. Send infrared light to the alignment waveguide (see in figure 5.3) and adjust the position of the FA and the polarization state of the input light, so that a strong output from the designed output port can be detected.
5. Gradually reduce the distance between of the FA and the PIC while keeping the best alignment till this distance is smaller than $100 \mu\text{m}$. After this step, the gap between the FA and the chip surface is so small that the best coupling between the GCs and the FA is realized.

We also noticed that, after alignment, the gap between the FA and the chip surface can be varying due to environmental mechanical vibrations. These variations can change the coupling efficiency of the fibers and thus strongly influence the output signals of the LDV. To avoid this impact, we usually glue the FA to the chip using an index matching gel after the alignment. After a 5-minute ultraviolet-light curing process, the FA and the chip can be strongly stuck together. The strong spurious variations disappear once the gluing process is finished.

During the measurement, the chip is pressed on a vacuum chuck by the atmospheric pressure. A lens designed for the infrared light signal is set in front of the

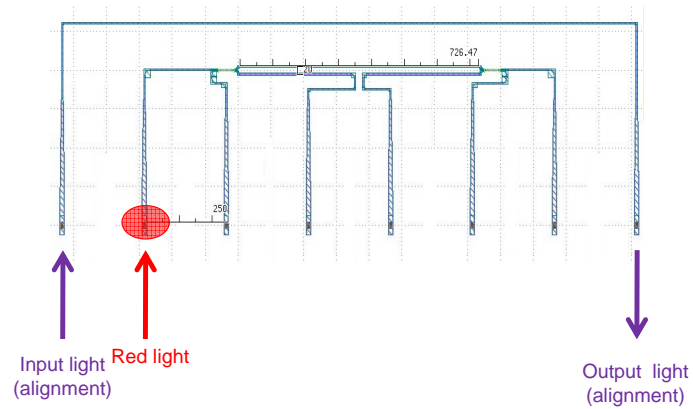


Figure 5.3: A PIC design with grating coupler array, which is customized to a fiber array with a pitch of $250\ \mu\text{m}$. A reference waveguide is also put in the design for the sake of alignment.

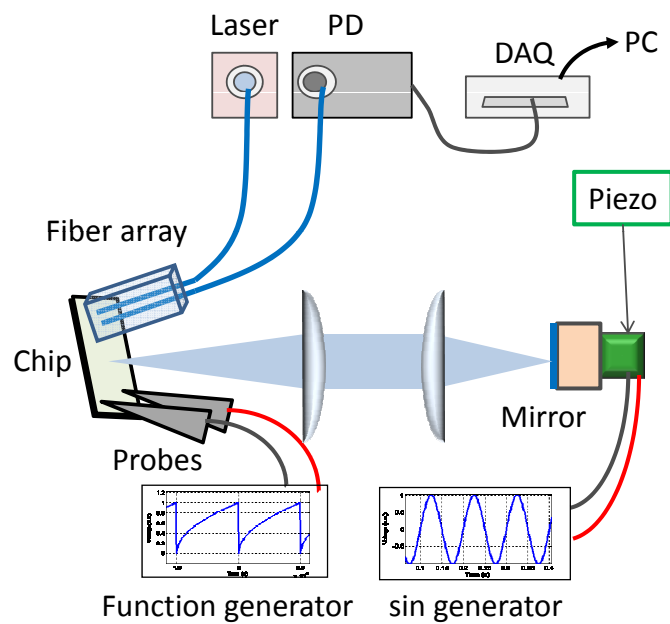


Figure 5.4: The measurement setup of the LDV.

chip and is used to focus the light signal from the chip to the target. For the target, we use a piezo stack to generate a desired vibration since the vibration frequency of the piezo stack can be precisely controlled. The setup used for a heterodyne LDV is shown in figure 5.4. If needed, a pair of electrical probes can also be used to apply a driving signal to the on-chip modulator. This setup can also be easily accustomed to a homodyne setup.

5.2 Heterodyne LDV

As is already mentioned in Chapter 4, the most important component in a heterodyne LDV is the optical frequency shifter (OFS), which is used to ensure that the carrier of the photocurrent signal (before demodulation) does not lie in the low frequency region, where the influence of $1/f$ noise is significant.

5.2.1 Proof-of-principle fiber-based setup for serrodyne based LDVs

Before the test of on-chip heterodyne LDVs, a proof-of-principle setup was implemented with the help of a fiber-based LDV system (see figure 5.5) to evaluate the performance of the serrodyne technique and the corresponding demodulation method. This setup was designed and measured by Stijn Meersman in his master thesis project [5]. These results are also reported in [6]. The optical frequency shifter (OFS) was realized with a LiNbO_3 phase modulator using the serrodyne technique.

The laser source was a distributed feedback (DFB) laser at 1550 nm, with a 3 dB linewidth of around 2 MHz. An isolator (not shown in figure 5.5) was inserted behind the laser to avoid optical reflections to the laser. In this setup, the relative intensity noise originated from the laser driver ($43 \text{ dB}/\sqrt{\text{Hz}}$ lower than input laser power) dominated over other noise sources when the optical power incident on the detector was higher than 100 nW. If this power was lower than 100 nW, the discretization noise (-85 dBm/Hz) from the 16-bit ADC became dominant. The demodulated signal can be strongly distorted due to the large relative noise. To avoid this noise influence, the reflection of the measurement signal from the moving target needed to be enhanced. Therefore, a focuser with an NA of 0.1 was used to focus the laser beam onto one small spot of the vibrating surface. A retroreflective film was also attached on top of the moving target to improve the reflected power by more than 10 dB.

In the measurement arm, light went to the vibrating target (a moving membrane of a loudspeaker) through a circulator and the aforementioned focuser. However, a small fraction of spurious light signal (around -50 dB) went directly from Port 1

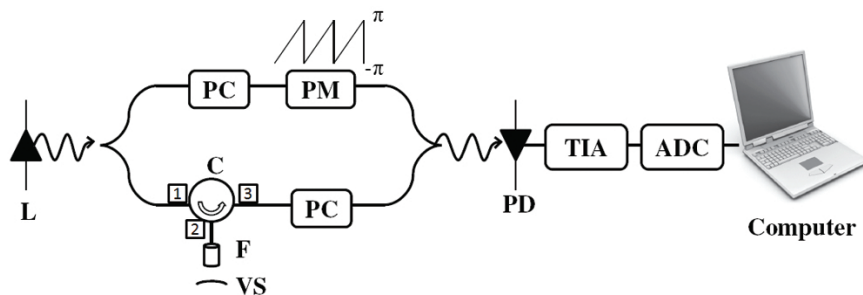


Figure 5.5: Schematic configuration of the experimental setup. In the figure, **L** stands for the laser, **C** stands for the circulator, **F** stands for the focuser, **VS** stands for the vibrating surface, **PM** stands for the phase modulator, **PC** stands for the polarization controller, **PD** stands for photo-detector, **TIA** stands for transimpedance amplifier, **ADC** stands for analog-to-digital converter. Reproduced from [6].

to Port 3 of the circulator. Moreover, the surface of focusers also introduced reflections. These signals to some degree deteriorate the results of demodulation.

Several polarization controllers were inserted to align the polarisation of measurement and reference arms. The optical path length difference of the measurement and reference arms were set to be smaller than the coherence length of the laser so that the signals are still in coherence before recombining.

In the optical combiner, the beams from both arms were recombined and sent to an InGaAs photodiode. The photocurrent was converted to a voltage signal by a homemade transimpedance amplifier (TIA). In the TIA, the lower frequency signals were filtered out to reduce the influence of low frequency noise. Then the signal was digitized with a data acquisition card (NI USB-6218). The demodulation was realized in MATLAB.

The optical power of the reflected signal from the target into the fiber was measured to be 20 dB less than the power sent to the moving surface. However, it was still 30 dB above the spurious reflection from the circulator and focuser. In order to have a good SNR, a 99:1 optical coupler to split the light asymmetrically (99% of light was sent to the measurement arm) was used to compensate the 20 dB optical loss in the measurement arm. In our experiment, the power of the laser was reduced to $50 \mu\text{W}$ and the corresponding optical power on the detector was 200 nW. An SNR of 40 dB was obtained from the measurement.

A function generator was used to create the sawtooth phase profile in the light going through the PM. Because of the linear relation between the phase and voltage in the electro-optic effect, a sawtooth voltage was directly provided to the phase modulator. When the peak-to-peak amplitude of the sawtooth voltage was 7.08 V, a good suppression of the 2nd order sidebands (combined with -2nd order)

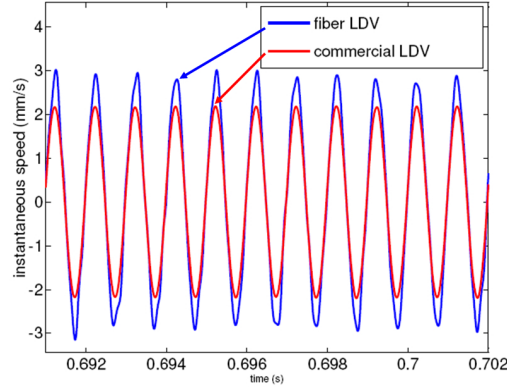


Figure 5.6: Comparison of the demodulated results between Polytec LDV and fiber-based serrodyne LDV.

was obtained. The ratio of this sideband to the fundamental harmonic was around -35 dB, and hence the corresponding phase error was smaller than 1%. The limited suppression ratio was mainly caused by the imperfect polarization of the input field to the phase modulator.

Sound vibrations at several different frequencies (between 300 Hz and 6 kHz) produced by the membrane of a loudspeaker were then measured. The frequency shift f_{ofs} in the reference arm was set at 24 kHz. A digital bandpass filter with a center frequency of 24 kHz and a bandwidth of 12 kHz was used to filter out the low frequency noise and high order harmonics.

Our measurement results were compared with those obtained from a commercial LDV instrument (Polytec OFV-5000). Both our fiber based and Polytec LDVs were pointed to the same vibrating membrane, and the measurements were done for the same duration. Two measurement results are shown in figure 5.6. It turned out that the vibration frequencies measured by both devices matched well, while the vibration amplitudes were somewhat different (ratio χ is 0.76). This difference may be caused by the mismatch of the measuring positions for the two devices.

A figure of resemblance (FOR) was defined as

$$\text{FOR} = 1 - \frac{\text{RMS}(v_P - \chi v_f)}{\text{RMS}(v_P)}, \quad (5.1)$$

with v_P and v_f the vibration speed measured with the Polytec LDV and our fibre LDV respectively. The calculated FOR for different vibration frequencies f_{vib} and peak velocities of the membrane of the loudspeaker are shown in figure 5.7(a).

It can be seen that the trends for all vibration frequencies were the same. At low peak velocities (around $100 \mu\text{m/s}$), the FOR was rather low. This is because

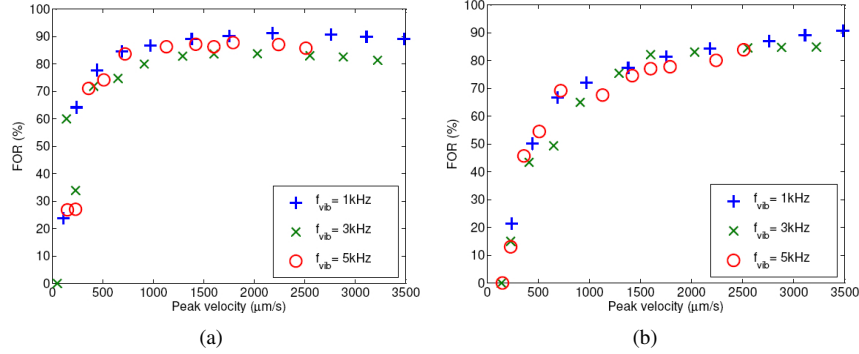


Figure 5.7: Figure of resemblance for different vibration frequencies and speeds with difference bandwidths of bandpass filters. (a): bandwidth of 12 kHz. (b): bandwidth of 24 kHz.

the phase variations in these situations were so small that they were strongly distorted by the phase noise. When the peak velocity surpass 300 $\mu\text{m/s}$, the FOR was higher than 60%. For peak velocity higher than 800 $\mu\text{m/s}$, the FOR exceeded 80%. However, at even higher speeds the FOR saturated and even dropped slightly. This is because the bandwidth of our signal became larger than the bandwidth (12 kHz) around f_{ofs} . Information would then be lost after filtering, resulting in distortions. The bandwidth of the bandpass filter was increased to around f_{ofs} , and the corresponding FOR figure is shown in figure 5.7(b). The dropping part in figure 5.7(a) disappeared. But noise introduced by the larger filter bandwidth deteriorated the demodulation and decreased the FOR for low speeds vibrations.

Our measured vibrations with sound frequencies starting from around 1000 $\mu\text{m/s}$ were relatively accurate, with an FOR larger than 80%. This corresponded with a peak displacement in the order of 100 nm.

5.2.2 On-chip heterodyne LDV with TO-based serrodyne OFS

An LDV PIC with an TO serrodyne LDV [7] is demonstrated in this section. This device is fabricated via ePIXfab and post-processed in the cleanroom of Ghent University. A repetitive square-root-of-time voltage with a peak-to-peak amplitude V_{pp} of 3.75 V was applied across the heater in order to generate a phase modulation with a peak-to-peak amplitude of 2π in the TO modulator. Since the resistance of the heater was around 1 k Ω , the average power consumption of the heater was around 7 mW. The frequency shift f_{ofs} of this serrodyne OFS is kept at 2 kHz. The light transmission antenna used in this device is a tilted focusing grating coupler (see Chapter 3) with an oblique angle $\alpha = 20^\circ$, and it also works as a light receiving antenna for collecting reflected signal from the vibrating surface. The 2×2 optical

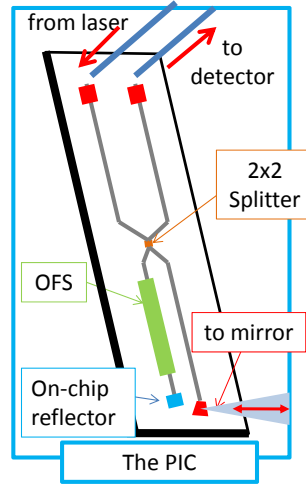


Figure 5.8: The PIC design of a Michelson type heterodyne LDV PIC.

splitter is realized with a multimode interference (MMI) coupler (3.96 μm long, 2.95 μm wide).

The measurement setup has already been shown in figure 5.4. The PIC design of the Michelson type LDV is schematically shown in figure 5.8. In this setup, coherent light with a wavelength of 1550 nm and a 3 dB linewidth of about 2 MHz is sent into the on-chip interferometer via a standard on-chip grating coupler. The signal is split into two paths by a 2×2 3dB MMI coupler. The measurement light was sent out of the chip via a tilted grating coupler. Microscope images of both the MMI and the tilted focusing grating coupler are shown in figure 5.9. With the help of two aspherical lenses, the measurement light is focused perpendicularly onto a vibrating mirror attached to a piezo-stack. The reflected light from the mirror is recaptured by the same tilted grating coupler on the chip. The round trip distance of light in free space is about 40 cm, which is much less than the coherence length of the light. Since the grating coupler is polarization sensitive, only the reflected light with the correct polarization can be coupled back to the chip. A TO-based serrodyne OFS and an on-chip reflector are put in the reference arm (see figure 5.9). The signals from both the measurement and the reference arms are recombined in the same 2×2 MMI as mentioned before, and sent to an external photo-detector via another grating coupler.

An IQ demodulation is implemented in software. With this method, two signals $I(t) \propto \alpha(t) \cos[\theta(t)]$ and $Q(t) \propto \alpha(t) \sin[\theta(t)]$ are derived from the photocurrent signal $i(t)$ in the demodulator (see Chapter 2). The angle of the vector $I(t) + iQ(t)$ equals $\theta(t)$. In the measurement results, it is usually found that the

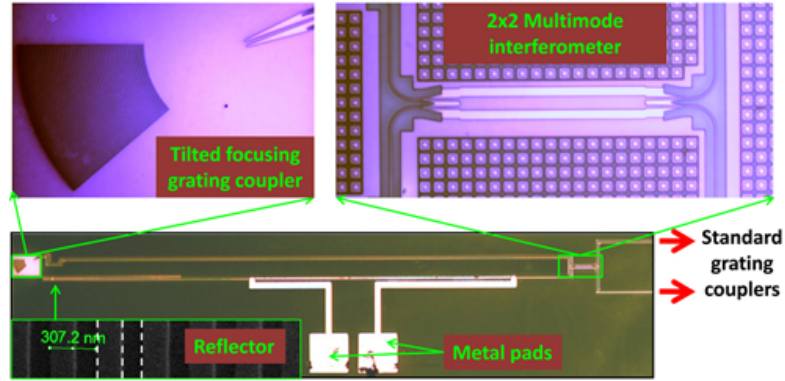


Figure 5.9: Microscope images of the PIC. Images of the tilted grating coupler [8], 2×2 multimode interference coupler, and reflector are also shown.

trace of the vector is a circle, but the center of the circle is not in the origin, indicating that $I(t) \propto \alpha \cos[\theta(t)] + I_0$ and $Q(t) \propto \alpha \sin[\theta(t)] + Q_0$. As is mentioned in Chapter 2, two main causes are responsible for this deviation: the 0th order harmonic and spurious reflections. By measuring the ratio between the shift of the IQ circle center and the radius of the circle, the relative power strength of the spurious reflection (and the 0th order harmonic) with respect to the useful signal can be estimated.

Results of the recovered displacement measured from the on-chip LDV are compared with those from a commercial LDV from Polytec. The time dependent displacements for both measurements are shown in figure 5.10. Note that the two measurements were done separately, and we did not try to match the phases of the results. The curves in figure 5.10(a) and figure 5.10(b) are the measurement results of a vibrating piezo-stack driven by a sinusoidal voltage signal at 22.6 Hz. The peak-to-peak values of the drive voltages are 50 V and 100 V, respectively.

The frequency response of this piezo stack was measured by both the on-chip and Polytec LDV systems, and they are shown in figure 5.11. It can be seen that both measured responses are quite similar. However, most of the results from the on-chip LDV were smaller than those from Polytec, and the corresponding ratios were mostly within the region of 90% and 95%. The cause for this deviation is under further investigation. However, it is possible to correct the on-chip outputs by multiplying the demodulated values with a calibration factor.

The IQ traces for most of the measurement results are nice circles, which means that a proper serrrodyne signal was generated. According to the measurement results, the power ratios between the recaptured useful reflection and the reference light are between -8 dB and -14 dB. The loss of the reflected light is

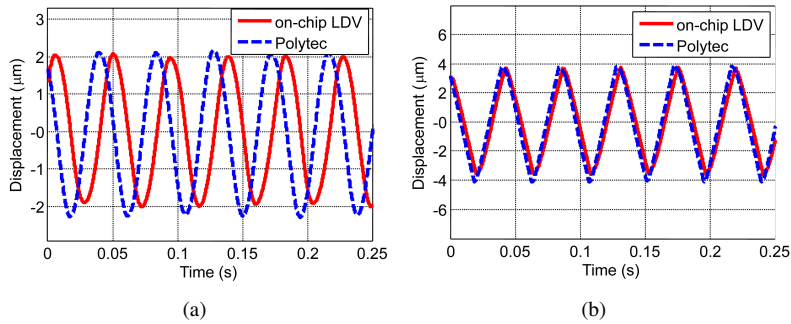


Figure 5.10: Demodulated displacements for on-chip LDV: the solid red curve stands for results measured with on-chip LDV, and the blue dashed lines are for results from Polytec LDV. Results in 5.10(a) are for the piezo vibration driven by a 50 Vpp signal, while those in 5.10(b) are for the vibration driven by 100 Vpp.

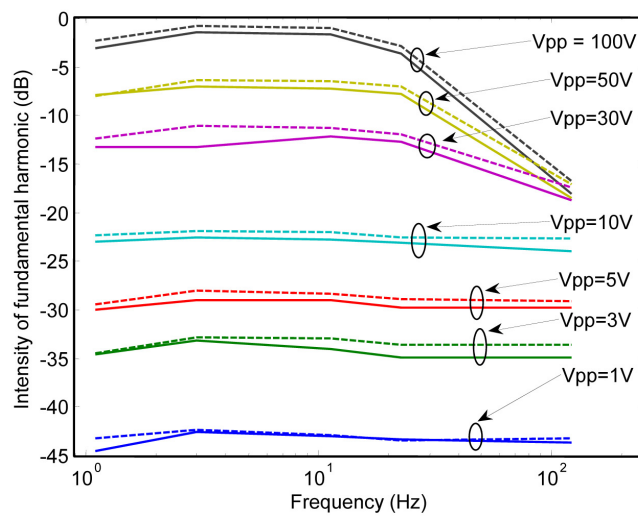


Figure 5.11: Response of the piezo-electric stack measured both by on-chip LDV (solid lines) and Polytec LDV (dashed lines). The peak-to-peak voltages of the piezo driver are chosen as: 1 V, 3 V, 5 V, 10 V, 30 V, 50 V, and 100 V.

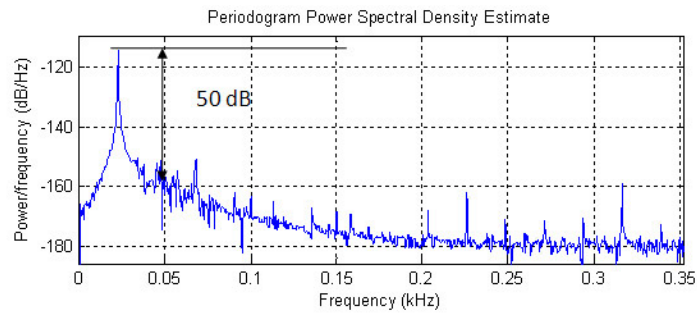


Figure 5.12: The power spectral density of the demodulated signal, when the piezo stack is driven by a 50 Vpp signal at 22.6 Hz.

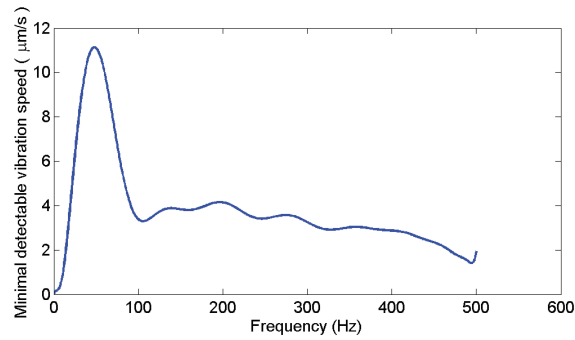


Figure 5.13: The power spectral density of environmental vibrations measured using LDV PIC with TO serrodyne frequency shift.

mainly caused by the coupling loss in the grating coupler and imperfect alignment of the optical system. By estimating the modulation depth of the photo-current while the vibrating surface is moved away and no useful reflection is sent back to the LDV, the ratio between the spurious reflection and the reference light can be obtained. This ratio turns out to be a stable value in time, which is about -23 dB. The major part of the spurious reflection probably comes from the 2×2 MMI. Because the stability of this ratio, the compensation method, which shifts the IQ trace center back to the origin, can thus work well. This compensation method will face problems if the useful reflection is too weak, in which case a small fluctuation in the spurious reflection can have a strong influence on the LDV output. According to the measured results, the compensation method can work well even when the power ratio between the recaptured useful light and the reference light reaches -30 dB, which means that the mirror can be replaced by a white paper. The grating coupler is good enough to be used for such a coupling efficiency.

The signal-to-noise ratio (SNR) due to the shot noise can be calculated using

$$SNR = \frac{RP_m P_r}{q_0 B(P_r + P_m)}, \quad (5.2)$$

where P_m and P_r are the power values of the measurement and reference signals respectively, $R \approx 1A/W$ is the responsivity of the detector, $q_0 = 1.6 \times 10^{-19}C$ is the elementary charge, and B is the bandwidth. According to this equation, the shot noise limited SNR value of the experiment results is larger than 130 dB. However, the quantization noise in the analog-to-digital converter (ADC) is around -85 dB less than the signal, which is larger than the shot noise. The power spectral density of the demodulated signal corresponding to figure 5.10(a) is plotted in figure 5.12. It can be found that the SNR is only 50 dB in this measurement, and this is because the environmental vibrations also have an influence on the mirror. The power spectral density of the background vibration is measured and shown in figure 5.13. It can be found that the environmental vibration is mainly near 50 Hz. In order to obtain the shot noise limit, the quantization noise in the ADC has to be suppressed by increasing the ADC resolution, and a better compensation method should also be implemented.

Due to the bandwidth limitation of the optical frequency shifter, the frequency and amplitude of the vibrations is limited according to Carson's bandwidth rule [9]: $f_{ofs} > 2(f_v + f_D)$, where f_v is the vibration frequency of the target, and f_D is the Doppler frequency shift corresponding to the maximal velocity of the vibration. The measured maximal and minimal vibration velocities of this device are around $400 \mu\text{m/s}$ and $0.8 \mu\text{m/s}$, respectively. The maximal f_D is thus around 500 Hz, which means that it still fulfills Carson's rule if the vibration frequency is increased to 500 Hz. This on-chip LDV system can be useful in applications that only measure small vibrations at low frequencies. In order to measure vibrations with higher frequency or larger amplitudes, a faster optical frequency shifter

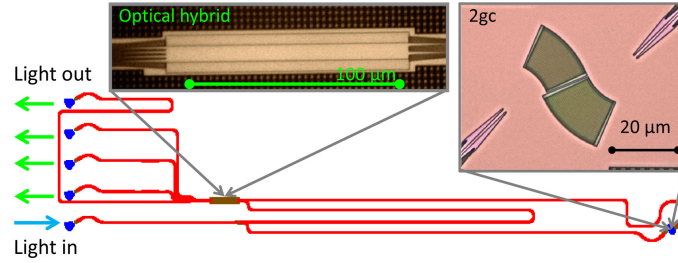


Figure 5.14: The PIC design and microscope images of the 90° optical hybrid and of the 2gc light receiving components.

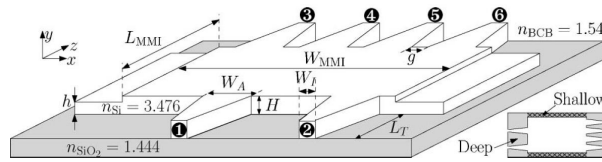


Figure 5.15: Schematic show of a 90° optical hybrid. Reproduced from [10].

is needed. This might be realized by using a carrier injection/depletion based optical phase modulator, whose bandwidth could be larger than several gigahertz. However, as is mentioned, these phase modulators suffer from parasitic amplitude modulation and appropriate measures are needed to mitigate the impact of amplitude modulation.

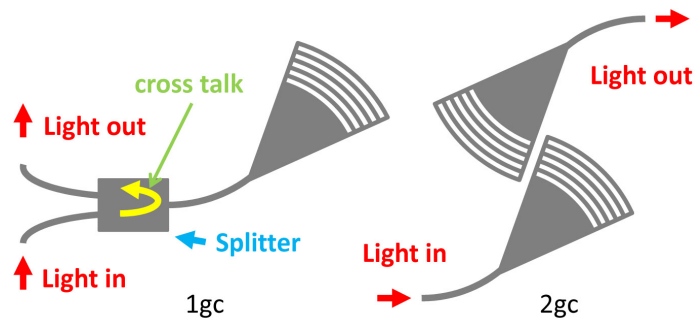


Figure 5.16: The configuration of the 1gc type and the 2gc type light receiver.

5.3 On-chip homodyne LDV

A number of homodyne LDVs with compact 90° optical hybrids were also fabricated via ePIXfab and characterized in our lab [11]. The PIC design and microscope images of several key components are shown in figure 5.14. The schematic show of the 90° optical hybrid is shown in figure 5.15 [10]. In our design, the width and the length of the multimode region are chosen as $W_{MMI} = 7.7 \mu\text{m}$ and $L_{MMI} = 115.5 \mu\text{m}$. Measurement results from [10] shown that, in the wavelength band between 1510 nm and 1555 nm, the phase error of this device was within $\pm 5^\circ$ and the common mode rejection ratio (CMRR) in this band was below -20 dB.

In these designs, two different light coupling configurations used for sending and receiving measurement signals are shown in figure 5.16. A grating coupler and a 1×2 optical splitter are deployed in the first configuration (1gc), while two adjacent grating couplers are used in the second configuration (2gc). Both configurations can be used for receiving the reflected measurement light, though they still have several problems. The 1gc design suffers from a strong spurious reflection (the cross talk between the two left ports of the splitter, see figure 5.16) and a significant power loss (at least 6 dB) in the optical splitter. The cross talk problem is alleviated in the 2gc design since the two optical ports are not connected on chip. However, since the two grating couplers are spatially separated, the imaging system used for picking up the reflected light can not ensure a sufficient coupling efficiency in the back-reflection. Note that the two grating couplers in the 2gc design are different because their common coupling direction is not perpendicular to the chip surface.

To estimate the receiving efficiency of the measurement signal, the phase in the measurement reflection is modulated during the measurement, by creating a mechanical vibration in the surface where the measurement light is focused. The amplitude of the vibration should be larger than $\lambda_0/2$ so that the maximum amplitude modulation depth is obtained. In practice, a piezo stack was used, driven by a 60 Vpp voltage signal oscillating at 31 Hz. According to the measured modulation depths, the power ratio of the reflected measurement signal to the reference signal was -28 dB for the 2gc LDV, and -34 dB for the 1gc LDV. This result indicates that the 2gc LDV is better than the 1gc LDV in terms of power efficiency.

To retrieve the values of the spurious reflections, the wavelength dependence of the photocurrent signals was measured. This was done by measuring the average values of the photocurrents for different wavelengths while the measurement signal is still under modulation. Since the reference signal and the spurious reflection have different optical lengths in the interferometer, an amplitude modulation is obtained in the average photocurrents and the corresponding modulation depth reveals the strength of the spurious reflection. The average optical power of each port (DC_j) is derived from the average photocurrent and plotted as a function of

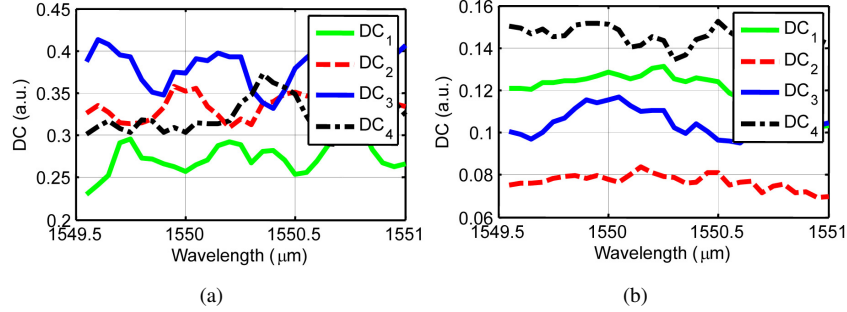


Figure 5.17: (a) The average light power values at each output port (DC_j) for the homodyne 1gc LDV. (b) DC_j for the homodyne 2gc LDV.

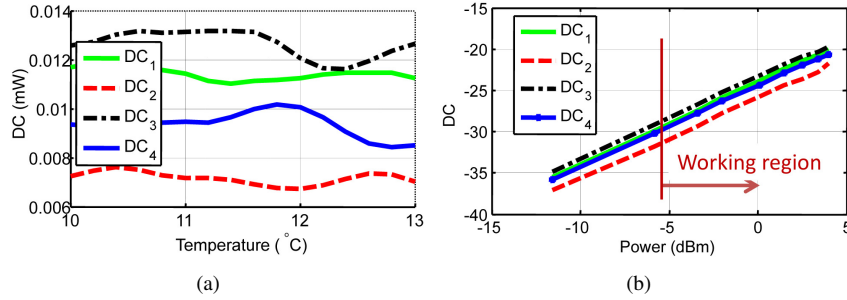


Figure 5.18: (a) The average light power values at each output port (DC_j) as a function of device temperature (2gc LDV). (b) DC_j as a function of the input power (2gc LDV).

wavelength in figure 5.17(a) and figure 5.17(b). It is shown that the 2gc LDV has weaker DC signals than the 1gc LDV, but its modulation depths are also weaker than those of the 1gc LDV. The modulation depths indicate that the spurious reflection in 1gc LDV is about -25 dB lower than the reference signal, while that value in the 2gc LDV is lower than -30 dB.

Since the 2gc LDV picks up more back-reflection and has less spurious reflection than the 1gc LDV, we will focus on the 2gc LDV in the following paragraphs. The differences between 1gc and 2gc LDVs are summarized in Table 5.1.

The temperature stability of the PIC based homodyne LDV with a 2gc light receiving component is also experimentally examined. The measured DC_j signals are shown in figure 5.18(a). The main cause for the deviations of these DC_j signals is the temperature-induced phase changes in the on-chip spurious reflections. These deviations are significant (up to 17%) as the temperature increases from 10°C to 13°C. In order to improve the performance of the PIC based LDVs, we suggest stabilizing the chip temperature within 0.5°C by attaching a temperature

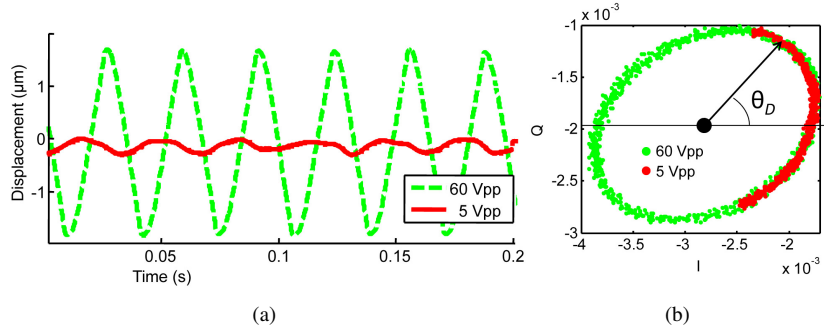


Figure 5.19: (a) Demodulated signals for two vibrations in time domain. (b) IQ Lissajous curve.

stabilizer to the chip.

The relations between the input optical power and the average light power values at the four outputs (DC_j) are shown in figure 5.18(b). By comparing the total power of the four outputs with the input light power, it is found that the total loss of the optical power in the PIC-based LDV is around 18 dB. If the input light power is lower than -6 dBm, noise from the laser and the detectors would dominate and deteriorate the demodulation results.

Homodyne LDVs are capable of measuring vibrations with large amplitudes and frequencies. The largest detectable amplitude and frequency are limited by the sampling rate of the analog-to-digital converter (ADC) and the speed of the DSP. With our present ADC which works with a sampling rate of 20 ksps, the maximal detectable velocity is around 7 mm/s. This value can be further increased once a higher sampling rate is used. This device can also be used to measure small mechanical vibrations (with an amplitude smaller than $\lambda_0/2$) if a temperature stabilizer is introduced and the active compensation approach for sub-half-wavelength vibrations is applied. In figure 5.19(a), the measured displacements of a piezo stack driven by two different oscillating voltage signals are shown. These two voltage signals have different peak-to-peak amplitudes, i.e. 60 Vpp and 5 Vpp,

Type	measurement reflection (dB)	spurious reflection (dB)
1gc	-34	-25
2gc	-28	<-30

Table 5.1: Performance of 1gc and 2gc LDVs, all values are compared with the power of the reference light.

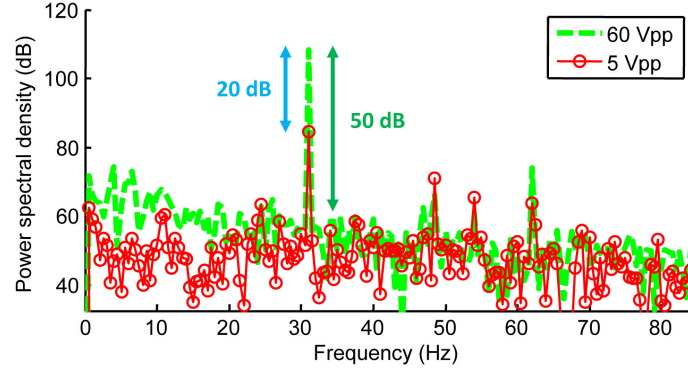


Figure 5.20: Power spectral densities of the LDV outputs for the two vibration signals.

but the same oscillating frequency (31 Hz). These displacement values are calculated using the aforementioned “arc-tangent” algorithm. The vibration generated by the 5 Vpp voltage signal has an amplitude smaller than $\lambda_0/2$, but can still be measured with our active compensation approach for sub-half-wavelength vibrations. Their corresponding Lissajous curves and power spectral densities are also shown in figure 5.19(b) and in figure 5.20, respectively. It can be found that the measured power ratio between the two vibrations is around 20 dB. For the vibration driven by the 60 Vpp voltage signal, a signal-to-noise ratio (SNR) of around 50 dB is achieved. Derived from this SNR value, the minimal detectable vibration amplitude is around 6 nm, which corresponds to a peak velocity of 1.2 $\mu\text{m/s}$ for this frequency.

5.4 Conclusions

In this chapter, we report several on-chip LDV devices, and these devices include both serrodyne-based heterodyne and optical-hybrid-based homodyne LDVs.

For the serrodyne-based heterodyne LDV, a proof-of-concept measurement is firstly realized with an optical fiber system and a LiNbO_3 phase modulator, which is used to generate the serrodyne frequency shift. This fiber-based serrodyne LDV works well in the expected frequency and velocity range. Results show that this proof-of-concept system is able to measure audio frequency vibrations with sub-micron displacements (larger than 100 nm).

An on-chip laser Doppler vibrometer with a serrodyne OFS based on thermo-optic modulation is then reported. Vibrations of a piezo stack within the frequency range [1.1 Hz, 123 Hz] and the velocity range [0.8 $\mu\text{m/s}$, 400 $\mu\text{m/s}$] were measured with the on-chip LDV. Compared with a commercial LDV, the on-chip LDV is proved to be able to retrieve the instantaneous displacements in this range with a

Type	min d (nm)	min v ($\mu\text{m/s}$)	max v ($\mu\text{m/s}$)
fiber heterodyne	100	1000	>3500
on-chip heterodyne	1	0.8	400
on-chip homodyne	6	1.2	depends on ADC

Table 5.2: The performance summary.

good accuracy. Theoretically, the measurable frequency range of this TO-based serrodyne on-chip LDV can be extended to 500 Hz if the vibration is not larger than 400 $\mu\text{m/s}$.

Finally, an on-chip homodyne LDV is demonstrated. This homodyne LDV operates with a minimal input light power of around -6 dBm. Besides the noise in lasers and detectors, on-chip spurious reflection is the major source of deviation in these on-chip homodyne LDVs. With the help of an active compensation approach, the homodyne LDV is capable of measuring vibrations with amplitudes larger than one half of the light wavelength (775 nm). When measuring a sub-half-wavelength vibration, an extra temperature stabilizer and a specific active compensation approach for sub-half-wavelength vibrations are required. According to the measurement results, the minimal detectable amplitude of a 31 Hz vibration is around 6 nm, which corresponds to a velocity of 1.2 $\mu\text{m/s}$.

The key parameters of each device are summarized in table 5.2. These data are based on our measurement results, and all of these setups can be improved. For the fiber-based heterodyne LDV with $f_{ofs} = 24$ kHz, the measured vibrations have large deviations at low frequency region since a large bandwidth in the pass band of the filter is used and thus more noise is introduced to the signal. For on-chip TO-based heterodyne LDV, $f_{ofs} = 2$ kHz. Therefore a bandpass filter with a small bandwidth is required in this case, which ensures a signal with weak noise. But this small filter bandwidth confines the measurement range of the LDV. Compared to heterodyne LDVs, homodyne LDVs have relatively worse measurement resolutions due to low frequency noise, but they may have a larger measurement range.

References

- [1] <http://www.epxifab.eu>.
- [2] S. Stankovic, R. Jones, M. N. Sysak, J. M. Heck, G. Roelkens, and D. Van Thourhout. *Hybrid III-V/Si Distributed-Feedback Laser Based on Adhesive Bonding*. IEEE Photonics Technology Letters, 24:2155–2158, 2012.
- [3] L. Vivien, J. Osmond, J.-M. Fédéli, D. Marris-Morini, P. Crozat, J.-F. Damlencourt, E. Cassan, Y. Lecunff, and S. Laval. *42 GHz p.i.n Germanium photodetector integrated in a silicon-on-insulator waveguide*. Optics Express, 17(8):6252–7, April 2009.
- [4] OZ-optics. *Data sheet: V-GROOVE ASSEMBLIES*, 2013.
- [5] Stijn Meersman. *Analysis and Proof-of-principle Implementation of a Laser Doppler Vibrometry based Middle Ear Microphone*, 2010.
- [6] Yanlu Li, Stijn Meersman, and Roel Baets. *Realization of fiber-based laser Doppler vibrometer with serrodyne frequency shifting*. Applied optics, 50(17):2809–14, June 2011.
- [7] Y. Li, S. Verstuyft, G. Yurtsever, S. Keyvaninia, G. Roelkens, D. Van Thourhout, and R. Baets. *Heterodyne laser Doppler vibrometers integrated on silicon-on-insulator based on serrodyne thermo-optic frequency shifters*. Applied Optics, 52(10):2145–52, April 2013.
- [8] D. Vermeulen, Y. De Koninck, Y Li, E. Lambert, W. Bogaerts, R. Baets, and G. Roelkens. *Reflectionless grating coupling for silicon-on-insulator integrated circuits*. In Group IV Photonics (GFP), 2011 8th IEEE International Conference on, volume 1, pages 74–76. IEEE, 2011.
- [9] J. R. Carson. *Notes on the theory of modulation*. In Proc. IRE, pages 57–64, 1922.
- [10] R. Halir, G. Roelkens, A. Ortega-Moñux, and J. G. Wangüemert-Pérez. *High-performance 90 degree hybrid based on a silicon-on-insulator multimode interference coupler*. Optics Letters, 36(2):178–80, January 2011.
- [11] Y. Li and R. Baets. *Homodyne laser Doppler vibrometer on silicon-on-insulator with integrated 90 degree optical hybrids*. Optics Express, 21(11):13342–13350, 2013.

6

Multi-point LDVs for arterial pulse wave velocity (PWV) measurements

In Chapter 5, the discussion was focused on single-point LDVs, which measure the instantaneous velocity (or displacement) of only one vibrating point at each time step. However, for many applications, such as complex flow measurements and pulse wave velocity (PWV) measurements, the vibration information of only one point is not enough. Some techniques, such as particle image velocimetry (PIV) [1] and scanning LDV [2], have been developed to obtain the vibration information of multiple positions. However, both of these techniques face problems for applications requiring high time-resolution output: the PIV technique is limited by the frame rate of the image recording devices, and the scanning LDV suffers from a reduced time resolution due to scanning.

To solve these problems, some techniques have been developed to realize high time-resolution multi-point LDVs. For example, a design taking advantage of the multiple diffraction orders of an acousto-optic modulator (AOM) allows a simultaneous measurement of ten vibrating positions [3, 4]. However, this device is based on an optical fiber system and is not compact enough. The discussions in previous chapters have shown that very compact LDVs can be realized on the SOI platform, and this high degree of miniaturization indicates the capability of supporting multiple LDVs. In this chapter, we report an SOI-based double-point LDV used for the arterial pulse wave velocity (PWV) measurement, to emphasize the advantage of the SOI technology in the field of multi-point LDVs.

According to publications [5–7], the arterial PWV is an important and inde-

pendent marker for cardiovascular risk. The Laser Doppler vibrometry has already been suggested as a potential technique to measure the local carotid PWV by measuring the transit time of the pulse wave between two locations along the common carotid artery (CCA) from the skin surface vibrations. However, present LDV-based PWV measurement setups require two stand-alone vibrometers, and hence are bulky and difficult to handle. In our solution, the two stand-alone LDVs are integrated on the same SOI chip, so as to reduce the device volume and the fabrication cost, and improve the operation convenience.

This chapter is organized as follows: In the first section, the background of PWV is reviewed. Then the on-chip dual-LDV systems design is presented. Calibration and *in-vivo* PWV measurements are reported and discussed afterwards. Finally, a concept design to mitigate the difficulty in optical alignment during operation is proposed.

6.1 Pulse wave velocity (PWV)

Pulse wave velocity (PWV) is an important measure for arterial stiffness, which is highly related with many cardiovascular diseases [8]. A larger value of PWV indicates a greater arterial stiffness and thus a higher risk of cardiovascular events, so in clinical practice PWV is used as an important and independent predictor of cardiovascular mortality [5–7]. In practice, the carotid-femoral PWV, which describes the average velocity of the arterial pulse propagating from the carotid to the femoral artery (see figure 6.1), is usually used. The carotid-femoral PWV value normally lies between 4 m/s and 12 m/s for a healthy people [9]. The European Society of Hypertension suggested that a carotid-femoral PWV of 12 m/s can be considered as the threshold of an estimate of subclinical organ damage [10], and individuals with carotid-femoral PWV higher than this threshold should seek for clinical treatments to prevent cardiovascular events.

Several devices have been introduced to measure the PWV, the most well known being the Complior and Sphygmocor system [7]. For the assessment of local arterial PWV, however, there are no widespread commercial devices. It is only since recent that efforts have been undertaken to measure the propagation of the pulse using fast ultrasound-based techniques [12, 13]. Additionally, the measurement setup of the carotid-femoral PWV is usually bulky and sometimes causes discomfort to subjects because they are palpated in the groin. A new noninvasive method to measure the local PWV of the common carotid arteries (CCAs) using laser Doppler vibrometry (LDV) technique has been proposed [6, 14]. This method simplifies the measurement procedures and also overcomes the uneasiness in the conventionally used carotid-femoral PWV measurement. However, the proposed measurement setup for the CCA PWV measurement is still bulky, which prevent this technique from being widely used.

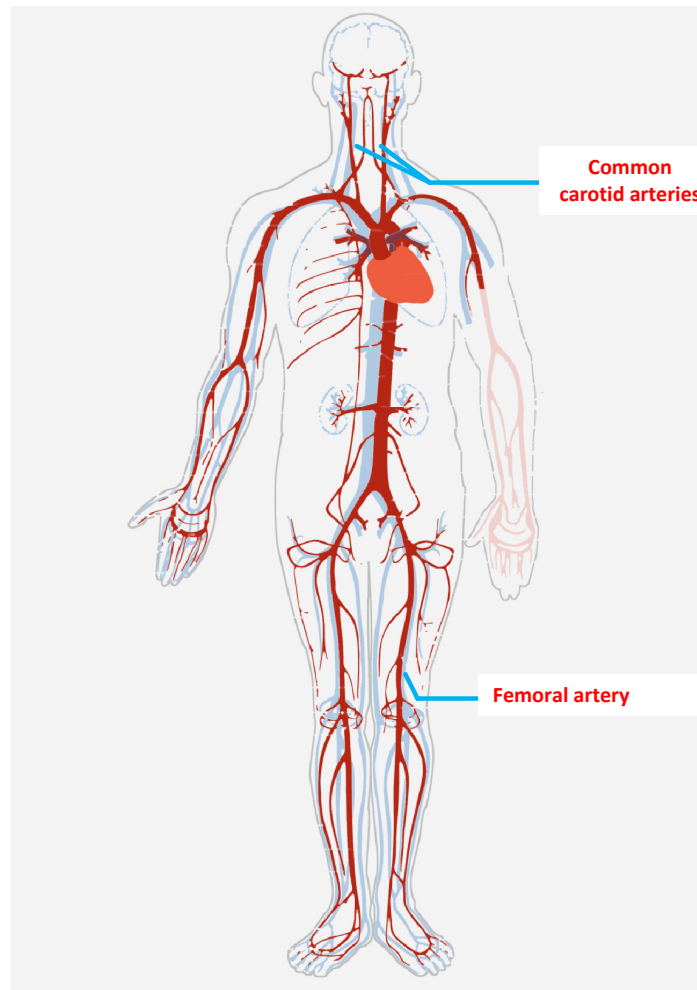


Figure 6.1: The artery system. Adapted from [11]

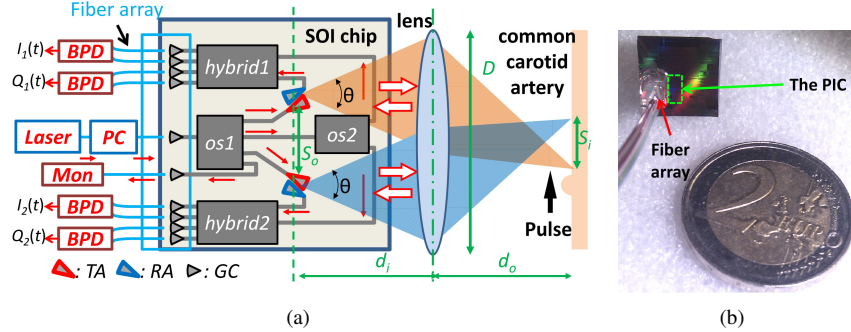


Figure 6.2: (a) The schematic of the PWV measurement device using a dual-LDV PIC chip. In the figure *os* stands for optical splitter, *hybrid* for 90° optical hybrid, *PC* for polarization controller, *BPD* for balanced photo-detectors, *Mon* for monitor, *TA* for transmitting antenna, *RA* for receiving antenna, *GC* for grating coupler. (b) The photo of a real dual-LDV chip with a bonded fiber array, compared with a two euro coin.

6.2 On-chip Dual-LDV device

In chapter 5, the detailed principle of a single homodyne LDV integrated on SOI has been described. The proposed PIC-based PWV measurement device consists of two interferometers, and each works as a stand-alone homodyne LDV. The schematic of the on-chip system and the measurement setup are shown in figure 6.2(a). Although techniques of integrating lasers and photo-detectors (PDs) on SOI chips have already been developed [15, 16], we still use external laser and PDs in this proof-of-concept setup to solely test the performance of the passive optical system. The light source and the PDs are connected with the chip via a fiber array (FA).

In the operation, coherent light generated in the external laser is sent to the chip via the FA. A polarization controller (*PC* in figure 6.2(a)) is used to ensure an optimized coupling efficiency from the fiber to the on-chip grating coupler (*GC*). In the 1×4 optical splitter (*os1* in figure 6.2(a)) light is split into four parts: two parts are the measurement signals of the two stand-alone LDVs, the third part is split again into two reference signals with another optical splitter (*os2*), and the fourth part is directly sent out to a detector (*Mon* in figure 6.2(a)) to track the variations of the light intensity. Two light transmitting antennas (*TAs*) and two light receiving antennas (*RAs*), realized by means of grating couplers, are set in the measurement arms to send light out of the chip and receive back reflections, respectively. A lens is set in front of the chip to focus the two light beams from the *TAs* onto two locations on the neck region of the CCA. The two *TAs* (or *RAs*) have a separation $S_o = 0.98$ mm to ensure an adequate large distance between the

two measurement positions S_i , which can be calculated as follows

$$S_i = |M|S_o = \left| -\frac{d_o}{d_i} \right| S_o, \quad (6.1)$$

where M is the magnification of the optical system, d_o and d_i are the object and image distances, respectively. The back-scattered signals are collected by the same lens and focused back to the chip, where they are picked up by the RAs. To ensure that enough reflection is coupled to their corresponding RAs, the locations of the RAs are set very close the TAs. According to the Doppler effect, the recaptured reflection signals carry the information of the vibrations in their time-dependent frequency shifts. They are mixed with the reference signals in the two 90° optical hybrids (see figure 6.2(a)). From each optical hybrid, four optical signals are obtained and sent to two external balanced PDs. The footprint of this PIC is smaller than 5 mm^2 , and most of the space is taken by the FA. A photo of the chip is shown in figure 6.2(b), in which the actual area of the dual-LDV PIC is shown in the green box.

With the help of an analog-to-digital converter (ADC), the generated photocurrents of the balanced PDs are transformed into digital signals which can be used to recover the instantaneous velocity information of each vibration using a digital ‘‘arc-tangent’’ demodulation method mentioned in Chapter 2. After the demodulation, two curves representing the instantaneous velocities of the vibrations can be obtained. The sampling time of the ADC t_s determines the maximal detectable displacement speed of the neck surface $v_m = \lambda_0/2t_s$, where λ_0 is the wavelength of the light. In our measurement, the sampling frequency $f_s = 1/t_s$ is chosen to be 40 kHz, which corresponds to a v_m of 31 mm/s. Note that the value v_m is not related to PWV.

Considering the resolution of a measured PWV, it is better to use a large S_i value, which is, however, limited by the size of the neck. In practice, the distance S_i is normally chosen to be larger than 1 cm, indicating that the value of $|M|$ is normally larger than 10. In this case, however, the numerical aperture of the lens on the image side is very small, which results in a strong reduction in the collected power of the backscattered light. In order to obtain a stronger reflection, two pieces of reflective tapes are attached on the sites where the vibrations are measured. Considering the source side of the lens, the aperture of the lens D should be large enough to collect both light beams from the chip to avoid additional loss, indicating that $D > D_c = S_o + 2d_o \tan(\theta/2)$, where $\theta \simeq 11^\circ$ is the divergence angle of the output light (see figure 6.2(a)). In this setup, a lens with a focus distance $f = 18.4 \text{ mm}$ and aperture $D = 5.5 \text{ mm}$ is used. The separation S_i is around 1.5 cm, which leads to $D_c = 4.8 \text{ mm}$ (being smaller than D).

In this device, the implemented LDVs are homodyne type rather than heterodyne type. This is because the homodyne LDV does not require the use of optical

frequency shifters (see [17]) and thus has a relatively low production cost compared to heterodyne. However, homodyne LDVs also have disadvantages, e.g. they may not work well for vibrations smaller than half a wavelength. But this problem is not critical in the PWV measurement and can be alleviated by stabilizing the laser source and using a temperature controller. In addition, the wave pulse is usually very strong and thus weaker vibrations can usually be ignored.

6.3 Algorithms for retrieving PWV

The PWV is usually retrieved by measuring the transit time of the pulse wave between the two measurement locations, denoted as Δt . The value of PWV can be obtained from Δt and S_i using the following formula

$$PWV = S_i / \Delta t. \quad (6.2)$$

The accuracy of the PWV measurement thus depends on the accuracy of the retrieved transit time Δt . The maximal detectable PWV value PWV_m is ultimately limited by the sampling frequency t_s of ADC, and their relation can be written as $PWV_m = S_i / t_s$. Providing $f_s = 40$ kHz and $S_i = 1.5$ cm, a PWV_m of 600 m/s can be obtained. The resolution of the PWV is

$$dPWV = PWV^2 \cdot t_s / S_i. \quad (6.3)$$

However, due to the inaccuracy in the algorithm for retrieving Δt and deviations in the measurements, the PWV_m is normally determined by the error in measured transit time, denoted as t_d , rather than the sampling time t_s . This transit time error depends on many factors, including physical changes between the two pulses, errors in the LDV outputs, and limitations in the algorithms used for retrieving Δt . In [6], a cross-correlation algorithm is used to retrieve the PWV, in which the transit time between the two measurement locations (Δt) is obtained from the cross-correlation of the two measured velocity curves. The accuracy of this method depends on the shape changes between the measured velocity curves of the two vibrations. These shape changes are partly caused by propagation dispersion of the pulse wave and reflection at sites with impedance mismatch [12], and partly caused by errors of homodyne LDVs when light reflection is not strong enough. Hermeling et al. proposed to use the transit time of the systolic foot of the pressure waveform [12], in which the deviation also depends on the shape variation and the accuracy of the LDV system. However, this algorithm is more complex than the cross-correlation method in many situations.

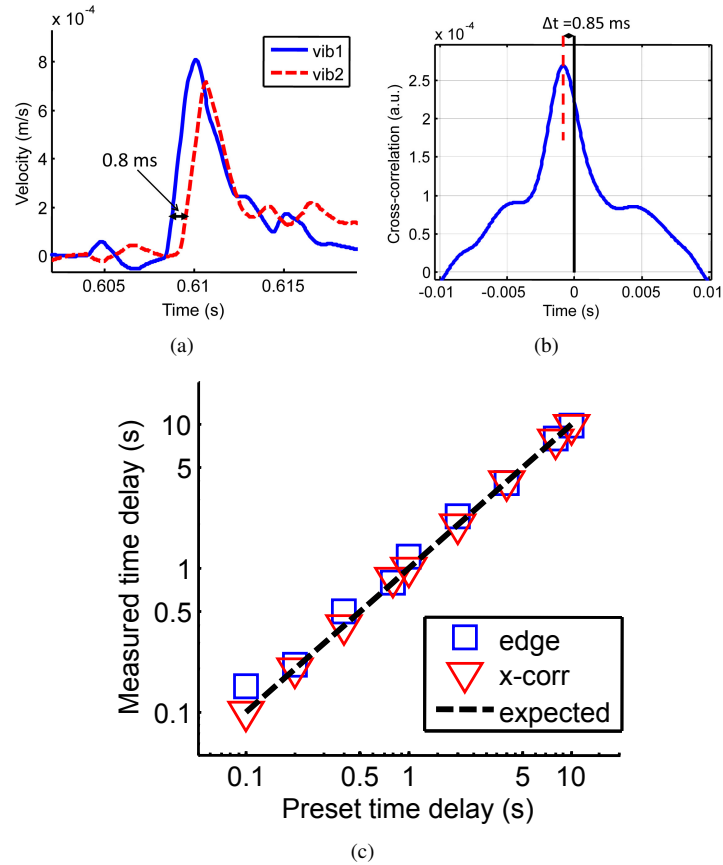


Figure 6.3: Calibration measurement results on two pulses generated on two separate loud speakers. The two pulses have the same shape but are generated at different times. (a) The measured two pulses with a delay of 0.8 ms. (b) The cross correlation of the two velocity curves, which shows a time delay of 0.85 ms. (c) The recovered delay time for different method, where x-corr means cross-correlation method.

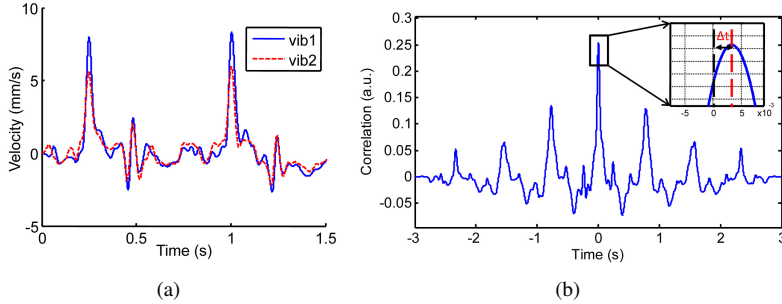


Figure 6.4: (a) The velocity curves of the two pulses. (b) The cross-correlation of the two measured pulses. A time delay $\Delta t = 3.3$ ms is obtained using the correlation method.

6.4 Calibration and *in vivo* measurement

The LDV PICs are fabricated via ePIXfab [18]. A calibration measurement was firstly done on two separate loudspeakers, on which two pulses were generated by two voltage signals with the same shape but a relative preset time delay Δt . The input light with a wavelength of 1550 nm has a power of 6 dBm and linewidth of 150 kHz. These challenging test conditions correspond to a pulse wave velocity of up to 150 m/s, which is well beyond the values that can be expected *in vivo*. In figure 6.3(a), the velocity curves of the two pulses with a preset delay $\Delta t = 0.8$ ms is shown. It can be seen that a time delay of 0.8 ms is retrieved from the leading edge delay of two pulses, while the delay derived from the cross-correlation method is around 0.85 ms (see figure 6.3(b)). The retrieved results of these two methods have been compared using a series of measurements (see figure 6.3(c)). It can be found that the deviations in time delay with both methods have no apparent difference, and both deviations are less than 0.2 ms. The measured root-mean-square deviations of the leading-edge and cross-correlation algorithms are 0.13 ms and 0.08 ms, respectively. The estimated deviation is mainly caused by the shape difference between the two pulses.

Then the device was used to measure the CCA PWV *in vivo*. The person under test was a healthy male volunteer aged 26 years. During the test, the volunteer was sitting in an upright position in front of the device, with two reflective tapes attached to two locations along the CCA. The separation of the two locations was between 1.5 cm and 1.7 cm. The two light beams were adjusted to be focused on the two reflective tapes, respectively. The demodulated velocity results for a representative measurement are shown in figure 6.4(a), and the cross-correlation of the velocities is obtained and shown in figure 6.4(b). It is seen that the transit time of the pulse is around 3.3 ms, and this corresponds to a PWV between 4.5 m/s and 5.2 m/s. The displacement and acceleration signals are also shown in figure 6.5(a)

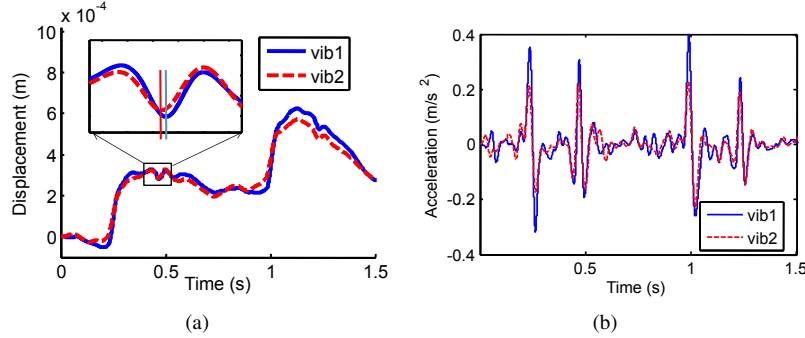


Figure 6.5: (a) The displacements of the two pulses. (b) The accelerations of the two pulses.

and figure 6.5(b). It is found that, the noise of the acceleration signal is stronger than that of the velocity signal mainly in the high frequency region. If a proper filter is applied, the cross-correlation method can also work well with the acceleration signal, but not with the displacement signal, which has a strong low-frequency variation. Another byproduct of the LDV system is the heart rate of the subject. In this measurement, the average heart rate of the subject is around 78 bpm, which is calculated according to the time delay between two adjacent pulses.

6.5 Scanning-beam configuration

During the measurement, we found that it is not easy to point the laser beam from the LDV to the right position on the neck. This optical alignment procedure requires professional knowledge of the cardiovascular system and sometimes takes a long time. This inconvenience in the optical alignment procedure hampers the popularization of this device. To solve this problem, an on-chip scanning-beam design is proposed.

In the proposed scanning-beam design, the alignment procedure is automatically done by scanning the light beam among a number of positions on the skin to find the location with the strongest vibration amplitude. The interval between every two adjacent spots is around 5 mm, being a little bit smaller than the average carotid diameter (6.10 mm for women and 6.52 mm for men [19]) to ensure a sufficient space resolution of the scan. The number of positions is chosen to be 6 for each measurement beam as a result of balancing between scan range and design complexity. The scan is realized with 6 light transmitting antennas (TAs) for each measurement beam, and each TA corresponds to one light focus position on the skin. During the scan, the measurement light is routed to each of the 6 grating couplers in spatial sequence. The routing function can be realized on chip by means

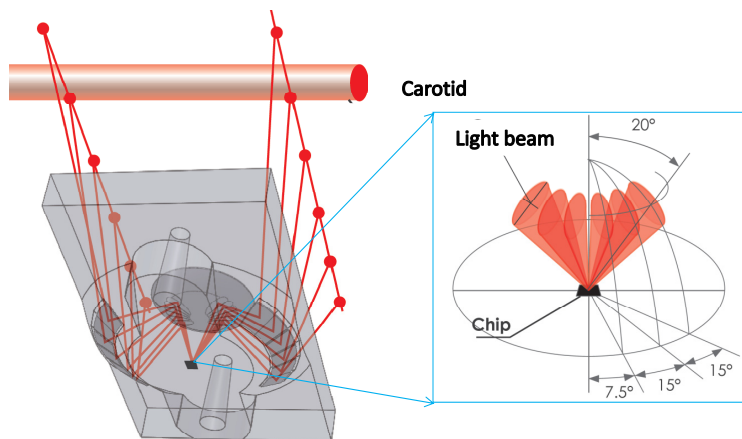


Figure 6.6: Designs for different light paths using on-chip grating couplers and free space optical systems (mockup). Reproduced from [21].

of optical micro-ring switches [20], which is controlled by a micro-controller next to the photonic chip.

The schematic of the output light beams from the 6 TAs and an optical system used to focus those light beams on the measurement positions are shown in figure 6.6. The TAs are designed in such a way that the projection of each output beam on the chip surface occupies an angle range of 15° . As a result, the 6 GCs take only one quadrant in the chip surface. In order to avoid an overlap between two adjacent light beams, the azimuthal beam divergence (the divergence of the beam projection on the chip surface) should be around 10° , which is plausible with current GC techniques. The zenith angles of the light beams (the angles between the light beams and the surface normal) can be chosen depending on the configuration of external optics, and these values are set to be 20° in figure 6.6. Two such TA groups are designed in two opposite quadrants, so that each one is responsible for one measurement position on the skin.

The two groups of light beams are separated using two groups of external mirrors, which are designed to focus the light beams onto 12 spots in two separate lines (see figure 6.6). To ensure that all light beams can be focused on the skin during the measurement, two spacers are used to keep the distance between the chip and the skin at a predefined value (see figure 6.7). It has been tested that the influence of the spacers on the vibrations of the measurement positions is not significant. However, whether the use of spacers changes the measured PWV value is still unclear and needs further study.

Compared to the light-beam scanning techniques using scan engines, the on-chip scanning approach is advantageous since it does not introduce any moving

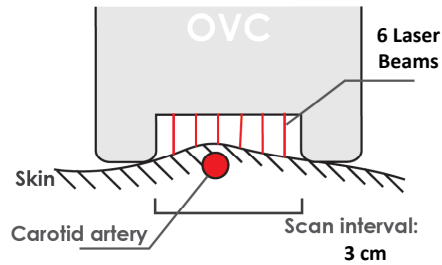


Figure 6.7: The spacers of OVC, which are used to keep a distance between the optical components and the skin. Reproduced from [21].



Figure 6.8: The view of the PWV measurement device. Reproduced from [21].

part in the device, which may lead to a device vibration that will be added to the LDV output signals.

6.6 Concept product design

The concept product design of a hand-held PWV measurement device has been made by Dries Willems as a master project for a degree in produce design at Arte-sis hogeschool Antwerpen [21], and his design is shown in figure 6.8. The device is 10 cm long along the longest side, 4.5 cm wide, and 2 cm thick. There are four buttons in the device: the switch button is used to turn the state of the device between “on” and “off”, the two small 8 mm blue buttons are used for navigating among different functions, and the 12 mm black button is used to confirm a function.

The on-chip scanning beam method is used in this hand-held device to ensure that general practitioners can easily make the PWV measurement. The measured values of PWV and heart rate can be displayed on the device immediately after

one successful measurement. More details about this concept design can be found in [21].

6.7 Conclusions

In this chapter, the proof-of-concept of a miniaturized PWV measurement device utilizing two-point LDV photonic integrated circuit is demonstrated with experimental results. The cross-correlation method is used to derive the PWV, and the time delay error was found to be around 0.1 ms. In addition, the device is able to measure the full range of CCA PWV when the separation between the two measurement spots is only 1.5 cm apart from each other. A scanning beam design used to alleviate the alignment requirement of the measurement is also proposed in this chapter. A concept product design based on this scanning beam approach is proposed and described.

In future work, efforts should be made to integrate lasers and photo-detectors on the same photonic integrated circuits. A PIC with more than two LDVs is also interesting for future study since it can be used to obtain more information of the pulses at different locations.

References

- [1] R. J. Adrian. *Multi-point optical measurements of simultaneous vectors in unsteady flow: a review*. International Journal of Heat and Fluid Flow, 7(2):127–145, 1986.
- [2] K. Venkatakrishnan, B. Tan, and B.K.A. Ngoi. *Two-axis-scanning laser Doppler vibrometer for precision engineering*. Optics and Lasers in Engineering, 38(3-4):153–171, 2002.
- [3] E. Li, J. Xi, J. Chicharo, J. Yao, and D. Yu. *Multi-point laser Doppler velocimeter*. Optics Communications, 245(1-6):309–313, January 2005.
- [4] Y. Fu, M. Guo, and P. B. Phua. *Spatially encoded multibeam laser Doppler vibrometry using a single photodetector*. Optics Letters, 35(9):1356–8, May 2010.
- [5] A. Dogui, N. Kachenoura, F. Frouin, M. Lefort, A. De Cesare, E. Mousseaux, and A. Herment. *Consistency of aortic distensibility and pulse wave velocity estimates with respect to the Bramwell-Hill theoretical model: a cardiovascular magnetic resonance study*. Journal of cardiovascular magnetic resonance : official journal of the Society for Cardiovascular Magnetic Resonance, 13(1):11, January 2011.
- [6] A. Campo, P. Segers, and J. Dirckx. *Laser Doppler vibrometry for in vivo assessment of arterial stiffness*. In IEEE International Workshop on Medical Measurements and Applications Proceedings (MeMeA), pages 119 – 121, Bari, 2011.
- [7] M. W. Rajzer, W. Wojciechowska, M. Klocek, I. Palka, M. Brzozowska-Kiszka, and K. Kawecka-Jaszcz. *Comparison of aortic pulse wave velocity measured by three techniques: Complior, SphygmoCor and Arteriograph*. Journal of Hypertension, 26(10):2001–7, October 2008.
- [8] J. Blacher, R. Asmar, S. Djane, G. M. London, and M. E. Safar. *Aortic Pulse Wave Velocity as a Marker of Cardiovascular Risk in Hypertensive Patients*. Hypertension, 33(5):1111–1117, May 1999.
- [9] Pierre Boutouyrie and Sebastian J Vermeersch. *Determinants of pulse wave velocity in healthy people and in the presence of cardiovascular risk factors: 'establishing normal and reference values'*. European heart journal, 31(19):2338–50, October 2010.
- [10] G. Mansia, G. De Backer, A. Dominiczak, R. Cifkova, R. Fagard, G. Germano, G. Grassi, A. M. Heagerty, S. E. Kjeldsen, S. Laurent, K. Narkiewicz,

- L. Ruilope, A. Rynkiewicz, R. E. Schmieder, H. A. j. Struijker Boudier, and A. Zanchetti. *2007 ESH-ESC Guidelines for the management of arterial hypertension: the task force for the management of arterial hypertension of the European Society of Hypertension (ESH) and of the European Society of Cardiology (ESC)*. *Blood Pressure*, 16(3):135–232, January 2007.
- [11] Wikipedia Contributors. *Artery*.
- [12] E. Hermeling, K. D. Reesink, R. S. Reneman, and A. P. G. Hoeks. *Confluence of incident and reflected waves interferes with systolic foot detection of the carotid artery distension waveform*. *Journal of Hypertension*, 26(12):2374–80, December 2008.
- [13] J. Luo, R. X. Li, and E. E. Konofagou. *Pulse wave imaging of the human carotid artery: an in vivo feasibility study*. *IEEE transactions on ultrasonics, ferroelectrics, and frequency control*, 59(1):174–81, January 2012.
- [14] A. Campo and J. Dirckx. *Dual-beam laser Doppler vibrometer for measurement of pulse wave velocity in elastic vessels*. In Ramón Rodríguez-Vera and Rufino Díaz-Urbe, editors, *22nd Congress of the International Commission for Optics: Light for the Development of the World*, volume 8011, pages 80118Y–1, August 2011.
- [15] S. Stankovic, R. Jones, M. N. Sysak, J. M. Heck, G. Roelkens, and D. Van Thourhout. *Hybrid III-V/Si Distributed-Feedback Laser Based on Adhesive Bonding*. *IEEE Photonics Technology Letters*, 24:2155–2158, 2012.
- [16] L. Vivien, J. Osmond, J.-M. Fédéli, D. Marris-Morini, P. Crozat, J.-F. Damlencourt, E. Cassan, Y. Lecunff, and S. Laval. *42 GHz p.i.n Germanium photodetector integrated in a silicon-on-insulator waveguide*. *Optics Express*, 17(8):6252–7, April 2009.
- [17] Y. Li, S. Verstuyft, G. Yurtsever, S. Keyvaninia, G. Roelkens, D. Van Thourhout, and R. Baets. *Heterodyne laser Doppler vibrometers integrated on silicon-on-insulator based on heterodyne thermo-optic frequency shifters*. *Applied Optics*, 52(10):2145–52, April 2013.
- [18] <http://www.epxfab.eu>.
- [19] J. Krejza, M. Arkuszewski, S. E. Kasner, J. Weigele, A. Ustymowicz, R. W. Hurst, B. Cucchiara, and S. R. Messe. *Carotid artery diameter in men and women and the relation to body and neck size*. *Stroke; a journal of cerebral circulation*, 37(4):1103–5, April 2006.

-
- [20] S. J. Emelett and R. Soref. *Design and simulation of silicon microring optical routing switches*. *Journal of Lightwave Technology*, 23(4):1800–1807, April 2005.
- [21] D. Willems. *Concept design of a compact diagnosis tool for cardiovascular diseases using LDV*, 2011.

7

Conclusion

7.1 Conclusions

In this thesis, we have discussed the feasibility of realizing a miniaturized laser Doppler vibrometer (LDV) on a silicon-on-insulator (SOI) platform. Several problems brought to the miniaturized LDV by this SOI platform were analyzed, and corresponding solutions were proposed and realized. Several on-chip LDVs with expected performance are finally demonstrated.

The SOI platform nowadays can provide all necessary components, especially the optical frequency shifter (OFS) and a 90° optical hybrid, for implementing an LDV system. On the SOI platform, LDVs with very small footprint can be realized. The minimal size of our proposed on-chip LDV devices is less than 0.4 mm^2 . With a better design, this value can be even smaller. Production cost of these on-chip LDVs can be strongly reduced in case of a high-volume production.

Except the strengths brought by the SOI platform, some problems have to be considered as well. According to theoretical analysis, several important deviation sources can strongly influence the performance of an on-chip LDV. They are the spurious reflection in on-chip devices, imperfect 90° optical hybrids (for homodyne), and imperfect optical frequency shifter (for heterodyne). According to simulation, to ensure that the phase deformation in the LDV output is lower than 0.01π , the following requirements should be fulfilled:

1. The power of the spurious reflection is 30 dB lower than that of the measurement signal.

2. The power of the -1st order harmonic in the frequency shifted reference signal is 30 dB lower than that of the fundamental harmonic of the reference signal.
3. The power of the 0th order harmonics in the frequency shifted reference signal is 30 dB lower than that of the measurement signal.

Demodulation methods corresponding to these deviations have been proposed and analyzed in simulation, which has shown that the demodulation is quite successful. However, these demodulation methods may desire a significant calculation time and thus may not work well for high frequency vibration measurements. Noise also strongly limits the performance of these demodulation methods.

To avoid the unnecessary compensation procedure, several on-chip designs have been redesigned to suppress the reflection. These devices include the grating couplers and 2×1 multi-mode interference (MMI) couplers. According to analysis, the strong spurious reflections existing in these devices are mainly caused by the mode-mismatching boundaries. In our reflectionless designs, the reflecting boundaries are deliberately tilted so that the reflections are sent to somewhere else rather than the input waveguide. Therefore the backreflection is reduced. It turned out that with these improved designs, the reflection of grating couplers are reduced to -40 dB (compared to the power of the input light). For the 2×1 MMI, the reflection is reduced to around -35 dB.

The optical frequency shifter (OFS) can also be realized on the SOI platform. On one hand, the serrodyne method can be used for generating a low frequency shift using a thermo-optic (TO) phase modulator, which has shown a second order suppression of 39 dB. On the other hand, a four-branch interferometry frequency shift method can strongly suppress the -1st order and 0th order harmonics regardless of the spurious reflections. Thus the four-branch interferometry method can be used for generating a high frequency shift with the help of carrier-depletion type modulators.

Based on the TO-based low-frequency serrodyne OFS, an on-chip heterodyne LDV is realized and measured. Measurement results show that the displacement sensitivity of this device is around 1 nm. Homodyne LDVs are also implemented with the help of an integrated 90° optical hybrid, and it demonstrates a minimal displacement sensitivity of 6 nm. In these designs, however, laser sources and photo-detectors are not integrated on the chip to avoid additional influences to the on-chip interferometers.

A device consisting of two stand-alone homodyne LDVs is also reported. This device can be used for measuring the arterial pulse wave velocity (PWV), which is an important marker for cardiovascular risks. The measurement is realized by calculating the transit time of the pulse between two spots on a common-carotid artery. Measurements shown that the output time accuracy of this double LDV

system is around 0.1 ms, which is good enough for the PWV measurement.

According to the above mentioned discussions, the SOI platform shows a promising capability of integrating miniaturized LDV devices. However, there is still a lot of space to improve the on-chip LDV designs, which will be discussed in the following section.

7.2 Prospectives

Up to now we have demonstrated several working LDV devices on the SOI platform. However, there are still several problems with these devices to be solved. One problem is the realization of fast serrodyne optical frequency shifters. As is already discussed, the four-branch interferometry frequency shifter may be used for realizing this function. However, it has not been fabricated and thus needs to be implemented and demonstrated by measurement in the future.

Another important issue is the integration of laser sources and photo detectors. Though these integrations have been realized and reported, they may greatly increase the fabrication complexity and influence the performance of the interferometer. Thus we have not tested the designs with integrated laser sources and photo detectors. But they should be implemented on chip in the future to eventually realize a fully integrated on-chip LDV system. The photo-detectors can be germanium-based and they can be directly provided by ePIXfab. Integrated lasers, however, may need to be realized in our own cleanroom with bonding technique. At the same time, integrated optical isolators are also needed to prevent the influence of back-reflections on the laser.

The capability of realizing multi-point LDVs is an important advantage of miniaturized LDVs. A Dual-LDV device has been reported in this thesis with successfully demonstrated PWV measurements. From the PWV measurement, we found that with three or more light beams we can obtain more information of the pulse waves. Therefore it would be very interesting to realize multi-point LDV devices using the SOI platform. There may be other applications that can benefit from the realization of multi-beam LDVs.



Optical frequency domain reflectometry

The optical frequency domain reflectometry (OFDR) is a technique for measuring reflections. Like optical time domain reflectometry (OTDR), this technique can resolve the positions of different reflection sources. OTDR is usually used for measuring reflections within a long distance, while OFDR is used for resolving small reflecting structures. In this section, the OFDR method used for on-chip reflection measurements is described.

In our OFDR measurement setup, the simplified OFDR method proposed by Morichetti [1] is used, which is shown in figure A.1. In this setup, the light source can be a broad band source or a tunable laser. Two important parameters should be defined before choosing the type of the source: the distance range L_{ofdr} and the distance resolution ΔL_{ofdr} . The L_{ofdr} of the OFDR is determined by the frequency resolution df of the optical spectrum analyzer (when a broad band source is used) or of the tunable laser, with the following relation

$$L_{ofdr} = \frac{c}{4n_g df} \approx \frac{\lambda_0}{4n_g d\lambda} \quad (\text{A.1})$$

where n_g is the group index of the light in the medium, and $d\lambda$ is the wavelength resolution. The distance resolution ΔL_{ofdr} is determined by the full-width half-maximum of the source spectrum $\Delta f_{1/2}$, with the following relation

$$\Delta L_{ofdr} = \frac{c}{2n_g \Delta f_{1/2}}. \quad (\text{A.2})$$

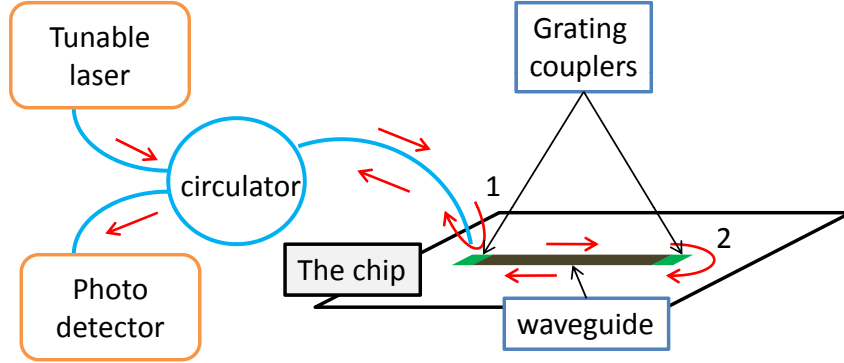


Figure A.1: The optical frequency domain reflectometry (OFDR) setup used for measuring reflections from a chip.

When input light is coupled into the on-chip device using a grating coupler, the value of $\Delta f_{1/2}$ is limited by the transmission spectrum of the grating coupler. We use a tunable laser in our measurement since the resolution of our optical spectrum analyzer is not sufficient.

In order to measure the reflection of an on-chip grating coupler we use the following procedure. First we align the input fiber with the help of an output fiber. After alignment, the output fiber is moved away so that the influence caused by the reflection of the output fiber facet is removed. With the help of a circulator, the reflected light signal including reflections from the input fiber facet and from the target reflective component in the waveguide is retrieved. In practice, a wavelength range from 1490 nm to 1570 nm with a 20 pm resolution was usually used.

The postprocessing on the reflection spectrum is realized in a computer, and a spatial distribution of the reflection is calculated from the autocorrelation $R(z)$ of the reflection spectrum. Three steps are done before calculating $R(z)$:

- interpolating the reflection spectra from the wavelength domain to the frequency domain.
- multiplying a Gaussian window to the spectrum in the frequency domain, so as to suppress numerical leakages [2]
- zero padding, in order to get a denser frequency mesh in the autocorrelation function, which is good for estimating the 3 dB bandwidth of peaks.

After these steps, a power spectral density $P(f)$ for an array of frequencies f is obtained. $R(z)$ is then derived by calculating the inverse Fourier transform of $P(f)$. Peaks in the power spectral density $P(f)$ show the position and power of different reflections.

References

- [1] F. Morichetti, A. Canciamilla, C. Ferrari, M. Torregiani, A. Melloni, and M. Martinelli. *Roughness Induced Backscattering in Optical Silicon Waveguides*. Physical Review Letters, 104(3):1–4, January 2010.
- [2] F. J. Harris. *On the use of windows for harmonic analysis with the discrete Fourier transform*. Proceedings of the IEEE, 66:51–83, 1978.

B

Tilted grating coupler design

B.1 Introduction

In this section, two derivations for the tilted grating coupler design are explained. The first one is about the angle deviation in a tilted grating coupler if the effective refractive index of the guided mode in the grating region is wrongly estimated. The second one is about the formula for tilted focusing grating coupler design.

B.2 Deviation of the direction in the out coupled light

When a tilted 1D grating coupler is designed, an approximation of the effective index of the guided mode in the grating region n_g^0 has to be made. However, sometimes this effective index estimation is not correct, and an approximated value n_g is used in the formula instead of n_g^0 . This the effective index deviation $\Delta n_g = n_g - n_g^0$ can change the direction of the out-coupled light.

To obtain this deviation, one can refer to figure B.1. A wrong estimation of the effective index of n_g^0 leads to a wrong \vec{k}_g value. In figure B.1 the dashed vectors are used for the design. However, the real \vec{k}_g value is smaller than the estimated one, and the difference is Δk_g . Considering this deviation, we can use the relation represented by the solid vectors to obtain the real value of $\vec{k}_{c,p}$, which is the projection of the output light wave vector \vec{k}_c on the chip surface.

Since the length of \vec{k}_c tends to keep the same value, the new direction of this

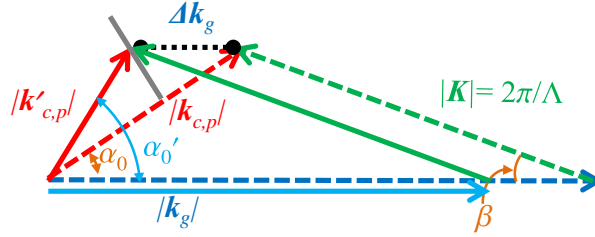


Figure B.1: The vector relation of a 1D tilted grating coupler with an effective index error Δn .

vector can be calculated as

$$\alpha'_0 = \alpha_0 + \arctan \left(\frac{\Delta n_g \sin \alpha_0}{n_{c,p} - \Delta n_g \cos \alpha_0} \right), \quad (\text{B.1})$$

$$\phi'_0 = \arcsin \left(\frac{\sqrt{n_{c,p}^2 + \Delta n_g^2 - 2n_{c,p} \Delta n_g \cos \alpha_0}}{n_c} \right). \quad (\text{B.2})$$

These expressions agree well with the measurement results, which has been discussed in Chapter 3.

B.3 Tilted focusing grating coupler

The focusing grating coupler design is simplified to a grating structure that couples light originating from a single spot on a chip to free space in a certain direction, described by the azimuth α_0 and zenith angle ϕ_0 . The azimuth α_0 is the angle between the projection of the output direction and the direction of incoming light, while the zenith angle ϕ_0 is the direction between the output light and the normal of the chip surface. In this section, an assumption is made that the effective index of guided light in the slab region n_s is the same as that in the grating region n_g^0 .

The output light can be considered as a plane wave, and the plane wave front is perpendicular to the output direction. So the design should fulfill this phase relation for each possible light path. To clarify this wavefront relation, a schematic plot of the grating coupler is shown in figure B.2.

Firstly only the first trenched line is considered. The phase condition of the out-scattered light is shown in figure B.2. For each azimuth direction from the light source, the light path includes two parts. The part in the slab region has a phase change of $n_g^2 k_0 r(\alpha)$, while the phase shift in free space is $n_c k_0 D(\alpha) \sin \phi$. Considering that $D(\alpha) = r(0) - r(\alpha) \cos \alpha$, we have

$$n_g^0 k_0 r(0) = n_g^0 k_0 r(\alpha) + n_c k_0 [r(0) - r(\alpha) \cos \alpha] \sin \phi. \quad (\text{B.3})$$

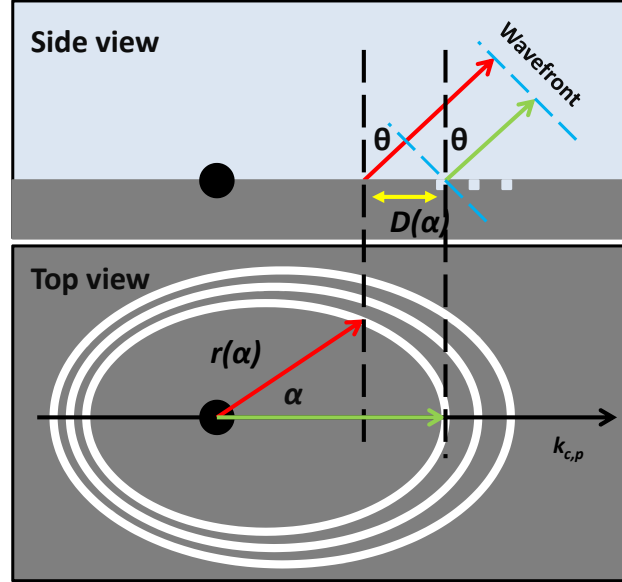


Figure B.2: Schematic of tilted FGCs.

This leads to

$$r(\alpha) = r(0) \frac{n_g^0 - n_c \sin \phi}{n_g^0 - n_c \cos \alpha \sin \phi}. \quad (\text{B.4})$$

For different lines, $r(0)$ is denoted as $r(0, q)$, where q is the index of the each grating. Since $r(0, q)$ follows the form of a standard 1D grating coupler, and thus we have

$$r(0, q) = \frac{q\lambda_0}{n_g^0 - n_c \sin \phi}, \quad (\text{B.5})$$

where $q = q_0, q_0 + 1, \dots$ is the index of each trench. By replacing the $r(0)$ value in Eq. B.4 with the $r(0, q)$ in Eq. B.5, we have

$$r(\alpha) = \frac{q\lambda_0}{n_g^0 - n_c \cos \alpha \sin \phi}. \quad (\text{B.6})$$

These curves turn out to be an array of elliptical curves.

B.4 Tilted focusing grating coupler with amendment

When considering that $n_g^0 \neq n_s$, the formula has to be amended. To simplify the problem, we assume that there is no refraction on the boundary between these two

regions. This is a good approximation when the incident angle of the light at the interface is not very large.

Under this approximation, Eq. B.4 for the first line has to be written as

$$r(\alpha, 0) = r(0, q_0) \frac{n_s - n_c \sin \phi}{n_s - n_c \cos \alpha \sin \phi}. \quad (\text{B.7})$$

For the other lines, the effective index of light in the grating region has to be considered. So that the Eq. B.3 has to be changed to

$$R(0, q)k_0 = R(\alpha, q)k_0 + n_c[r(0, q) - r(\alpha, q) \cos \alpha] \sin \phi k_0. \quad (\text{B.8})$$

where

$$R(\alpha, q) = n_s r(\alpha, q_0) + n_g^0 [r(\alpha, q) - r(\alpha, q_0)] \quad (\text{B.9})$$

is the on-chip optical length of the light in both the slab and the grating regions.

Removing the k_0 in Eq. B.8, the left side of Eq. B.8 is

$$n_s r(0, q_0) + n_g^0 [r(0, q) - r(0, q_0)], \quad (\text{B.10})$$

and the right side is

$$(n_s - n_g^0)r(\alpha, q_0) + n_c \sin \phi r(0, q) + (n_g^0 - n_c \sin \phi \cos \alpha)r(\alpha, q).$$

This will lead to

$$r(\alpha, q) = \frac{(n_s - n_g^0)[r(0, q_0) - r(\alpha, q_0)] + (n_g^0 - n_c \sin \phi)r(0, q)}{n_g^0 - n_c \sin \phi \cos \alpha}. \quad (\text{B.11})$$

Considering Eq. B.7 and Eq. B.5, the numerator of Eq. B.11 thus becomes

$$\begin{aligned} & (n_s - n_g^0)[r(0, q_0) - r(\alpha, q_0)] + (n_g^0 - n_c \sin \phi)r(0, q) \\ = & (n_s - n_g^0)[r(0, q_0) - r(0, q_0) \frac{n_s - n_c \sin \phi}{n_s - n_c \cos \alpha \sin \phi}] + (n_g^0 - n_c \sin \phi) \frac{q\lambda_0}{n_g^0 - n_c \sin \phi} \\ = & \frac{q_0\lambda_0}{n_g^0 - n_c \sin \phi} \left[\frac{\zeta}{n_s - n_c \cos \alpha \sin \phi} \right] + (q - q_0)\lambda_0, \end{aligned}$$

where

$$\begin{aligned} \zeta &= (n_s - n_g^0)n_c \sin \phi - (n_s - n_g^0)n_c \cos \alpha \sin \phi \\ &+ (n_g^0 - n_c \sin \phi)(n_s - n_c \cos \alpha \sin \phi) \\ &= (n_g^0 - n_c \cos \alpha \sin \phi)(n_s - n_c \sin \phi) \end{aligned}$$

Finally the numerator becomes

$$\frac{q_0\lambda_0}{n_g^0 - n_c \sin \phi} \left[\frac{(n_g^0 - n_c \cos \alpha \sin \phi)(n_s - n_c \sin \phi)}{n_s - n_c \cos \alpha \sin \phi} \right] + (q - q_0)\lambda_0. \quad (\text{B.12})$$

Put Eq. B.12 in Eq. B.11, the radius of each line will thus be obtained

$$\begin{aligned}
 r(\alpha) &= \frac{(q - q_0)\lambda_0}{n_g^0 - n_c \cos \alpha \sin \phi} + \frac{n_s - n_c \sin \phi}{n_g^0 - n_c \sin \phi} \frac{q_0 \lambda_0}{n_s - n_c \cos \alpha \sin \phi} \\
 &= \frac{(q - q_0)\lambda_0}{n_g^0 - n_c \cos \alpha \sin \phi} + \frac{kq_0 \lambda_0}{n_s - n_c \cos \alpha \sin \phi} \quad (\text{B.13})
 \end{aligned}$$

where

$$k = \frac{n_s - n_c \sin \phi}{n_g^0 - n_c \sin \phi}. \quad (\text{B.14})$$

